UNIVERSITAT DE BARCELONA

Inkjet printing next-generation flexible devices: memristors, photodetectors and perovskite LEDs

Sergio González Torres

Doctoral thesis

Inkjet printing next-generation flexible devices: memristors, photodetectors and perovskite LEDs

Author: Sergio González Torres

Directors: Prof. Blas Garrido Fernández

Dr. Giovanni Vescio

Tutor: Prof. Blas Garrido Fernández

Barcelona, January 2024

UNIVERSITAT DE BARCELONA

Inkjet printing next-generation flexible devices: memristors, photodetectors and perovskite LEDs

Programa de doctorat en Nanociències

Autor: Sergio González Torres

Directors: Prof. Blas Garrido Fernández

Dr. Giovanni Vescio

Tutor: Prof. Blas Garrido Fernández

Departament d'Enginyeria Electrònica i Biomèdica

Barcelona, Gener de 2024

UNIVERSITAT DE BARCELONA

Abstract

New pressures due to emerging trends in device fabrication are driving research efforts into new materials and manufacture processes to achieve new combinations of properties, including physical and chemical sensing capabilities, conductivity, flexibility, and transparency. Such applications are typically encompassed in the field of internet of things (IoT), based on the use of relatively simple, connected devices that sense and interact with the environment. To tackle these challenges, printed electronics, a field of graphics and text printing technologies adapted to the manufacture of electronics, is a favorable candidate to satisfy new needs in device fabrication, enabling the deposition of next-generation materials in ink form, at low-cost, with the potential for scalable manufacture.

Inkjet printing, a member of the field of printed electronics, is a solution-based deposition technology that allows the deposition of a multitude of functional materials, including insulators, semiconductors, and conductors. Thanks to its digital patterning property, device geometries can be defined without the need for a mask of photolithographic processes. This attribute not only reduces manufacturing costs, but also enables quick prototyping of device architectures at a small scale, providing a way to optimize device iterations at reduced upfront cost with adaptability for later large-scale manufacture. Thanks to its versatility in material choice and mask-less manufacture, whole device structures may be fabricated through inkjet-printing. Nonetheless, inkjet printing may also serve as a complement to more established technologies, such as complementary metal-oxide-semiconductor (CMOS) processes, where it can fulfill a role of depositing innovative materials.

This thesis attempts to showcase the versatility of inkjet printing as a device fabrication technology to address future challenges. After study and validation of inkjet-printed nanostructured materials from various families, three different types of devices are fabricated and characterized. The demonstrated devices cover non-overlapping application fields, highlighting the adaptability of inkjet-printing: 2D h-BN memristors, metal oxide nanoparticle photodetectors, and light-emitting diodes (LEDs).

The first experiments in this thesis deal with inkjet-printed 2D h-BN nanoflake memristors for hardware security applications. Memristors are a family of devices, sometimes known as the fourth passive circuit element along the resistor, the inductor and the capacitor, whose electrical resistance can be tuned by electrical manipulation, a property that can be exploited to represent information. Although promising results have demonstrated the potential for high density integration for data storage applications, with companies like HP dedicating research efforts in this field, the applicability of these devices is still subject to the limited device-to-device and cycle-to-cycle repeatability of memristors. In this thesis, the inherent stochasticity of memristors is exploited for use as true random number generators (TRNG). Particularly, their application as physical unclonable functions is showcased, which can be used as unique identifying digital keys.

Following, inkjet-printed metal oxide nanoparticle photodetectors are demonstrated. Metal oxides are a family of materials that are being studied as charge transport and blocking materials for solar cells and LEDs, and in this thesis are proposed for use in LED architectures as solution-processable inorganic materials. Moreover, as wide-bandgap materials, metal oxides can fulfill a promising role in visible-transparent, mechanically flexible, low-cost selective ultraviolet photodetectors. In this context, inkjet-printed metal oxide nanoparticle p-n junction photodiodes are fabricated and characterized.

In the final sections, the rapidly developing field of perovskite LEDs (PeLEDs) is studied, focusing on the inkjet printing of inorganic $CsPbBr_3$ perovskite quantum dot LEDs for display applications. Perovskites have in recent years shown impressive progress in light emitting and photovoltaic efficiency and are positioned to become the active material in future LEDs and solar cells. The highest efficiencies in perovskite LEDs in the literature are generally achieved through nanostructuring into quantum dots, which can be synthesized in colloidal dispersion through facile, scalable wet chemical processes such as hot injection and deposited through solution deposition processing. While efforts in the PeLED literature have focused on obtaining record efficiencies through the use of laboratory-scale techniques such as spin coating, few researchers have demonstrated scalable fabrication technologies for solution-processed perovskite LEDs such as inkjet printing. Here, the viability of inkjet printing is validated by showcasing fully-printed PeLEDs on flexible and rigid substrates, achieving a pure green emission with a narrow

full-width half maximum down to 22 nm centered at 517 nm, corresponding approximately to 0.119, 0.790 color coordinates in CIE 1931 color space, consistent with literature results of perovskite layers obtained through more established techniques, proving that the perovskite properties are maintained by the inkjet deposition process. Both fully inkjet-printed and mixed PeLED architectures (with inkjet-printed perovskite and spin-coated/evaporated transport layers), obtaining luminances up to 17920 cd/m^2 for mixed ones, competitive with literature structures obtained through more established deposition methods, and up to 324 cd/m^2 for fully inkjet-printed ones, within luminance specifications of display technologies and analogous to many commercial displays. Moreover, this result is achieved through low-temperature post-processing inorganic metal oxide transport layers, which substitute organic materials known for their limited long-term stability. Finally, a fully inkjet-printed PeLED active and transport/blocking layer stack is demonstrated on flexible substrates.

Acknowledgments

This doctoral thesis could not have happened without the support of many people.

First, I must thank my advisors Dr. Blas Garrido Fernández and Dr. Giovanni Vescio, for their guidance and complete availability throughout these 5 years. In addition, despite not listing as my directors, I extend my sincere gratitude to Dr. Gayathri Mathiazhagan for her expertise and company during countless hours at the lab, Dr. Sergi Hernández for his knowledge and advice in various measurement setups and proposed ideas for experiments and Dr. Albert Cirera, for his frequent heads-up on literature updates and experimental feedback.

I would also like to express my gratitude to our partners at INAM-UJI (Dr. Iván Mora-Sero's group), Universitat de València (Dr. Juan P. Martínez's group), Avantama AG, Saule Research Institute, ETHZ (Kovalenko lab), and Dr. Mario Lanza's group (particularly Dr. Kaichen Zhu) for their expertise, samples, measurements, and to Jesús Sanchez-Diaz and Rafael Abargués and colleagues for their warm welcome in my short visits at INAM-UJI and UV. Moreover, I am grateful to my senior colleagues that have been in Dr. Blas group, who have always been eager to lend a hand and whose example I have tried to follow: Dr. Juan Luis Frieiro, Dr. Oriol, and Dr. Julià López-Vidrier.

Thanks to all members of the Despatx Patera, particularly those I have had the chance to share office with, making my time at the faculty much more enjoyable: Daniel del Pozo, Dra. Catalina Coll, Dr. Adrià Huguet-Ferran, Dr. Javier Blanco-Portals, Dr. Lluís López-Conesa, Joshua Diago, and to the newer students whom I haven't had the chance to spend as much time with, I wish you a profitable stay. I also can't forget everyone at the *Laboratori de Nanoelectrònica Aplicada* whom tedious work afternoons became more enjoyable with.

I would also like to thank anyone else in the department of electronics engineering at UB whom at one point or another I have had the pleasure to interact with: Dr. Daniel Navarro-Urrios, Dr. Paolo Pelegrino, Dra. Francesca Peiró, Dra. Sonia Estradé, Dra. Anna Vilà, Dr. Albert Romano, Dr. Cristian Fábrega, Roser Marzo, Sergio Rodríguez, Martín, Antonio Cruz, Andrés Romero, and the late Dr. Albert Cornet, as well as any other name that might have slipped my mind.

Finally, to my close family and friends, without whose unconditional support none of this would have been possible, thank you.

List of figures

List of tables

List of acronyms

AI	Artificial intelligence
a-Si:H	Amorphous hydrogenated silicon
CBL	Charge blocking layer
CBM	Conduction band minimum
CCD	Charge-coupled device
CCFL	Cold cathode fluorescent lamp
CMC	Carboxy methyl cellulose
CMOS	Complementary metal-oxide-semiconductor
CPU	Central processing unit
CTL	Chage transport layer
CVD	Chemical vapor deposition
CVS	Constant voltage stress
DMD	Digital micromirror device
ECM	Electrochemical metallization
EL	Electroluminescence
EQE	External quantum efficiency
ETL	Electron transport layer
FET	Field effect transistor
FWHM	Full-width half-maximum
HOMO	Hoghest occupied molecular orbital
HRS	High resistance state
HTL	Hole transport layer
IJP	Inkjet printing
IoT	Internet of things
ITO	Indium tin oxide
LCD	Liquid-crystal display
LED	Light emitting diode
LIFT	Laser-induced forward transfer
LPE	Liquid-phase exfolliation
LRS	Low resistance state
LUMO	Lowest unoccupied molecular orbital
MHP	Metal-halide perovskite
MIM	Metal-insulator-metal
NC	Nanocrystal
NP	Nanoparticle
NTSC	National television system commitee
OLED	Organic light-emitting diode
PEDOT:PSS	poly(3,4-ethylenedioxythiophene) polystyrene sulfonate
PeLED	Perovskite light emitting diode

PL	Photoluminescence
PMT	Photomultiplier tube
Poly-TPD	Poly[N,N' -bis(4-butylphenyl)-N,N' -bis(phenyl)-benzidine]
PO-T2T	2,4,6-tris[3-(diphenylphosphinyl)phenyl]-1,3,5-triazine
PUF	Physical unclonnable function
PVS	Pulsed voltage stress
QD	Quantum dot
QLED	Quantum dot light emitting diode
R2R	Roll-to-roll
ReRAM	Resistive random access memory
RGB	Red-green-blue
RS	Resistive switching
RSD	Resistive switching device
RTN	Random telegraph noise
RVS	Ramped voltage stress
SC	Spin coating
SEM	Scanning electron microscope
SMU	Source-measurement unit
TEM	Transmission electron microscopy
TFT	Thin film transistor
TRNG	True random number generation
UV	Ultraviolet
VBM	Valence band maximum
VCM	Valence charge mechanism
XRD	X-ray diffraction

Table of contents

Chapter 1
Introduction

Addressing contemporary and future challenges in optoelectronics requires the ever-constant development of new materials, devices, and fabrication strategies. Current challenges in different fields can be addressed thanks to the incorporation of nanostructured materials, which incorporate enhanced properties such as memristors,[1] photodetectors,[2] and high-color purity LEDs.[3] In addition, thanks to the low-temperature post-processing methods that solution processing allows compatibility with flexible substrates is enabled, allowing the fabrication of conformal and wearable devices. Some examples include enhanced healthcare monitoring by plasmonic biosensors,[4] touch sensitive human-computer interfaces for applications such as augmented reality,[5] flexible and green energy storage devices,[6] and wearable health sensors.[7] Such materials can be deposited through solution processing routes in a facile, low temperature, low-cost manner without relying on vacuum deposition or processes.

This thesis explores the use of inkjet printing, a solution-based deposition technology initially developed for the printing of arts and graphics, for the fabrication of electronic and optoelectronic devices. In contrast to most technologies in the field of printed electronics, inkjet printing allows the deposition of a wide range of materials while enabling quick prototyping thanks to its independence from masks to define printed patterns, combined with the potential for scalability of production.

Three device families will be explored: memristors for security applications, photodetectors, and light-emitting diodes (LEDs) for display applications, each one showcasing the potential for inkjet printing to tackle current technological challenges.

1.1. Inkjet printing for fast prototyping and high throughput

Traditional electronic and optoelectronic device fabrication routes often involve complex multi-step vacuum deposition processes that make scaling to large areas challenging and expensive[8] and require hazardous chemicals that later need to be disposed of.[9] For example, III-V compound-based LED and solar cell fabrication is generally achieved through metal-organic chemical vapor deposition,[10] often requiring the use of

hazardous gases such as phosphine (PH_3) and Arsine (AsH_3).[11]

Manufacturing companies have recognized since the turn of the millennium the potential of applying graphics printing technologies to the deposition of functional materials for optoelectronics.[12,13] This process involves the deposition of inks that contain the requisite materials onto a substrate (Fig. 1.1), falling within the domain known as solution processing. Among a variety of other printing methods such as gravure or offset, inkjet printing is a mature technology that was developed in the context of printing graphics and text. Unlike other technologies, however, inkjet printing allows the printing of an arbitrary pattern without the need to change masks or rolls, with good resolution and throughput. Compared to traditional vacuum deposition routes, solution processing allows facile, low-cost manufacturing for a variety of materials. Thus, inkjet printing provides a route for fast, low-cost prototyping with the potential for scaling. The applicability of inkjet printing for functional material deposition will be demonstrated through the fabrication of the following device families.
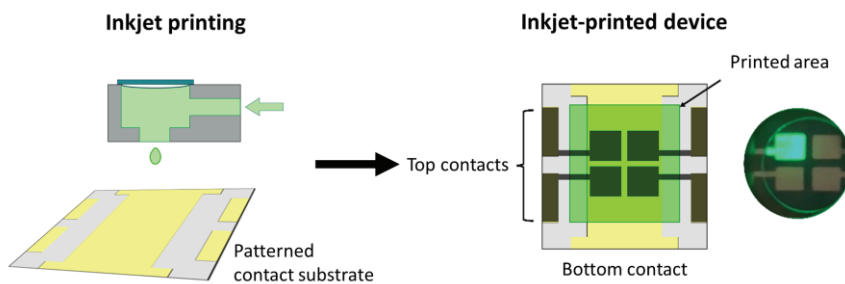
Fig. 1.1 Inkjet printing of electronic and optoelectronic devices.

1.2. Inkjet-printed h-BN memristors for security applications

Traditional central processing units (CPUs) rely on the integration of many transistors, which are the building blocks of logic gates. The miniaturization of transistors has been occurring exponentially year after year since the advent of integrated circuit (IC) processors, resulting in access to higher processing power at lower costs, commonly known as Moore's law.[14] Concerns have been raised about the long-term viability of this trend, however, as the scaling of transistors will eventually be limited by the size of atoms.[15] This limited future scaling of traditional CPUs, compounded with the explosion of big data and the rise of machine learning in many aspects of life, imposes a limit date

on the application of traditional CPUs. Computing tasks are moving towards a decentralized processing model: many smartphones come with an artificial intelligence accelerator,[16] and NVIDIA is speeding 3D processing workloads from their high-end graphics processing units (GPUs) with a machine learning accelerator that speeds up rendering in real-time by up-scaling from low resolution frames.[17,18]

The traditional processing architecture, known as the *Von Neumann model*, is optimized for linear instructions on a limited size of data, but is inefficient at calculations with massive data.[19] This is a result of the need to move information from memory to the CPU, an inefficient process that slows down computation and results in the so-called Von Neumann bottleneck.[20] In response, a new model of computing known as *in-memory computing* puts forward the idea to concentrate the storage and processing of information in the same hardware element.[21] To fulfill this role, researchers have proposed the memristor, a device also known as resistive random-access memory (ReRAM).[22,23] Memristors are a family of devices whose resistive state may be altered in a controlled way by application of electrical stresses.[24] Among other possible configurations, arrays of memristors may be used to perform vector-matrix multiplications efficiently. Although this concept of in-memory computing has been demonstrated in simulations and experimentally, the device-to-device and cycle-to-cycle stochasticity of memristors creates challenges for their application as memory elements[25] and to the in-memory computing model.[26,27]

Though currently the intrinsic variability of several studied families of memristors poses difficulties in computing applications, this unique physical property can be exploited for security and cryptography. Cryptography is a field that involves the application of algorithms to guard sensitive information, employing random numbers that can be used as keys to encrypt and decrypt data.[28] While random numbers can be generated through pseudo-random software algorithms, these are vulnerable to being exploited for their patterns, and are inferior to truly random hardware-based solutions. Physical unclonable functions (PUFs) are one such way to generate unique identifiers that are practically impossible to clone, cost effective, and resilient to attacks. PUFs draw their truly random key generation from micro- and nanoscopic variations intrinsic to their fabrication process. Safety measures are increasingly in need due to the rise of the internet

3

of things (IoT), where networks of simple devices collect and exchange information, with examples including smart watches, security cameras, home thermostats, etc. Security concerns have been raised, where unprotected sensitive IoT devices such as home cameras have been infiltrated easily by bad actors, gaining access to sensible information. Thus, in order to achieve the successful application of the IoT, improved security such as that provided by PUFs is needed.

Although CMOS PUFs have been demonstrated, it is hard to obtain true randomness from them.[29] Conversely, the inherent stochastic nature of memristors, usually regarded as their Achille's heel in other applications,[30] is an excellent source of true physical randomness.[28]

Most memristors studied in the literature have traditionally been manufactured from transition metal oxides like ZnO and HfO_2 in a metal-insulator-metal (MIM) structure, showing high operation speeds, long retention times, high endurance, and high integration density.[31] However, their development seems to have reached a plateau, as these record performances have been achieved separately on different device architectures, stunting their real-world commercial applicability.[32] This has prompted the movement of research towards new materials in search of new avenues for memristors, whence 2D layered materials have gained attention. Layered 2D materials have provided new qualities to other electronic device families such as field effect transistors (FETs), conferring flexibility, transparency, chemical stability, and a high ON/OFF ratio.[33] In addition, they allow the fabrication of flexible and transparent memristors.[34]

The deposition of 2D material-based devices can be facilitated thanks to the versatility of inkjet printing, which will be showcased here by fabricating and studying inkjet-printed h-BN memristors as candidates for building PUFs.

1.3. Inkjet-printed metal oxide photodetector diodes

The field of optoelectronics emerges from the interplay between electronics and light and contributes to a range of domains. In the field of communications, elements such as fiber optics and IR remote controls apply the principles of optoelectronics for the transmission of information. On the other hand, devices such as pulse oximeters and ambient light sensors use light to extract information from their environment. In order to

achieve these tasks, the photodetector is a fundamental element responsible for converting an optical signal into an electrical one. Owing to the breadth of applications in optoelectronics, the required characteristics of the corresponding photodetectors vary widely over the range of tasks. Such desirable characteristics might include high sensitivity, fast response, or discrimination of certain wavelength ranges.

Photodetection in the ultraviolet (UV) range is important for tasks such as flame detection, water purification, furnace control, UV astronomy, and UV radiation dosimetry.[35] A wide range of devices have been employed for UV photodetection, including semiconductor photodiodes, thermal detectors, photomultiplier tubes, and charge-coupled devices, thanks to their high gain and low noise floor.[36] However, these are not necessarily blind to visible light, and come with their own disadvantages. For example, photomultiplier tubes (PMT) devices are very sensitive, yet they are bulky and require high voltage power supplies, while charge-coupled devices (CCDs) are more compact but require long acquisition times for reliable signal capture. Semiconductor photodetectors stand out thanks to their low voltage requirements, compact form factor and low sensitivity to magnetic fields. In addition, they are low cost, have good linearity and sensitivity, and can operate at high speed.[37] Nonetheless, semiconductor UV photodetectors often employ narrow-bandgap materials, meaning that they also detect photon energies lower than the target UV, thus requiring optical filters for UV-only operation.

In order to address these problems, high-bandgap UV materials for photodetectors such as GaN have received interest and are becoming commercially available. In a parallel fashion, increasing interest has been developing in metal oxides, thanks to their natural abundance and low toxicity. One of the most well studied metal oxides is ZnO, which has optoelectronic properties similar to GaN. Remarkably, Zn is about 300 times cheaper per kilogram than Gallium, and its low toxicity is thoroughly tested to the extent that it is commonly included in sunscreens.[38]

Inkjet printing enables the facile fabrication of photodetectors from a wide array of metal oxides, demonstrated in this thesis by the inkjet-fabrication and characterization of n-ZnO, p-NiO photodetectors.

1.4. Inkjet-printed perovskite LEDs for display applications

Electric light sources are a fundamental aspect of modern life, not only for illumination, but also for information display, whether it be through simple LED indicators or high resolution, full color displays. The first major advancement in light generation came with the discovery and subsequent spread of incandescent, arc discharge, and other early forms of electrically generated light. These freed humanity from the dependence on combustion for light, providing higher brightness, and the safety and convenience of not relying on combustible matter.

Fast-forwarding to the present day, LEDs are taking over in most illumination applications, replacing other technologies such as incandescent, fluorescent, and halogen, which were in common use until recently. This transition, made possible by the relatively recent development of efficient blue emitters, is explained by the versatility of LEDs, which combine high efficiency, a compact form factor, long life, a narrow and tunable emission spectrum, and robustness. Applications of LEDs are as diverse as high-brightness compact flashlights, human-centric lighting, car headlights, and, remarkably, modern display applications.

The display manufacturing industry has come a long way since the days of cathode ray tube and early flat displays and has in recent years progressed greatly thanks to developments in LEDs. The first application of LEDs to display technologies was as backlights for liquid crystal display (LCD) panels, substituting earlier white fluorescent lighting, which have a wide color emission spectrum and require bulky driving electronics. Besides fulfilling the role of a backlight element, LEDs have also more recently been incorporated in displays in the form of emissive subpixel elements, as in the case of organic LEDs (OLEDs), which provide exceptional color accuracies and vibrant images. Being composed of an array of red-green-blue (RGB)-emitting subpixels that are switched on as required, OLED screens achieve a so-called "infinite"[39] contrast ratio, as blacks are represented by switching a portion of the screen off, which also results in reduced energy consumption. However, despite the vibrancy of OLED displays, they still suffer from high cost and limited lifetime due to their reliance on expensive and relatively unstable organic materials.

On a separate front, the advent of quantum dot (QD) synthesis enabled the fabrication of more stable emissive materials with higher emission purity.[40] QDs are semiconductor nanocrystals small enough to confer them new properties arising from quantum confinement, such as pure, size-tunable light emission. Inorganic QDs display pure emission with long-term robustness thanks to the inherent stability of inorganic materials, and the fact that the emissive properties are determined by the crystalline nanostructure of the QDs. For these reasons, QD-based displays currently represent the main competitor of OLED technology in the display front.

The main commercial application of QDs in display applications is commonly known as QLED, an iteration of LCD display technology where the backlight emission spectrum is enhanced with photoemissive quantum dots, which increases the purity of the RGB color components. However, while they currently are the most relevant commercially available competitor to OLED, QLED screens depend on expensive, highly toxic CdSe nanoparticles. In response, perovskite QDs are being studied as solution processable emissive materials for LEDs. Perovskites have been proposed as both color conversion layers and as active emissive layers in LED structures. Thanks to their precise emission wavelength tunability and narrow emission, perovskite QD downconversion-based display backlights have achieved upwards of 140% reproduction of the national television system commitee (NTSC) color gamut,[41] with facile synthesis methods at a reduced cost and reduced levels of toxicity compared to Cd-containing QDs.[42]

The capability of inkjet printing to fabricate perovskite QD-based LEDs is shown in this thesis through the inkjet-printed deposition of PeLEDs based on $CsPbBr_3$ QD colloidal suspension and metal oxide nanoparticle inks.

1.5. Objectives

This thesis seeks to demonstrate the application of inkjet printing as a material deposition technology that not only allows scalable, facile solution processing routes, but also enables the deposition of new materials for next generation devices. Particular focus has been placed on the *fully-inkjet* fabrication of devices, aiming to move away from the reliance on vapor deposition methods. The demonstration of fully-inkjet fabrication is a crucial step for the establishment of inkjet printing as a device manufacturing technology,

as it allows fabrication in a streamlined Roll-to-Roll (R2R) process, wherein device fabrication is performed continuously on a flexible substrate from an input roll to an output one, hence the name. This goal, however, can prove challenging due to the interactions between printing steps, as bottom layers can be negatively affected by the thermal and chemical stress caused by successive processes, constraining post-processing temperatures and requiring the use of orthogonal solvents.

Inkjet printing allows facile deposition of materials. In ***Chapter 4***, inkjet printing allows the deposition of h-BN with post-processing temperatures as low as 150 ºC, compared to chemical vapor deposition (CVD), which requires temperatures above 850 ºC.[43] In ***Chapter 5***, inkjet printing represents a simple, scalable deposition approach to deposit metal oxide thin films, compared to vacuum deposition. In ***Chapter 6***, inkjet printing enables the deposition of defect-resistant perovskite NC-based LEDs.

With the principal objective of showcasing the versatility of inkjet printing for the fabrication of electronic and optoelectronic devices, the following specific objectives will be undertaken in this thesis:

1. Verify the long-term switching stability of inkjet-printed h-BN memristors and study their modes of operation.

2. Demonstrate the applicability of inkjet-printed h-BN memristors as elements for PUFs and random number generation.

3. Develop high-quality thin films from inkjet-printable p-type and n-type metal oxide inks to be used as hole and electron transport layers for PeLEDs.

4. Fabricate photodetectors based on the metal oxide materials studied above, validating their optoelectronic properties.

5. Prepare ink formulations for inkjet printing technology to obtain high-quality thin films from inkjet-printable perovskite QD suspensions ($CsPbBr_3$).

6. Once high-quality inkjet-printed $CsPbBr_3$ layers are obtained, design a benchmark device structure for PeLEDs with inkjet-printed $CsPbBr_3$ based on proven structures from the relevant literature. Transport layers will be deposited by evaporation and spin coating, established technologies that will

be compared with inkjet printing.

7. Finally, demonstrate a fully inkjet-printed PeLED device structure on flexible substrates. This is a critical factor towards demonstrating the viability of inkjet printing as a device manufacturing technology for PeLEDs.

1.6. Outline of the thesis

In this thesis, inkjet printing has been demonstrated for the fabrication of electronic and optoelectronic devices of different types and families of materials. The thesis is divided as follows. ***Chapter 2****: Background and state of the art* provides an overview of printed electronics technologies, the materials used throughout this thesis and the three device families studied. Next, ***Chapter 3****: Fabrication and characterization methods* describes the different instrumental setups.

The following chapters summarize the main achievements for each device family. ***Chapter 4****: inkjet-printed h-BN memristors for hardware security*; ***Chapter 5****: Inkjet-Printed p-NiO/n-ZnO Heterojunction Diodes for Photodetection Applications*; and ***Chapter 6****: Fully Inkjet-Printed Green-Emitting PEDOT:PSS/NiO/Colloidal CsPbBr₃/SnO₂ Perovskite Light-Emitting Diode on Rigid and Flexible Substrates* showcase the results achieved with each family of devices throughout this thesis in the form of published articles. Finally, in ***Chapter 7****: Conclusions and future prospects*, a comprehensive summary of the results attained is presented, highlighting the key findings and potential future lines of research.

REFERENCES

1. Lu, K. *et al.* Solution-processed electronics for artificial synapses. *Mater Horiz* **8**, 447–470 (2021).

2. García de Arquer, F. P., Armin, A., Meredith, P. & Sargent, E. H. Solution-processed semiconductors for next-generation photodetectors. *Nat Rev Mater* **2**, 16100 (2017).

3. Zhang, L. *et al.* Advances in the Application of Perovskite Materials. *Nanomicro Lett* **15**, 177 (2023).

4. Song, L., Chen, J., Xu, B. Bin & Huang, Y. Flexible Plasmonic Biosensors for Healthcare Monitoring: Progress and Prospects. *ACS Nano* **15**, 18822–18847 (2021).

5. Liu, Y.-F., Wang, W. & Chen, X.-F. Progress and prospects in flexible tactile sensors. *Front Bioeng Biotechnol* **11**, (2023).

6. Huang, T.-T. & Wu, W. Scalable nanomanufacturing of inkjet-printed wearable energy storage devices. *J Mater Chem A Mater* **7**, 23280–23300 (2019).

7. Liu, Y., Pharr, M. & Salvatore, G. A. Lab-on-Skin: A Review of Flexible and Stretchable Electronics for Wearable Health Monitoring. *ACS Nano* **11**, 9614–9635 (2017).

8. Khan, Y. *et al.* A New Frontier of Printed Electronics: Flexible Hybrid Electronics. *Advanced Materials* **32**, (2020).

9. Frost, K. & Hua, I. "Quantifying spatiotemporal impacts of the interaction of water scarcity and water use by the global semiconductor manufacturing industry". *Water Resour Ind* **22**, 100115 (2019).

10. Zhang, Y., Liu, C., Zhu, M., Zhang, Y. & Zou, X. A review on GaN-based two-terminal devices grown on Si substrates. *J Alloys Compd* **869**, 159214 (2021).

11. Capper, P., Irvine, S. & Joyce, T. Epitaxial Crystal Growth: Methods and Materials. in 1–1 (2017). doi:10.1007/978-3-319-48933-9_14.

12. Kang, J., Koo, Y., Ha, J. & Lee, C. 41-2: *Invited Paper:* Recent Developments in Inkjet-printed OLEDs for High Resolution, Large Area Applications. *SID Symposium Digest of Technical Papers* **51**, 591–594 (2020).

13. Werner Zapka - Handbook of Industrial Inkjet Printing_ A Full System Approach-Wiley-VCH (2017).pdf.

14. Khan, H. N., Hounshell, D. A. & Fuchs, E. R. H. Publisher Correction: Science and research policy at the end of Moore's law. *Nat Electron* **1**, 146–146 (2018).

15. Leiserson, C. E. *et al.* There's plenty of room at the Top: What will drive computer performance after Moore's law? *Science (1979)* **368**, (2020).

16. Ignatov, A. *et al.* AI Benchmark: All About Deep Learning on Smartphones in 2019. in *2019 IEEE/CVF International Conference on Computer Vision Workshop (ICCVW)*

3617–3635 (IEEE, 2019). doi:10.1109/ICCVW.2019.00447.

17. Burnes, A. NVIDIA DLSS 2.0: A Big Leap In AI Rendering. https://www.nvidia.com/en-us/geforce/news/nvidia-dlss-2-0-a-big-leap-in-ai-rendering/ (2020).

18. Li, S., Li, H., Wang, Y., Liao, Y. & Yu, L. SteerNeRF: Accelerating NeRF Rendering via Smooth Viewpoint Trajectory. (2022).

19. Sebastian, A., Le Gallo, M., Khaddam-Aljameh, R. & Eleftheriou, E. Memory devices and applications for in-memory computing. *Nat Nanotechnol* **15**, 529–544 (2020).

20. Kanamoto, T. *et al.* A Single-Stage RISC-V Processor to Mitigate the Von Neumann Bottleneck. in *2019 IEEE 62nd International Midwest Symposium on Circuits and Systems (MWSCAS)* 1085–1088 (IEEE, 2019). doi:10.1109/MWSCAS.2019.8884919.

21. Zhou, Y. *et al.* Boolean and Sequential Logic in a One-Memristor-One-Resistor (1M1R) Structure for In-Memory Computing. *Adv Electron Mater* **4**, (2018).

22. Li, C. *et al.* Long short-term memory networks in memristor crossbars. *Nat Mach Intell* **1**, (2018).

23. Guo, T. *et al.* From Memristive Materials to Neural Networks. *ACS Appl Mater Interfaces* **12**, 54243–54265 (2020).

24. Lanza, M. *et al.* Standards for the Characterization of Endurance in Resistive Switching Devices. *ACS Nano* **15**, 17214–17231 (2021).

25. Lanza, M. *et al.* Memristive technologies for data storage, computation, encryption, and radio-frequency communication. *Science (1979)* **376**, (2022).

26. Zhang, Y. *et al.* Brain-inspired computing with memristors: Challenges in devices, circuits, and systems. *Appl Phys Rev* **7**, (2020).

27. Eshraghian, J. K., Wang, X. & Lu, W. D. Memristor-Based Binarized Spiking Neural Networks: Challenges and applications. *IEEE Nanotechnol Mag* **16**, 14–23 (2022).

28. Jiang, H. *et al.* A novel true random number generator based on a stochastic diffusive memristor. *Nat Commun* **8**, 882 (2017).

29. Gao, Y., Al-Sarawi, S. F. & Abbott, D. Physical unclonable functions. *Nat Electron* **3**, 81–91 (2020).

30. Legenstein, R. Nanoscale connections for brain-like circuits. *Nature* **521**, 37–38 (2015).

31. Roldan, J. B. *et al.* Time series modeling of the cycle-to-cycle variability in h-BN based memristors. in *2021 IEEE International Reliability Physics Symposium (IRPS)* 1–5 (IEEE, 2021). doi:10.1109/IRPS46558.2021.9405100.

32. Pan, C. *et al.* Coexistence of Grain-Boundaries-Assisted Bipolar and Threshold Resistive Switching in Multilayer Hexagonal Boron Nitride. *Adv Funct Mater* **27**, (2017).

33. Hui, F. *et al.* On the use of two dimensional hexagonal boron nitride as dielectric.

Microelectron Eng **163**, 119–133 (2016).

34. Yuan, B. *et al.* 150 nm × 200 nm Cross-Point Hexagonal Boron Nitride-Based Memristors. *Adv Electron Mater* **6**, (2020).

35. Lakhotia, G. *et al.* An investigation on TiO2–ZnO based thick film 'solar blind', photo-conductor for 'green' electronics. *Materials Science and Engineering: B* **168**, 66–70 (2010).

36. Jandow, N. N., Abu, H., Yam, F. K. & Ibrahim, K. ZnO Metal-Semiconductor-Metal UV Photodetectors on PPC Plastic with Various Metal Contacts. in *Photodetectors* (InTech, 2012). doi:10.5772/37963.

37. Monroy, E., Omn s, F. & Calle, F. Wide-bandgap semiconductor ultraviolet photodetectors. *Semicond Sci Technol* **18**, R33–R51 (2003).

38. Osmond, M. J. & Mccall, M. J. Zinc oxide nanoparticles in modern sunscreens: An analysis of potential exposure and hazard. *Nanotoxicology* **4**, 15–41 (2010).

39. Hippola, C. *et al.* Enhanced Light Extraction from OLEDs Fabricated on Patterned Plastic Substrates. *Adv Opt Mater* **6**, (2018).

40. Moon, H., Lee, C., Lee, W., Kim, J. & Chae, H. Stability of Quantum Dots, Quantum Dot Films, and Quantum Dot Light-Emitting Diodes for Display Applications. *Advanced Materials* **31**, (2019).

41. Singh, R. K. *et al.* Progress of Backlight Devices: Emergence of Halide Perovskite Quantum Dots/Nanomaterials. *Frontiers in Nanotechnology* **4**, (2022).

42. Dey, A. *et al.* State of the Art and Prospects for Halide Perovskite Nanocrystals. *ACS Nano* **15**, 10775–10981 (2021).

43. Jing, X., Puglisi, F., Akinwande, D. & Lanza, M. Chemical vapor deposition of hexagonal boron nitride on metal-coated wafers and transfer-free fabrication of resistive switching devices. *2d Mater* **6**, 035021 (2019).

Chapter 2
Background and State of the Art

This chapter provides an overview of the most important areas covered throughout this thesis. The first section introduces the field of printed electronics, comparing inkjet printing with the most relevant competing technologies, followed by a concise view of important parameters for successful inkjet printing. Next, the major materials and material families are reviewed (*2.2. Functional materials for solution processing*). Finally, the three device families fabricated during the thesis through inkjet printing are presented in *2.3. Selected devices*.

2.1. Printed Electronics

Growing market demands for a variety of electronic and optoelectronic devices has pushed the industry to revolutionize fabrication processes to adapt to new requirements of flexibility, wearability nanostructured materials combined with high-throughput, low-cost manufacturing. Commonly employed fabrication technologies typically rely on various vacuum deposition processes, such as evaporation and sputtering. These methods, which have been the standard for decades, can achieve high material purities and qualities of interfaces. They require, however, complex setups, expensive high purity fungible materials, have limited scalability due to the intrinsic difficulties in preparing high-volume vacuum chambers, and some steps may be incompatible with flexible substrates.[1,2] Furthermore, an extra lithography step is generally required to define the device geometry, as these deposition processes inherently deposit layers homogeneously with no defined geometry. This photolithographic process is generally subtractive, as part of the deposited material is discarded, resulting in material loss.[3]

In response to these demands, the microelectronics manufacturing industry began adapting graphics and text printing technologies to fabricate electronic devices.[4–7] Printed electronics is a term that encompasses a variety of techniques adapted for the fabrication of electronics, allowing the deposition of a variety of materials on different substrates at reduced cost and complexity,[8] and may either be a complementary process to other deposition technologies, or the sole method of fabrication for electronic devices (i.e.,

fully-printed manufacturing).

As these technologies derive from an application used to print text and graphics, they generally define the device geometry at the point of deposition, forfeiting lithographic processing steps and greatly streamlining the manufacturing process. Due to the particularities, each technology has a minimum feature size (pitch, measured in μm) and a maximum fabrication speed (measured in printed surface per unit time), which are summarized in Table 2.1. According to whether there exists contact with the substrate, printing technologies can be classified into *contact* and *non-contact* types.

Table 2.1 Properties of different printing technologies. Adapted from Refs [4,9–15].

	Inkjet printing	LIFT	Screen printing	Gravure	Offset	Flexography
Ink viscosity (cP)	5 - 50	$1 - 10^6$	500 - 5000	10 - 1000	$100 - 10^5$	50 - 500
Pitch (μm)	30 - 70	>60 μm	50 - 150	5 - 100	10 - 50	30 - 100
Film thickness (μm)	0.1 - 1	-	5 - 100	0.1 - 1	0.5 - 10	0.5 - 8
Printing speed (m/s)	1 - 10	0.08 (R2R)	0.1 - 1	0.1 - 10	0.25 - 15	50 - 500
Maskless patterning	✓	✓	✗	✗	✗	✗

Contact printing technologies, summarized in Fig. 2.1, require some form of a *mask* to define the device geometry, which needs to be manufactured beforehand specifically for the pattern at hand. This added step needs to be considered as it may be expensive and hinders workflows that require the use of different patterns (e.g. in prototyping). On the other hand, non-contact technologies, summarized in Fig. 2.2, are generally *maskless*, as they define the geometry to print by placing ink in the required positions (e.g. inkjet printing and LIFT). This kind of maskless manufacturing may also be called *digital*, as the desired pattern can be changed on the go (e.g. by loading a pattern image into a computer), making it especially appealing for fast prototyping, where several successive versions of a device might need to be tested and perfected. Another main benefit of these printing technologies is the reduced contamination of the substrate due to their non-contact nature,[16] and the wider available range of substrates that can be exploited for stretchable and flexible optoelectronics.

2.1.1. Contact printing technologies.
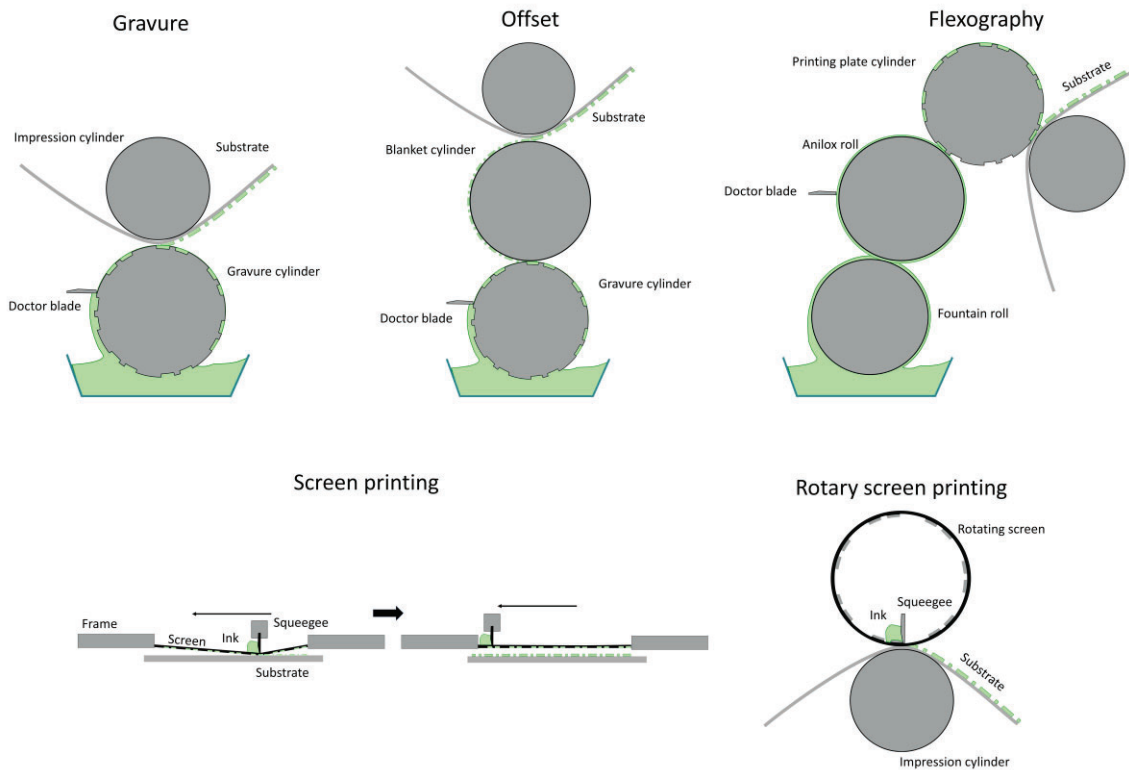
Fig. 2.1 Sketch of contact printing technologies discussed in this section.

2.1.1.1 Screen printing

Screen printing is a printing technology whose origins are in early 20th century graphic design,[17] which consists of a masked mesh that is placed on top of the receiving substrate and filled with ink. The mesh determines not only the pattern to be transferred, but also the desired layer thickness, and can be made from several materials, considering the desired accuracy, thickness, robustness and cost.[18] In order to transfer the pattern, a squeegee is dragged across the mask, forcing the paste through the openings in the mesh and depositing the desired pattern. Thus, screen printing is not considered a digital technology, as every pattern to be printed needs a specific mask.

Screen printing is generally used to print on textiles and ceramics and has been used to print a variety of optoelectronic devices and materials such as contacts,[19] LEDs and electroluminescent displays,[20–22] solar cells.[23] The achievable thickness range is usually quoted as 10-100 μm,[4] although thicknesses down to 100 nm have been reported.[23]

An R2R version of screen printing exists, called rotary screen printing, where a

cylindrical mesh is turned along the receiving substrate to print the pattern. Its characteristics are like those of flat screen printing, with the added benefit of high-speed manufacture (100 m/min).

2.1.1.2 Gravure

In gravure, the substrate to be printed is rolled between two cylinders, called impression cylinder and gravure cylinder. It is a fast method, being able to print at up to 1000 m/min. The pattern to be printed is etched as a relief on the surface of gravure cylinder, which is typically built from a hard material such as metal.[24,25] The gravure cylinder is partially submerged in an ink pool and, as it rolls, ink fills the relief pattern, with excess ink being removed by a doctor blade. The remaining ink finally arrives on the substrate, where it is deposited as the cylinder rolls. This printing action is helped by the impression cylinder, which applies high pressure (3 MPa) on the substrate.[26]

While the gravure rolls have a long usable lifetime and allow high resolutions (down to 10 μm), they are expensive to manufacture, so this technology is best suited for large production volumes.[25,27] Gravure is typically used to print on packaging[28] and has been demonstrated for the fabrication of transparent contacts,[29] solar cells,[30] OLEDs,[31] antennas,[32] and transistors.[33]

2.1.1.3 Offset

Also known as offset gravure, this method is similar to gravure with an added cylinder called blanket cylinder. This is a soft cylinder, generally built of rubber, that acts as an intermediary between the gravure cylinder and the substrate. As the cylinders roll, the pattern is imprinted from the gravure cylinder onto the blanked cylinder and finally onto the substrate.[34]

This setup achieves higher resolutions, thanks to the higher viscosity, oily inks used in addition to the strategic use of water in the negative parts of the gravure cylinder. Water is added because the hydrophobic interaction with the oily inks allows the pattern features to be transferred more sharply. However, this principle of operation also imposes further restrictions on the characteristics of the inks, limiting its applications in printed electronics.[35]

2.1.1.4 Flexography

Another variant of gravure, flexography is akin to an inverted version of offset. As opposed to offset, in flexography, the roll that collects the ink is a flat roll called the *fountain roll*. Ink is then transferred to another flat roll called the *anilox roll*, where the ink layer is flattened by a doctor blade, leaving a uniform layer. The ink is then transferred onto the *printing plate cylinder*, which is patterned. Finally, the ink is deposited onto the substrate by applying pressure with the help of an impression cylinder.

The rolls in this technology are built from soft materials, such as plastics or rubber, making the patterning process considerably cheaper. However, this also means that the patterns on the rolls can be damaged, limiting their resolution and lifetime.

Flexography is generally destined for printing in packaging, and has been demonstrated to fabricate antennas[36,37] and transport layers for OLED.[38,39]

2.1.2. Non-contact printing technologies
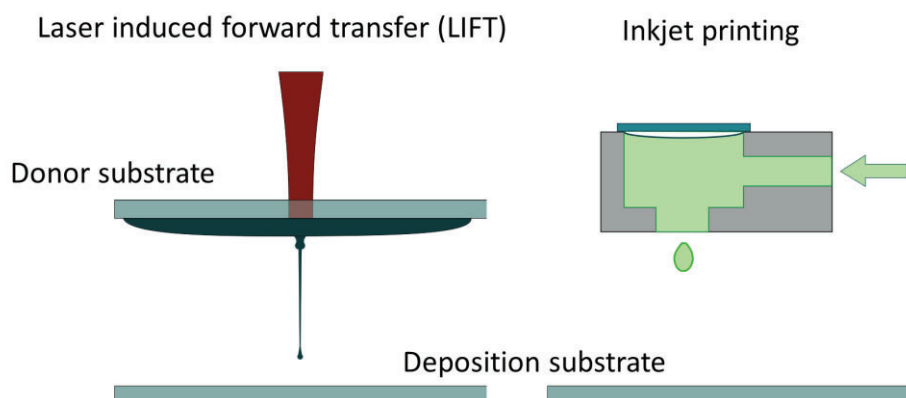
Fig. 2.2 Sketch of non-contact printing technologies discussed in this section.

2.1.2.1 Laser Induced Forward Transfer (LIFT)

LIFT is a printing technology that is comparable to a nozzle-less alternative to inkjet printing. The typical setup in LIFT consists of an acceptor substrate, a donor substrate where a layer of ink is spread, and a laser source that is generally pulsed, but may also be continuous wave.[40] The laser is impinged on the ink layer at the donor substrate, creating a local zone of heating. The energy transferred is sufficient to induce localized boiling of the ink, which generates a rapidly expanding bubble of gas. As this bubble expands, ink is ejected in a jet shape, which travels towards the substrate, depositing the material.

To define the pattern to print, a micro-positioner setup, a scanning (galvanometric) setup or a digital micromirror device (DMD) may be used.[41] Thus, LIFT is a digital printing technology, as it can generate arbitrary patterns without the need to fabricate a mask. While not established as a commercial technology compared to inkjet, with most setups being produced in-house by research groups, it provides the printing capabilities of inkjet with some benefits.

LIFT is a nozzle-less technology. This removes some restrictions in terms of ink availability, present in inkjet printing. Most notably, viscous (e.g. screen printing) inks,[42] large particle sizes, and suspensions of high aspect ratios such as nanowires[43] can be successfully printed. Additionally, the absence of a nozzle eliminates problems such as clogging. Despite these promising properties, its commercial application in a roll-to-roll process is still limited, with one known example of a LIFT implementation.[10]

2.1.2.2 Inkjet Printing

Inkjet printing is a commonly used technology in the graphics and arts industry thanks to its adaptability and scalability. Inkjet printing is a digital printing technology, able to print an arbitrary pattern with no need to use masks or other lithographic processes. It is based on a movable printing head which contains several ink-ejecting nozzles and an ink deposit. Ink transfer is achieved by ejecting ink droplets from the nozzle onto the substrate as the printing head scans the printing area.

This controlled deposition mechanism makes inkjet printing incredibly material efficient, as material is only deposited where it is needed, with a negligible amount of ink lost in occasional maintenance purges of the cartridge. Inkjet printing can achieve high printing speeds across wide substrates. Thanks to the non-contact nature of inkjet printing, there are few restrictions on substrate choice. Furthermore, inkjet printing can be part of an R2R process.

Compared to offset and screen printing, the required ink viscosity for inkjet printing is not high, its achievable resolution is adequate, and thanks to its digital nature it does not suffer from registration problems,[16] all in addition to its maskless nature.

Despite the advantages of inkjet printing, some possible issues should be considered. Due to ink rheology requirements, low boiling point solvents are commonly used in inkjet

printing inks. This may lead to clogging problems as part of the solvent of the ink remaining in the nozzle can evaporate prematurely. This issue is can be solved easily by proper cleaning and care of the state of the nozzles. At the same time, undesired effects due to fast evaporation of solvents can lead to the formation of a *coffee ring* in the printed layer, a well-known phenomenon that creates inhomogeneity in final layer thickness.

Two main families of inkjet printer can be differentiated in terms of droplet ejection control (continuous drop vs. drop on demand, Fig. 2.3), and further into two types in terms of ejection mechanism (thermal and piezoelectric, Fig. 2.4).

►   Drop on demand vs continuous drop.

Drop on demand technologies can interrupt or activate the jetting process at the nozzle, thereby determining when drops are transferred into the receiving substrate (Fig. 2.3 a). In contrast, continuous dropping is characterized by a non-stop repeating ejection of droplets as the printing head is functioning. Drop deposition is determined by electrically charged plates that deviate unwanted drops into a collection element, while drops that are let through are be deposited (Fig. 2.3 b).
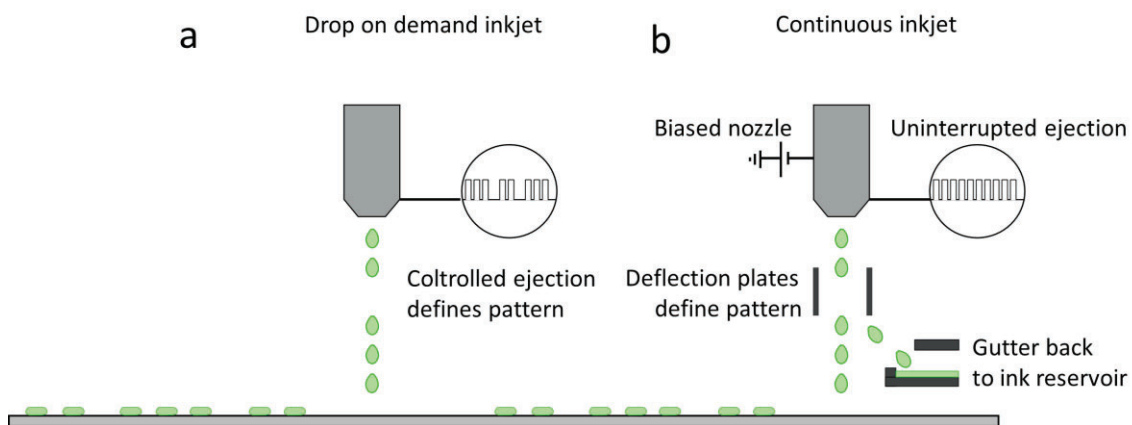
Fig. 2.3 Inkjet printing technology according to jetting control (a) drop on demand (b) continuous inkjet.

►   Thermal vs piezoelectric actuation

In thermal jetting systems, a rapid-heating element heats a spot in the ink chamber, producing a rapidly expanding bubble of evaporated liquid (Fig. 2.4 a). This rapid expansion forces a volume of ink outwards, forming a jet that travels towards the receiving substrate. The main drawback of this inkjet technology is the thermal stress

placed on the ink, as it is exposed to temperatures of up to 400 ºC, which limits the choice of inks.[44]

In contrast, piezoelectric printheads use the deflection of a piezoelectric element (Fig. 2.4 b). A pulsating electric potential is applied on the piezoelectric element inducing a rapid deformation, which forces a volume of ink outwards. Being a mechanical process, a wider variety of ink rheologies are accepted, the ink is subjected to lower stress, and the printing head has a longer usable life.[45]

Thermal actuation | Piezoelectric actuation

Heating element causes displacement due to localized vaporation

Piezoelectric element causes displacement due to deformation
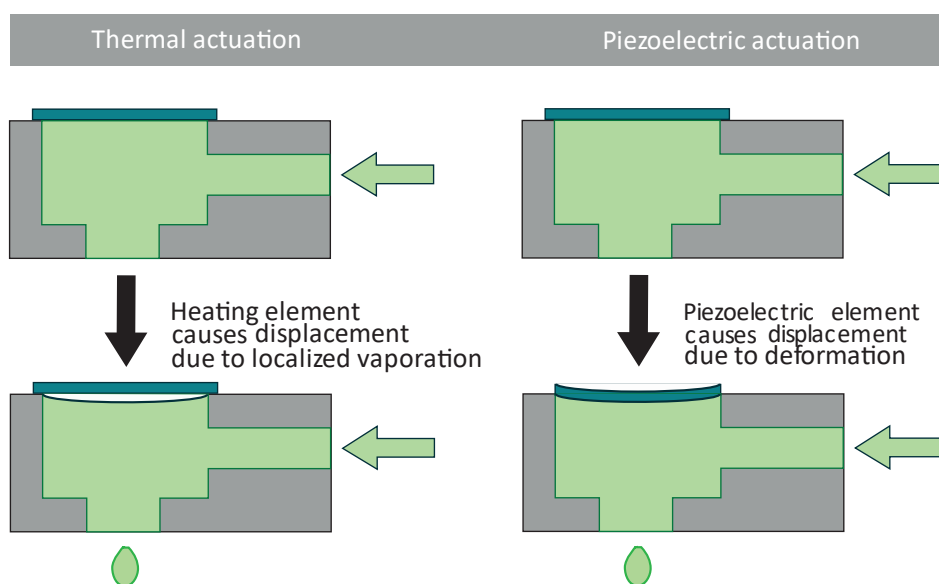
Fig. 2.4 Two most common mechanisms for jetting: thermal actuation and piezoelectric actuation.

2.1.2.3 Ink requirements for inkjet printing inks

When designing an ink for use in inkjet printing, there are some parameters that must be considered. Like other solution processing technologies, inkjet printing is feasible for a range of ink rheologies. While the exact physical interactions are complex, the theoretical and practical limits of inkjet printing have been studied extensively in the past. In this section, an overview of the most important parameters and conclusions will be presented.

The main parameters that describe the rheology of a fluid are surface tension, viscosity, and density (γ, η, ρ, respectively). Surface tension (γ) is related to the energy required to increase the surface area of a liquid. This energy requirement is a consequence of the intermolecular forces at the surface of a liquid interface. For a liquid in contact with

air, the liquid molecules at the surface experience a net force towards the bulk, arising from cohesive attraction. This results in the liquid attempting to minimize its interface surface area, which plays a role in droplet formation and ink-substrate wetting. Viscosity (η) is related to the fluid's resistance to flow, arising from internal forces of friction. Density (ρ), as a measure of a liquid's mass per unit volume, is related to inertial effects.

One crucial aspect in inkjet printing is achieving proper, stable drop formation.[46] If the drops are unstable, obtaining a homogeneous thin layer will be challenging. In order to understand the stability of drop formation inkjet printing, these three parameters (γ, η, ρ) are reduced into a figure of merit called the Z number, which equal to the inverse of the Ohnesogre (Oh) parameter[47] (eq. 2.1).

$$Z = \frac{1}{Oh} = \frac{\sqrt{l\rho\gamma}}{\eta} = \frac{Re}{\sqrt{We}} \qquad \text{(eq. 2.1)}$$

This parameter was first proposed by Fromm, [48] and predicts an ideal range of drop formation: at low values of Z, the ink is too viscous to induce jetting, and at high values multiple satellite drops occur. Although Fromm's initial analysis concluded that a value of Z>2 was required, later authors have proposed, empirically and numerically, a Z number within the range 1-4<Z<10-14,[49,50] where a low Z number leads to no jetting, and a high Z number leads to satellite droplets (Fig. 2.5). However, the Z number alone is not enough to determine the printability of an ink, as it does not consider the speed of droplet ejection. This is an important factor whose effects are twofold.
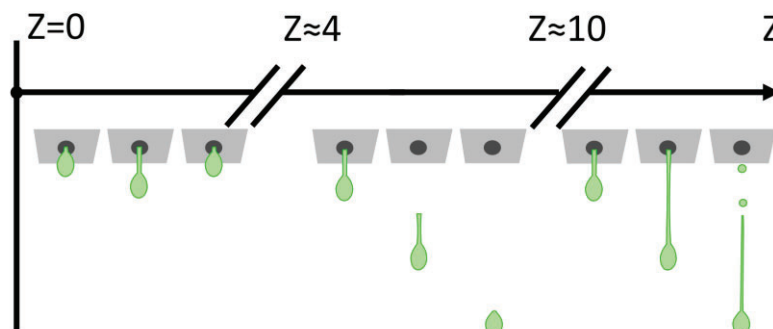
Fig. 2.5 Sketch of effect of Z number on jetting dynamics.

Firstly, for the drop to be formed, it must overcome the ink/air surface tension at the nozzle. As mentioned earlier, a liquid generally tends to minimize its surface area, as that increases its energy; since the formation of a droplet increases the surface area with respect to the resting state, this process requires energy. This condition leads to a requirement of minimum ejection velocity as a function of the nozzle diameter d_n and surface tension γ (eq. 2.2)(eq. 2.2), that can be expressed in terms of the Weber number[51] (eq. 2.3)(eq. 2.3).

$$v_{min} = \sqrt{\left(\frac{4\gamma}{rd_n}\right)}$$
(eq. 2.2)

$$We = v_{min}\sqrt{\left(\frac{rd_n}{\lambda}\right)} > 4$$
(eq. 2.3)

Secondly, droplet splashing upon impact with the substrate, which may happen at high speeds (Fig. 2.6), should be avoided. Empirical studies [52] suggest that the onset of splashing can be represented with a condition that relates the Weber and Reynolds numbers, and f(R), a function of surface roughness, with a dimensionless scalar value approximately equal to around 50 for flat, smooth surfaces [53]. Thus, for smooth surfaces, the condition for splashing can be described as follows (eq. 2.4):

$$\sqrt[2]{We} \cdot \sqrt[4]{Re} > f(R) \approx 50$$
(eq. 2.4)
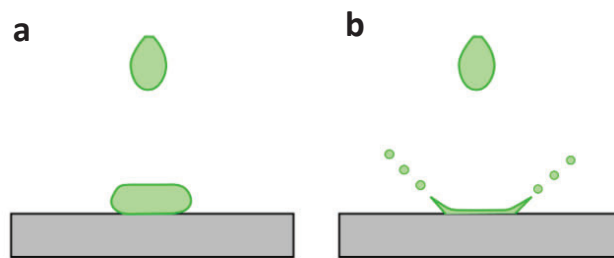
Fig. 2.6 Sketch of droplet impacting the substrate in (a) ideal conditions and (b) at the onset of splashing in non-ideal conditions.

With these conditions studied, the printable bounds achievable by inkjet printing can be represented graphically. This is generally shown as a region in a log-log 2D parameter space with coordinates of Weber and Reynolds numbers, seen in Fig. 2.7. In this plot, loci of constant Z number appear as diagonal lines with positive slope (center of figure). The condition of minimum ejection velocity appears as a horizontal boundary (gray region

below We≈4), and the condition of onset of splashing appears as a line of negative slope (top right of figure). The center area represents the printable range of ink rheologies and drop velocities.
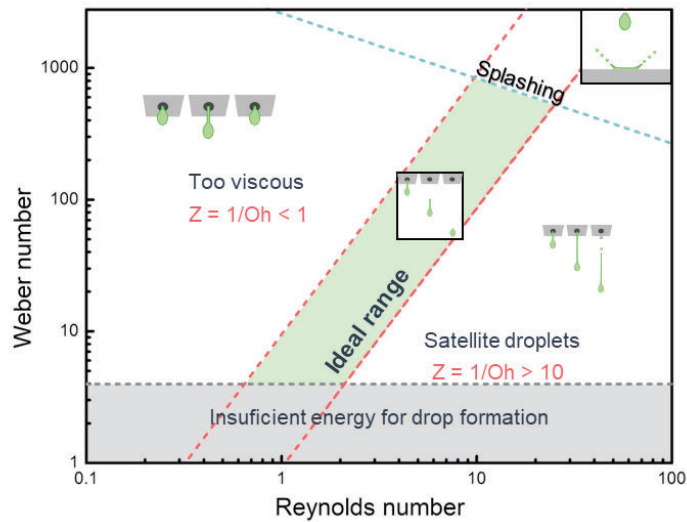
Fig. 2.7 Plot of ideal range of printability related to the figure of merit Z and the conditions for insufficient energy for drop formation and the onset of splashing.

► Ink-substrate interactions

Wetting is the ability of ink to spread across a substrate. This is mainly a function of the surface energy of the ink in relation to that of the substrate. The lower the surface tension of the ink in comparison to the substrate, the better the wetting becomes.[54] The wetting properties of an ink on a substrate may be evaluated by a contact angle test, without the need to measure the surface tension explicitly, with lower contact angles indicating better wetting ability. In fact, the cosine of the contact angle is a linear function of the surface tension of the liquid for a constant substrate. This relationship may be plotted in a Zisman plot in order to find the critical surface tension γ_c, which is the surface tension beyond which complete wetting is achieved (contact angle $\theta = 0$).[54] It should be noted that perfect wetting is not necessarily the optimal condition for inkjet printing, as a non-zero contact angle with optimized contact line pinning (i.e., the wet layer radius shrinks at a controlled rate) allows the formation of a well-defined, thick wet layer.[55–57] As contact angle nears 0, the wet layer becomes thinner, as does the resulting thin film (Fig. 2.8).
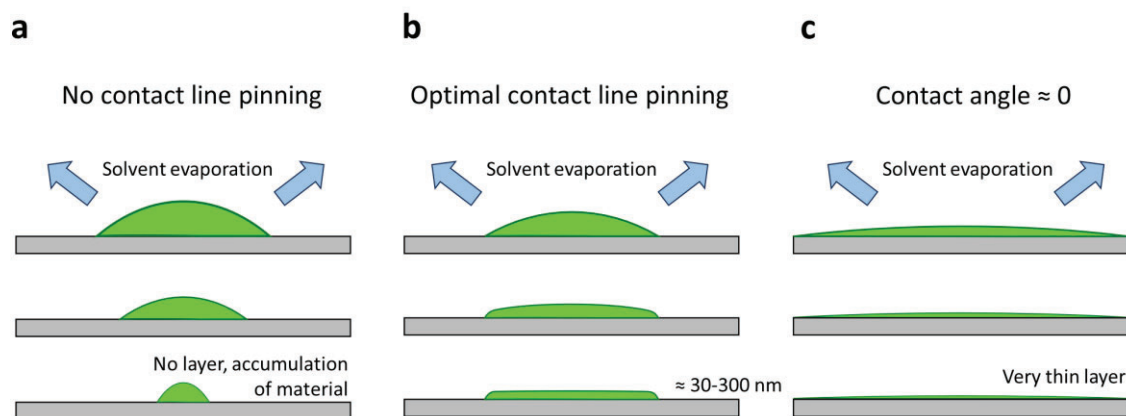
Fig. 2.8 Sketch of resulting film morphology in three general scenarios: (a) no contact line pinning, resulting in material accumulation and no layer formation, (b) optimal line pinning and non-zero contact angle, resulting in a well-defined layer morphology, (c) contact angle nearing 0 (complete wetting), leading to a very thin film.

Since wetting is a function of the difference in surface tension between the ink and the substrate, it may be improved either by manipulation of the ink formulation or by treatment of the substrate. For inks, their surface tension may generally be reduced by adding surfactants or low-surface tension solvents to the formulation.[58] Otherwise, the substrate can be treated in several ways in order to increase its surface energy, including chemical treatments (cleaning with detergents, solvents, and/or other chemicals), plasma treatments and UV/ozone treatments.

When a droplet (or printed area) dries on a substrate, the evaporation of the solvents undergoes a complex process. Generally, evaporation happens at a faster rate at the edges of the droplet. This uneven evaporation induces currents within the wet layer that drag the solid content of the ink towards the edges, causing an accumulation of material as the solvents dry,[59] commonly known as coffee ring effect. This effect is particularly present in inkjet printing due to the relatively low viscosities of the printable inks (2 - 20 mPa·s)[60].

The coffee ring effect may be counteracted in different ways. The most used approach is the incorporation of a solvent with a higher boiling point and lower surface tension.[61] As the solvent with lower boiling point evaporates faster, a surface tension gradient is established, creating a flow that opposes and counteracts the original flow. This principle will be shown in the $CsPbBr_3$ ink formulation used for the fabrication of LEDs in **Chapter 6**. The formulation of the ink is based on a specific ratio of high- and low-boiling point (dodecane and hexane) that ensure flat, homogeneous layers.

2.1.3. The role of solution processing in manufacture

As discussed earlier, printing offers substantial advantages, including high throughput, lowered cost of materials, and in the case of inkjet printing, maskless fabrication.

In vacuum-based deposition, the sample is placed in a vacuum chamber that contains either a target of the material to be deposited (e.g., physical vapor deposition methods such as thermal evaporation, electron beam evaporation, sputtering, etc.), or precursors to synthesize it (e.g., in chemical vapor deposition methods). Once a sufficiently high vacuum has been achieved (10^{-4} mbar to 10^{-8} bar, depending on the process), deposition can begin. Vacuum deposition methods have reigned as the preferred method of deposition for commercial fabrication of devices such as OLEDs,[62] even as solution processing methods are being studied.

There are multiple reasons vacuum evaporation has remained the main method of fabrication in many fields. In comparison to solution processing methods, vacuum deposition methods achieve very pure layers, thanks to a combination of factors. On the one hand, high vacuum protects the samples from atmospheric contaminants such as oxygen, moisture, and other chemical species,[63,64] and dust particles. On the other hand, since solvents aren't involved in vacuum-based deposition, the final layer is better ensured to be pure in contrast to solution-based routes, as solvents can be hard to completely remove afterward [65]. In addition, fine control of layer thickness can be easily guaranteed, and layer intermixing is not as big a concern. As a result, vacuum evaporation processes are free from constraints such as the choice of solvents, the solubility of the materials, solvent orthogonality, compatibility of rheology and interaction of successive layers.

The tradeoff of solution processing for this reduced control of layer properties is not only a considerable decrease in materials cost but also an increase in throughput. Moreover, solution processing enables the deposition of upcoming promising materials that would be impracticable otherwise. Indeed, this aspect of solution processing will be showcased in the fabrication of h-BN memristors (***Chapter 4***). Vacuum processes can be used to deposit h-BN, but require very high temperatures (>850 ºC),[66] reducing

compatibility with other substrate materials and previous processes. However, this can be avoided by exfoliating 2D h-BN nanosheets and depositing through a solution processing route. Solution processing routes also allow the use of nanocrystals, which, in the case of metal oxides, allows thin film fabrication with post-processing temperatures below 200 ºC, enabling compatibility with flexible substrates and other temperature-sensitive materials (*Chapter 5*). When fabricating perovskite-based devices, solution processing promotes maximum quantum yield thanks to the increased resilience of the perovskite material against defects in QD form (*Chapter 6*).

It is important to note that market pressures might not necessarily demand for the complete incorporation of inkjet printing as a material deposition technology, since traditional semiconductor materials and processes still offer unparalleled integration density and performance for most applications. Rather, inkjet printing comes as a compelling alternative for certain fabrication steps, where its flexibility in material choice and low cost offer a comparative advantage compared to other technologies.[67–70] Besides for fast prototyping applications, inkjet printing brings the possibility of depositing conventional and innovative materials (e.g. from metals to 2D nanoflakes) in a variety of rigid and flexible substrates. While standard forms of inkjet printing are generally limited to a line width of 5 μm, there is a growing market of devices that do not require higher integration density. In addition, specialized inkjet printing setups may reach feature sized below 1 μm,[71] enabling high precision manufacturing.

2.2. Functional materials for solution processing

This presents a pragmatic perspective on the properties of various materials and material families discussed in this thesis with a focus on their application in inkjet printing, in their respective order of appearance. Emphasis will be placed on exploring the practical advantages and challenges associated with their implementation in device fabrication, briefly addressing their physical and electrical properties.

Contacts and interconnects can be inkjet-printed from metal nanoparticle inks that are readily available from commercial distributors, as demonstrated in this thesis with h-BN memristors (*Chapter 5*). However, attempts to obtain photodetectors or PeLED devices with inkjet-printed top contacts were not successful in this thesis. Possible

explanations include percolation of metallic species or solvents inside the device structure, causing damage or shunting the device. For this reason, evaporated metallic contacts (PeLEDs) and carbon paste contacts (in the case of NiO/ZnO photodetectors) were used instead.

2.2.1. Hexagonal boron nitride (h-BN) ink

Hexagonal boron nitride (h-BN) is a 2D layered material with a structure analogous to graphite consisting of stacked hexagonal layers weakly bonded by Van der Waals forces in the vertical direction[72,73] that is receiving attention from researchers due to its unconventional properties.[74] The electrical properties of h-BN are remarkable, being a very effective electrical insulator, it exhibits a wide indirect bandgap of ~6 eV,[75] has a high dielectric constant (k = 4-6), and high resistance to the diffusion of chemical species.[76,77] This combination of properties has led to its proposed use as an insulator material in transistors,[78] in high energy density capacitors,[79,80] for encapsulation of high-power devices[81] and a variety of photonics applications.[82] In addition, thanks to its chemical robustness and atomically flat surface free of dangling bonds and charged impurities, it has been particularly hailed as an excellent encapsulating material for other 2D materials.

Traditional deposition methods, such as CVD, may be used to fabricate large-area 2D h-BN films. However, this requires high temperatures (>850 ºC), which is incompatible with most of CMOS processing which, depending on the specific materials and devices, has a limit of 200 ºC-500 ºC.[83–86] In case of incompatibility with CVD deposition on a particular substrate, a cumbersome transfer process of the h-BN layer is required, which may cause cracks and other faults.[87,88] In order to circumvent these stringent manufacturing constraints, h-BN can be fabricated in the form of 2D nanosheets by liquid phase exfoliation in a similar fashion to graphene. This enables the use of scalable solution processing routes such as inkjet printing to deposit h-BN without recurring to high temperature processes.[89]

One of the challenges in the fabrication of memristors is the limited endurance of most structures. In comparison to other materials used in M-I-M memristors, liquid-phase exfoliated h-BN provides a unique combination of wide bandgap, high dielectric strength,

chemical stability, conferring h-BN memristors high endurance,[90,91] and compatibility with low-temperature processing techniques. These characteristics make h-BN an enticing candidate for various applications, including memory devices, neuromorphic computing, and flexible electronics.[88]

When applied for memristors, h-BN has achieved high resistance state ratios and low-power consumption.[92] While, as a 2D material, h-BN has a low density of defects and is very flat,[91] its grain boundaries have been found to promote hot spots, limiting the propagation of dielectric breakdown, enhancing the endurance of the memristor.[91] In addition, while random telegraph noise (RTN)from traditional MIM metal oxide structures is unstable, the native defects in multilayer h-BN improved RTN stability as they limit lateral propagation.[93]

In this thesis, liquid phase exfoliated h-BN is inkjet-printed to fabricate Ag/h-BN/Pt and Ag/h-BN/Ag memristors that show promising qualities for security applications.

2.2.2. Metal oxide inks

Large area, transparent semiconducting thin films are needed for a variety of applications where electronics interacts with light, such as displays, LED panels, and solar cells. Because successful application in these fields requires large scale homogeneity polycrystalline materials such as p-Si, which show inhomogeneity and problems with grain boundaries, are not optimal.[94] In addition, mechanical flexibility is generally required, thus excluding single crystalline materials.[94] In response, materials such as amorphous hydrogenated silicon (a-H:Si) arose as key materials for solar cells and displays thanks to its homogeneity. However, a-H:Si is restricted by its limited carrier mobility and lack of mechanical flexibility.[95,96] The development of OLEDs in the late 20th and early 21st century brought forth a myriad of organic charge transport materials, which have been borrowed for use in the perovskite LED and solar cell fields. Thanks to the maturity of the OLED field, organic materials are a known way to provide high efficiencies to LEDs and solar cells. However, their high cost and limited stability are cause of concern,[96–98] compelling researchers to discover better alternatives.

While the first reports of the electrical properties of conductive oxides start in the 1950's,[94,96] interest started forming around the electronics applications of metal oxides in

the early 2000's, when T. Kamiya and H. Hosono reported results on large-area Indium Gallium Zinc Oxide transparent thin film transistors (TFTs). As a result, metal oxides became a key component of display applications.[99,100] Thanks to their combination of transparency, conductivity and flexibility, metal oxide films have been extensively used as transport materials in LED and photovoltaic devices.[101,102] In addition to these properties, the attention that metal oxides have received as an alternative family of materials for charge transport applications is explained by their increased chemical stability and carrier mobility in comparison to organic materials, while having facile and cost-effective solution processability.[97]

The apparently contradictory combination of electrical conductivity and optical transparency that many metal oxides display originates from their electronic configuration and the interaction between orbitals in the metallic and oxygen species.[103] In comparison to other materials, metal oxides display high degrees of ionicity because of the disparity in electron affinities between the metal and oxygen species, which leads to a conduction band minimum (CBM) mainly determined by the cation and a valence band maximum (VBM) mainly determined by the anion. In this structure, the CBM is mainly influenced by metallic s orbitals, which are spherical, and thus have low curvature. This leads to low electron effective masses in metal oxides, and thus high mobilities for electrons.[94] This explanation can be generalized for all main-group metals, and most transition metals.[96]

While this structure promotes high electron mobilities, the same doesn't apply for holes. In the case of holes, the VBM is formed by p orbitals with localized states, leading to less efficient conduction mechanism by hopping,[94] leading to a lack of p-type metal oxide materials[96] As a corollary, this particularity means that transport properties in amorphous metal oxide materials are not as pronouncedly inferior compared to the crystalline material. In the case of covalent semiconductors such as amorphous hydrogenated silicon (a-Si:H), sp^3 or p bonds dominate. These bonds are comparatively much more directional and, in amorphous structures, form deep and highly localized states beyond the CBM and VBM that lead to carrier trapping.[94]

Metal oxide processing is facilitated by nanoparticle suspensions, which provide a

way to reduce post-processing temperatures compared to precursor solutions.[104,105] A variety of processes have been developed to obtain metal oxide nanoparticles,[106,107] of which spray pyrolysis is attractive due to its simplified process[107] and potential for mass production.[106]

Following, the most successfully employed metal oxides throughout this thesis will be introduced.

2.2.2.1 Zinc oxide (ZnO)

ZnO is a wide, direct bandgap semiconductor that boasts a high bulk electron mobility (200 $cm^2V^{-1}s^{-1}$)[108] and high transparency to visible light. It is an extensively studied material thanks to its breadth of applications in a multitude of fields, including skin products, the food industry, optoelectronics,[109,110] and shows high abundance in nature, low toxicity,[111] and facile synthesis routes.[112,113]

ZnO predominantly presents itself in a hexagonal wurtzite configuration owing to the stability of this phase. However, ZnO may be stabilized in a cubic zincblende structure, particularly if deposited on a substrate of the cubic system.[114] ZnO is generally intrinsically n-doped because of its tendency to contain Zn-interstitial defects and oxygen vacancies.[115,116] On the contrary, p-type ZnO is difficult to obtain due to self-compensation of native Zn defects.[117,118]

Great interest developed in ZnO in the late 20th century due to its potential use in blue-UV LED homojunction devices. However, due to the difficulty in achieving p-type ZnO, this role was finally taken by GaN homojunctions,[119] with which high luminance blue LEDs were finally achieved in the early 90's.[120] Nonetheless, thanks to ZnO sharing similar lattice parameters to GaN in the wurtzite structure, ZnO has been demonstrated as a supplementary material in GaN-based LEDs.[118] Other applications of ZnO include rare-earth LEDs,[121] photodiodes, and transistors.[122]

Thanks to its band alignment with emissive materials and its deep valence band, which enables its use as a hole blocking layer, ZnO has recently been used as an electron transport layer material (ETL) for LEDs,[123–126] pushing to achieve high luminance values.[108] However, while ZnO has been regarded as one of the best inorganic ETLs for high performance QLEDs,[127,128] some concerns for its application in the field of

perovskite optoelectronics have been raised due to its tendency to de-protonate organic perovskites, which warrants attention in device engineering.[129–131] In addition, ZnO is believed to promote exciton quenching due to nonradiative recombination in intragap states arising from oxygen vacancies,[127,132,133] and through Auger recombination, which is enabled by the band alignment of ZnO with the emissive layer, facilitating interfacial charge transfer.[132] Some groups have ameliorated this quenching by including ZnMgO or an interfacial layer.

Despite their high performance, ZnO-based LEDs tend to show irregular stability[134,135] and, to show best performance results, require undergoing a process known as *positive aging,* where they are stored for up to months before measurement[128].

2.2.2.2 Tin oxide (SnO₂)

Similarly to ZnO, SnO_2 is a non-toxic, abundant[136] direct, wide-bandgap n-type semiconductor ~3.6 eV.[106,137138] Its naturally occurring crystalline structure is a tetragonal rutile structure.[139] Thanks to its deep conduction band level, it has potential as a hole blocking layer for LED structures.[140]

While SnO_2 has been extensively used for chemical and gas sensors,[141–144] its first successful application in solar cells in 2015 sparked interest in its optoelectronic applications,[145,146] being more recently used as an electron transport layer for LEDs.[128,140,147] SnO_2 has been considered as an alternative ETL to ZnO thanks to its similar electron mobility and lower charge carrier density which implies a lowered amount of nonradiative recombination,[127] while having a higher CBM which may improve charge injection,[134] being more photostable and chemically robust than ZnO for PeLEDs[148–150] and not showing the light soaking effect of ZnO in solar cells.[136,150] In addition, SnO_2 shows a lower trap density compared to ZnO, resulting in reduced exciton quenching.[150]

2.2.2.3 Nickel oxide (NiO)

NiO is one of the few intrinsically p-type metal oxides. Thanks to its hole injection properties, relatively low trap density, and stability in ambient conditions, NiO is an interesting inorganic material for optoelectronic devices, particularly PeLEDs,[151–156] and other device families. It has a large direct bandgap (3.6-4.3 eV), and thanks to its deep

conduction band at -1.8 eV [107] it can be used as an electron blocking material in LEDs. In stoichiometric form it is considered a Mott-Hubbard insulator[107]. However, when it presents defects in the form of nickel vacancies, it displays p-type behavior,[157,158] being one of the few intrinsically p-type metal oxides.[107]

NiO has been incorporated in a variety of LED families devices (PeLED, OLED, QLED) and solar cells.[159–164] While PEDOT:PSS is one of the reference hole transport layer (HTL) materials used in LEDs, NiO is being considered as a more stable, inorganic alternative in OLED and QLED. Thanks to its higher work function (WF), it shows higher stability compared to organic HTLs; particularly in perovskite devices, low WF charge transport materials tend to induce halide migration.[165]

In the case of perovskite LEDs, the objectives of this thesis place fabrication constraints on the design of the materials. One such requirement is the fully-inkjet fabrication of devices on flexible substrates, which restricts post-processing temperatures according to the most sensitive components, in this case the perovskite material and the flexible substrate. Until recently, most proposed metal oxide inks have been based on precursors, requiring high temperatures of up to 400 ºC.[104] In contrast, most transparent flexible substrates undergo morphological and color changes at temperatures above 200 ºC (PET, PEN, PPS), precluding the use of flexible substrates and sensitive perovskite materials. This temperature requirement can be lowered by using nanoparticle-based metal oxide inks, which enable lower post-processing temperatures.[105]

2.2.3. Organic materials

Organic materials are a family of materials formed by chains of carbon atoms bonded to other elements such as hydrogen, oxygen, and nitrogen. Organic materials are an interesting option for large area, flexible device fabrication, since they are naturally homogeneous, thanks to the lack of grain boundaries, their flexibility,[166,167] and, for many of them, compatibility with solution processing methods.[167,168] In addition, thanks to the configurability of organic chemistry, the properties of organic materials can be tightly tuned to the requirements of the application.[166,169] Indeed, they have been extensively used in the field of OLEDs, which has been demonstrated since the late 80's.[170] Thanks to the maturity of this field of research, there is a great selection of established organic

charge transport materials that can be used for exciton recombination LED structures.

In the context of optoelectronic device manufacture they can be classified into polymeric and small molecule materials. Small molecule materials have a well-defined molecular size, which provides them with more predictable properties and lower device-to-device variability in contrast to the relatively more stochastic nature of polymeric materials.[171] Although they may be adapted to solution processing, small molecule materials are generally deposited through vacuum evaporation,[172] being polymeric materials better suited to solution processing routes.[173,174]

However, organic materials have some disadvantages that must be considered for potential applications. The charge carrier mobilities of organic materials tend to be lower than their inorganic counterparts. This is because, in contrast to the band-based conduction mechanisms in inorganic materials, conduction in organic materials tends to be related to hopping mechanisms between localized states.[169,175,176] Furthermore, organic materials have relatively weak intermolecular bonds, resulting in compromised long-term stability and lower tolerance to stress.[169]

In this thesis, organic materials have been used in the fabrication of perovskite LEDS (more information in *Chapter 7*) due to their properties and status as reference materials for LED fabrication. Among other organic materials, poly(3,4-ethylenedioxythiophene) polystyrene sulfonate (PEDOT:PSS) was inkjet-printed for perovskite LEDs.

2.2.3.1 poly(3,4-ethylenedioxythiophene) polystyrene sulfonate (PEDOT:PSS)

PEDOT:PSS is a polymer blend that is highly conductive, transparent, mechanically flexible, has a long carrier diffusion length, is thermally stable and is inexpensive.[177] Thanks to this favorable combination of properties, it has extensively been used to obtain high-performance devices in the fields of photovoltaics, transistors, sensors, LEDs and displays, typically used in the form of a water-based ink solution. [177]

Its chemical structure consists of the conductive component PEDOT conjugated with PSS, a surfactant that facilitates dispersion in solvents.[177,178] First commercialized by Bayer, it is currently distributed by Heraeus and Agfa in various formulations and tradenames, including: Clevios PH500 and PH1000, highly conductive, and Clevios P VP a.i. 4083 (used in this thesis), less conductive, commonly used as a p-type injection

transport material in optoelectronic devices. This gives PEDOT:PSS formulations the flexibility to be used either for flexible contact[179–182] or for transport layer applications.[183,184] PEDOT:PSS can be deposited by a variety of standard solution processing techniques, including inkjet,[185–188] and can be manufactured into a uniform and smooth layer (<5 nm).[177] Although generally deposited by spin coating in the literature, high quality inkjet-printed PEDOT:PSS thin films have been obtained in this thesis Fig. 2.9.
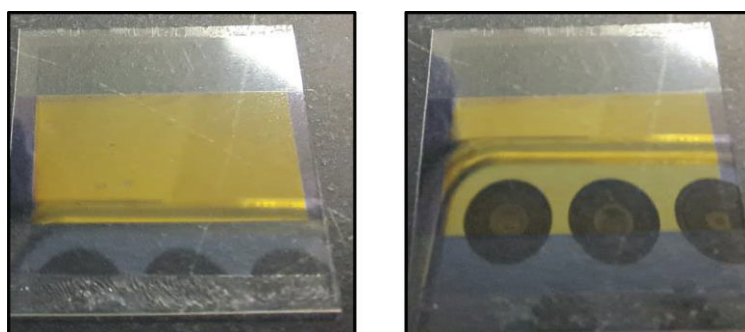
Fig. 2.9 High quality, well-defined PEDOT:PSS layers deposited through inkjet printing on flexible PEN substrate. The square substrates measure 2 cm.

2.2.4. Perovskites

Perovskites are a class of materials with the general formula ABX_3, named after the Russian mineralogist Lev Perovski. This is an extensive family of materials, with varied structures displaying a wealth of physical properties.[189] First extensive studies of perovskite materials come from the 1920's, when the founder of crystal chemistry, V.M Goldschmidt, set out to study the structure of a variety of synthetic perovskites in the early days of powder x-ray diffraction.[189] Since, perovskite materials have long been known for their diverse properties such as high dielectric constants, ferroelectricity and superconductivity.[189–191] More recently, metal halide perovskites (MHP), a subset of perovskite materials, have attracted interest as promising materials for optoelectronics, including LEDs, solar cells, waveguides and laser sources etc.[192–205]

MHPs follow the general formula ABX_3, where A^+ is generally a large ion (Cs^+, $CH_3HN_3^+$, $CH(NH_2)^{2+}$) and B^{2+} (Pb^{2+}, Sn^{2+}, Ge^{2+}) are cations bonded to X^-, a halide, leading to a crystalline structure formed by a cubic lattice with corner-sharing $[BX_6]^{4-}$ octahedra (Fig. 2.10).[206] These octahedra leave a wide empty space, leaving room to the

large A^+ cations.[207] Depending on this A^+ cation, metal halide perovskites (MHP) are classified into organic-inorganic hybrid halide or inorganic metal halide perovskites. Inorganic metal halide perovskites in particular have received interest thanks to their improved stability compared to their organic counterparts.[154,208,209] In LED applications, MHPs may be used either as electroluminescent layers or as color conversion materials for LCD backlights,[210,211] in a similar manner as QLED displays. f
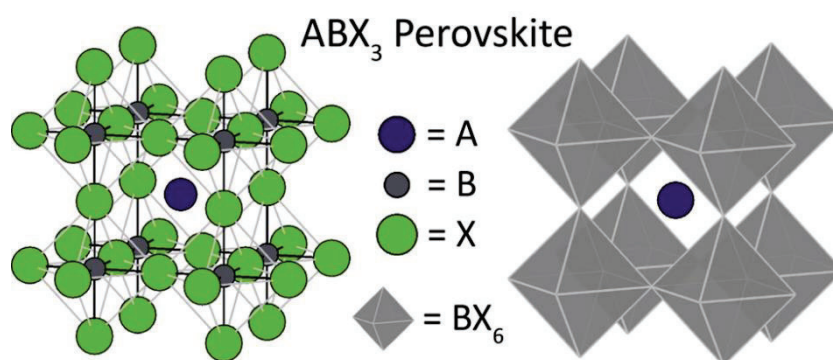
Fig. 2.10 Schematic structure of cubic ABX_3 perovskite crystalline structure, showing atom arrangement and $[BX_6]$ octahedra. Reprinted from *Ref* [206] .

Perovskite-based LED (PeLED) research is a rapidly growing field. From first reports in the 1990s,[212,213] PeLEDs have developed at an astonishing rate, catching up to organic LEDs and chalcogenide QD-based LEDs.[214] Considering spin coating, a small area fabrication process, PeLEDs have seen an increase from 0.1% efficiency in 2014 [214] to over 28% in 2022.[215] Interest and research progress in perovskites and related materials (e.g., transport layers) is compounded thanks to its intersection with the field of photovoltaics: first reports of perovskite-based solar cells appearing in 2006,[216] perovskite solar cells have also showed impressive progress until the present, with efficiencies nearing 26%.[217]

2.2.5. Inorganic metal halide perovskite QDs

Colloidal QDs have gained popularity in the last decade, recently being the subject of the 2023 chemistry Nobel prize.[218] They are nanoparticles smaller than the Bohr radius of the respective material, typically in the range of 1-10 nm. This causes quantum confinement of electrons in the material, leading to a discretization and separation of the energy levels at the valence and conduction bands.[219–221] Because of this, their optoelectronic properties are dependent not only on the chemical composition of the

material, but also on size, making them compelling for optoelectronic applications.

CsPbX$_3$ materials may be fabricated in QD colloidal suspension by facile, ambient atmosphere, low-cost synthesis such as *hot injection*,[222–224] which allows to more easily optimize its material properties such as photoluminescence quantum yield (PLQY) thanks to the reduced ion migration, which in bulk films happens at the grain boundaries.[224] Owing to the relatively large Bohr diameter in CsPbX$_3$ materials of up to 5-12 nm (7 nm in CsPbBr$_3$), the bandgap of CsPbX$_3$ QDs can be tuned not only compositionally but also through QD size throughout the visible range up to 410-700 nm.[225–228]

One of the most extensively employed material families for quantum dots in commercial technology are Chalcogenides (InGaP, CdSe, etc.). They have been used commercially in display technologies for light down-conversion in QLED screens by companies such as Samsung, where rich and pure colors can be achieved thanks to their emission spectrum tunability and narrow emission full width half maximum (FWHM), covering in excess of 110% of the NTSC standard, surpassing OLED technology.[229] In comparison, electroluminescent quantum dot-based LEDs (including perovskite materials) reach up to 140 %, and traditional. Inorganic metal halide perovskite materials promise better performance with decreased cost and without the highly hazardous material Cd.

CsPbX$_3$ QDs show a combination of high PLQY (up to >90%) and narrow emission FWHM down to 12 nm-42 nm (for blue and red, respectively),[230,231] a combination that had only been achieved in core-shell chalcogenide QDs such as CdSe ones[230] which require hazardous and expensive chemical materials, and complex synthesis and structure.[231] In comparison, CsPbX$_3$ QDs are cadmium-free. While lead is a toxic heavy metal, Pb is considered less hazardous than Cd, and thus regulations in the EU allow concentrations of up to 1000 ppm of Pb in electronics, compared to the 100 ppm allowed for Cd.[222] Furthermore, knowledge and conclusions learnt from CsPbX$_3$-based LEDs may potentially be extrapolated to other families of lead-free perovskites which, while still limited in stability and luminous efficiency, are being actively researched.[232–239]

A distinctive property of lead halide perovskite QDs, lacking in other materials such as CdSe,[222] is their widely known defect tolerance,[240] which facilitates the synthesis

process to obtain high emission perovskite QD solutions. This is generally understood to arise from their tendency to form shallow trap states near the CBM and VBM as a result of the formation energies of shallow defect states being lower than that of deeper states.[241,242]

2.3. Inkjet-printed devices

In the following subsections, the three device families fabricated through inkjet printing throughout this thesis will be introduced: memristors, photodetectors and LEDs.

2.3.1. Memristors

Memristors may change their electrical resistance between different states in a reversible way in response to electrical stimulus, a mechanism known as *resistive switching* (RS). This property may be exploited to store information, as the different resistance states can be set to code information in the form of bits digitally, or in an analog form.

While first reports of I(V) hysteresis effects in certain materials were made in the 60s,[243] it wouldn't be until 1971 when Leon Chua suggested by a symmetry argument in his foundational paper[244] that alongside the resistor, the capacitor, and the inductor, there should exist a fourth passive circuit element. He termed this element the memristor (*mem*ory re*sistor*) and argued that the I(V) hysteresis effects observed by other researchers were a manifestation of this effect.

Resistive switching is observed in a variety of materials and structures. Since the switching mechanism can be very localized, direct observation of the phenomenon is notoriously challenging. Nonetheless, some researchers have demonstrated structural and compositional proof (through electron energy loss spectroscopy) of resistive switching mechanisms by in-situ transmission electron microscopy (Fig. 2.11).[245]
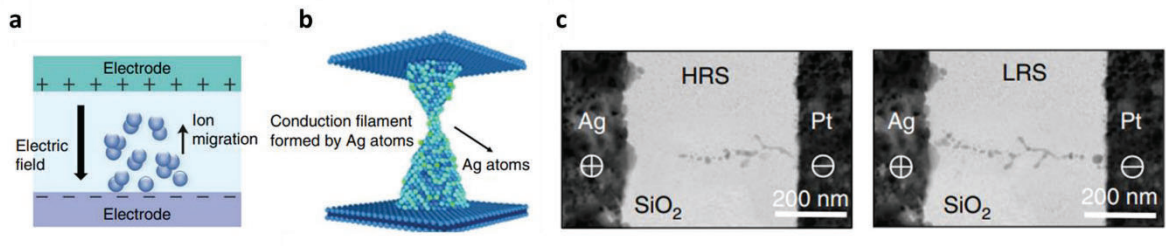
Fig. 2.11 a) movement of ions in a memristor under an applied voltage b) conductive filament connecting the two electrodes c) in-situ TEM visualization of filamentary resistive switching in an Ag based memristor. Reprinted from Ref [245] (a), Ref [246] (b), and Ref [247] (c).

This switching phenomenon is generally understood to be related to the formation and destruction of preferential conduction paths within the device. The formation of these preferential conduction paths in the SET process is believed to result from an electromigration of certain chemical species caused by the electric potential difference between the contacts of the device.[248–250] By applying an electrical stress to the device, these species are released and become mobile, drifting as an electric potential is applied. With enough stress, these species accumulate towards the positive contact side of the device, leaving behind a nanoscopic conductive filament (Fig. 2.12).
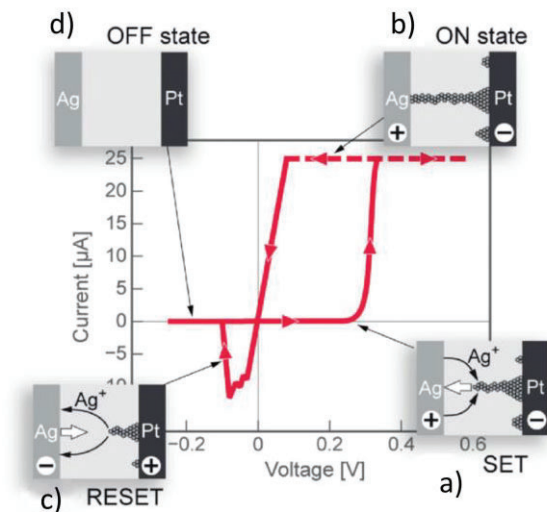
Fig. 2.12 Movement of mobile ionic species in the SET and RESET processes in a bipolar memristor. Reprinted from Ref [251].

Resistive switching can be classified according to different parameters. It may manifest as either switching between discrete resistance states (abrupt switching), or as a continuous variation in resistance (analog switching). The switching effect can also be

temporal, with a return or decay to a certain state (volatile switching), or it can be effectively permanent (non-volatile switching). Furthermore, resistive switching devices may be operated by a sudden electrical pulse, or a voltage ramp, and in terms of polarity they may operate in bipolar or unipolar modes. A short summary of these typologies is shown in Table 2.2 Visual Summary of RS typologies..

Table 2.2 Visual Summary of RS typologies.

Discretization of States	Volatility of states	Switching polarity	Current compliance	Applied switching stimulus
Abrupt switching: Discrete states	Non-volatile: Permanent	Bipolar: diferent polarities are required fow SET and RESET	Self-compliance: no current compliance is needed	Pulsed operation: The voltage is applied in a fast pulse, typically 1ns-1ms
or	or	or	or	or
Analog switching: Continuous variation	Volatile: The resistive states decay	Unipolar: SET and RESET are performed on the same polarity	Current compliance required	Voltage ramp: A steadily increasing voltage sweep is performed

These are not necessarily mutually exclusive categories: an RS device may operate in a number of these modes depending on the stimulus it receives. For example, a device may be able to operate in both pulsed and voltage ramp mode, or perhaps might behave as either bipolar or unipolar conditioned by a number of factors (e.g. depending on the current limitation imposed on the source measurement unit).

2.3.1.1 Filament formation by abrupt switching through ramped voltage

Ramped voltage operation is one of the standard modes of operation of memristors, where a voltage across the device is swept from 0-V_1. A current limitation (Icc) of is usually imposed in order to avoid an irreversible change of the device. As the voltage is increased in the positive direction, the current in the device increases gradually until it suddenly jumps up to Icc (rightmost, green curve in Fig. 2.13 a and b). When this happens, the device has switched from a low resistance state (LRS) to a high resistance state (HRS) (i.e., it has been *set*) for the first time, and thus it is said to have been *formed*. This is a requisite first step for operation of most memristors.

In the case of a bipolar switching device, the HRS is returned to (i.e., *reset*) by a similar process in the opposite polarity where the voltage is swept in the negative range until the device switches to a HRS (Fig. 2.13 b) red curve in the third quadrant). From

this point, the device can be cycled from HRS to LRS and vice-versa by repeating these processes. On the other hand, in the case of unipolar devices, the reset process is performed in the same polarity as the set process (Fig. 2.13 a, red curve labelled reset). This unipolar reset process generally requires a higher I_{cc} to occur, which is thought to be necessary in order to elicit a joule heating-mediated dissolution of the filament.
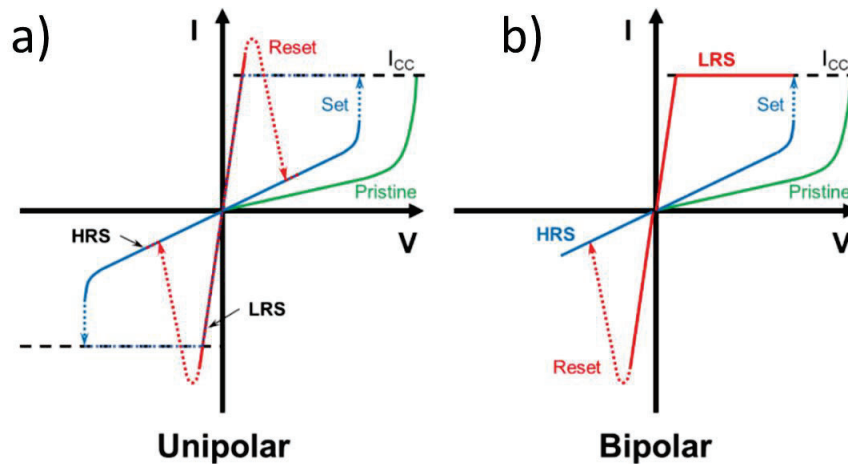
Fig. 2.13 Schematic representation of unipolar and bipolar abrupt switching.

2.3.1.2 Dynamics of the set process in filamentary memristors

The mobile chemical species involved in the RS mechanism can belong to different families, according to the device structure. In metal oxide memristors, one of the most commonly studied materials for RS, switching is determined by electromigration of oxygen vacancies ($V_{o^{2+}}$) which have a positive effective electrical charge, a mechanism typically known as *valence change mechanism* (VCM). By applying an electrical stress to the device, oxygen ions are released and accumulate in the positive contact side of the device, leaving behind a path of defective oxide material. As the material becomes defective, it turns more conductive at a local level, thus forming a nanometric conductive path.

Another extensively studied family of memristive architectures is known by the name *electrochemical migration* (ECM), consisting of devices that rely on the movement of small radius metallic cations (*e.g.*, Cu+, Ag^+) within an insulating matrix. Here, the conductive filament is formed as these metallic cations assemble into electrically conductive nanofilaments. These cations can either be supplied from metallic contacts

40

that act as reservoirs, or from metallic nanoparticles embedded in the metal oxide. ECM devices, in contrast to most of the filamentary VCM type, may display volatile switching.

2.3.1.3 Dynamics of the reset process

The reset process results from the destruction of the conductive filaments, leading to a return to a HRS. A distinction should be made between unipolar and bipolar memristors, due to the difference in the reset mechanism evidenced by their different modes of operation.

In bipolar devices, the reset process is a reversal of the set process, with ionic species flowing in the opposite direction due to the opposite voltage polarity, leading to a destruction of the conductive filaments. In addition, localized Joule heating around the filaments due to the high current density is thought to play a role in the dissolution of the conductive filament.[252] In contrast, for unipolar switching devices, Joule heating is believed to be the main mechanism mediating the destruction of the filaments. Although this simple explanation of the reset process is satisfactory for a first approach to the resistive switching phenomenon, more accurate models for the reset process take into account the complex interplay between phenomena such as the Soret force, resulting from a temperature differential in the population of mobile ions close and far from the conductive filaments, and the Fick force, an opposite force arising from the differential in concentration of mobile ions close and far from the conductive filaments.[243]

After the first forming cycle, the HRS of a bipolar memristor is generally more conductive than the pristine state. This is believed to be caused by a partial reset process where a remnant of the conductive paths is left (Fig. 2.14).[253]
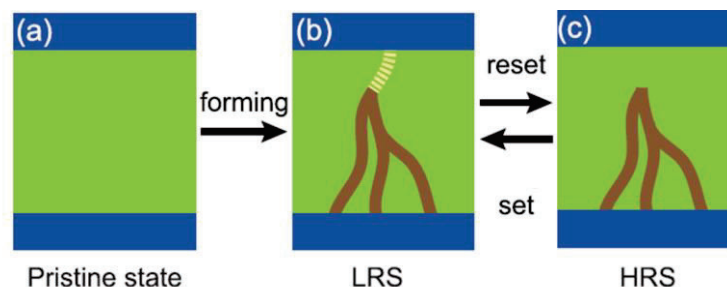
Fig. 2.14 Irreversible filament formation after the initial electroforming process. Reprinted from Ref [243].

2.3.1.4 Applications of resistive switching

The possible applications of resistive switching devices depend on their specific behavior, as shown in Fig. 2.15, which showcases some of the most commonly studied architectures. Abrupt switching mechanisms are generally favored for use as digital memories. Here the main concern is good separation between logical states, which is achieved when the HRS and LRS are very different, ideally by several orders of magnitude.

On the other hand, RS devices that show analog switching characteristics are favored towards use in analog computation applications. Analog memristors have been proposed as a hardware accelerator for vector-matrix product operations. This may be accomplished by a crossbar array of memristors, each storing a matrix value as a resistance state, whereas the vector is represented by the input currents. Multiplications of the dot product are carried out through Ohm's law, as a product of currents and resistances.[254,255]

a Memory applications **b** Neuromorphic applications **c** Security applications
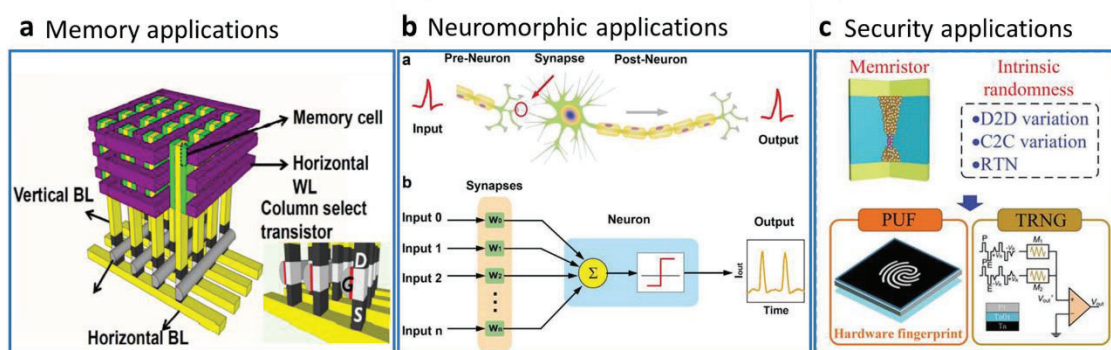
Fig. 2.15 Some popular applications for memristors: (a) high density application for solid state data storage, (b) neuromorphic computation applications that emulate the behavior of neurons, and (c) security applications that exploit the stochasticity of memristors. Reprinted from Ref [256] (a), Ref [257] (b) and Ref [258] (c)

More exotic applications involve the emulation of certain aspects of signal processing in biological neurons, a field known as neuromorphic computing. For example, it is well known that an important process that originates learning in the brain is spike-timing dependent plasticity, where two neurons that activate close in time together will strengthen their synaptic connection strength (Hebbian learning rules).[259] Clever setups have been used to induce spike-timing dependent plasticity and other neuron-like behaviors in memristors.

One of the challenges in memristors is in cycle-to-cycle and device-to-device repeatability. The switching threshold of resistive switching devices usually displays some variability, sometimes in a range of a few volts. This operating uncertainty limits practical applicability of memristors, especially in digital memory applications, where it would become a reliability issue. However, this intrinsic stochastic nature of memristors may be exploited for certain applications where unpredictability is sought for. An example of this will be explored in ***Chapter 4***, where inkjet-printed h-BN memristors are used as true random number generators (TRNG) for security applications.

2.3.2. Photodiodes

Photodetectors are an essential component for applications where electronics needs to interact with light. Fields such as scientific instrumentation, imaging and communications all have specific requirements for photodetection. For instance, photomultiplier tubes are very bulky and fragile, but are essential for precise scientific measurements, being capable of measuring single photons. On the other end of the spectrum, charged coupled devices have much lower sensitivity, but can be miniaturized in high densities, forming the basic sensing elements in cameras, where high spatial resolution is paramount. One property missing in these types of photodetectors, however, is wavelength discrimination, which is imperative for applications such as UV flame sensing and UV radiation dosimetry.

In light of this, photodiodes are a family of devices can be fabricated to intrinsically discriminate UV from visible radiation by appropriate choice of material, at low fabrication cost and complexity, compact form factor, ideal for wearable and flexible applications.

2.3.3. Standard operation of photodetectors based on PN junction diodes

Photodiodes are essentially p-n or p-i-n junctions that can be exposed to light. In dark condition, they behave as a typical diode with a rectifying I-V characteristic, changing their behavior when exposed to light. Following is a concise view of the basic working of these devices.

2.3.3.1 Photodiode at no applied external voltage and dark condition

In dark condition, a photodiode operates as a standard p-n junction. At the p-type and n-type material junction, diffusion causes majority carriers from either material to migrate into the opposite zone due to the differential in charge carrier concentration: holes form the p-type material diffuse into the n-type material, and electrons from the n-type material migrate into the p-type side (Fig. 2.16). As this happens, charge carriers recombine and a region with low carrier concentration is formed, called the depletion region or space charge region. This refers to the fact that, as a result of the intense recombination in this region, ionized acceptor (in the p-type side) and donor species (in the n-type side) form a built-in potential.
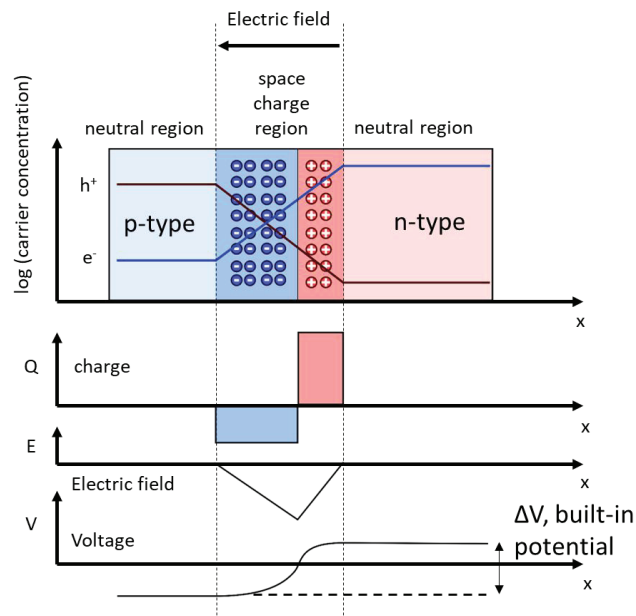
Fig. 2.16 Sketch of p-n junction at equilibrium with no applied voltage in dark condition

The effect of this built-in potential on charge carriers in the device is twofold. First, since the built-in potential increases the electric potential at the n-type region relative to the p-region, it creates a barrier for majority carriers from the respective p- and n-type regions, slowing down diffusion. This applies to either type of carrier, as holes (h^+) have higher potential energy for increasing positive potential fields, and vice-versa for electrons (e^-). This explanation can be reversed for the minority carriers of either material. Minority carriers, which are mostly thermally generated, are instead driven in the opposite direction when they form in the space charge region. Thus, the built-in potential also

creates a drift current of minority carriers that in these conditions is equal and opposite to the diffusion current of majority carriers.

2.3.3.2 Photodiode at a positive or negative applied external voltage and dark condition

Once a positive voltage is applied to the p-type side of the device, the potential barrier is diminished, and the diffusion current of majority carriers is facilitated. This creates a current that increases with increased applied voltage.

In the case of negative polarization, the potential barrier is instead increased, further impeding the diffusion of majority carriers, which tends to zero with increasing negative polarization. On the other hand, the flow of minority carriers remains mostly constant. This is because the minority carrier current depends mostly on the rate of generation of minority carriers within a close distance to the depletion region about their respective diffusion length, which is determined primarily by temperature. For this reason, a negative current with little dependence on voltage appears in the negative polarization. This current under negative bias is also called *dark current* and is an important parameter in photodetectors as it establishes the baseline for measurement.

2.3.3.3 Photodiode under illuminated condition

Upon illumination with photons of sufficient energy, electron-hole pairs are generated in the photodiode. When an electron-hole pair is generated within the depletion region, or a diffusion length away from it, its built-in potential can separate either charge carrier into their respective majority region (Fig. 2.17 a). If the photodiode is in a closed circuit, an overall device current can be established, known as *photocurrent* (I_p in Fig. 2.17 b). This current depends on the intensity of the incident light and is one of the main modes of operation of photodetection.
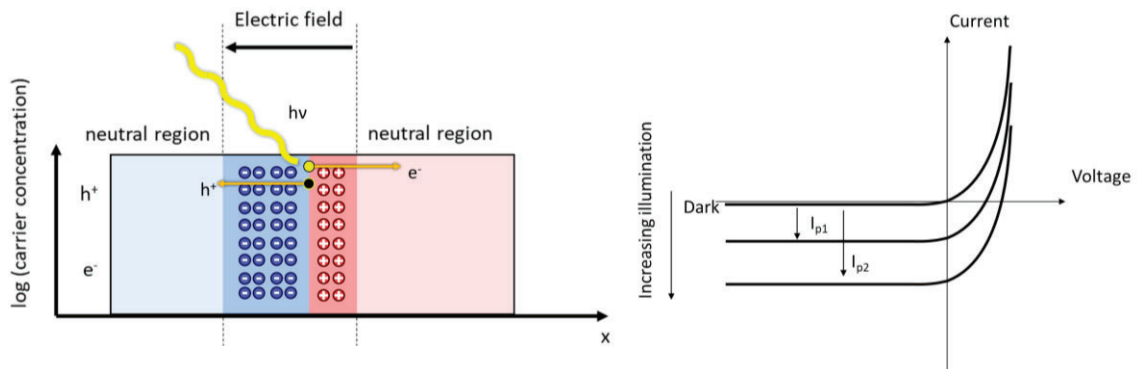
Fig. 2.17 (a) electron-hole pair separation in a photodiode (b) I(V) characteristic under dark and illuminated conditions.

In order to facilitate detection through photocurrent, photodetectors are normally operated at negative bias, due to the increased contrast between the dark current and the photocurrent. In addition, negative bias also increases the length of the depletion region slightly, increasing the probability that a photon will generate an electron-hole pair there.

2.3.4. LEDs

LEDs convert electrical energy directly into light energy through *electroluminescence* (EL), and therefore can achieve higher power conversion efficiencies than other technologies. Since the first demonstrations on SiC in 1907, the materials and structures have evolved in a variety of directions. Early applications of LEDs mostly involved simple indicator lights and electroluminescent 7-segment displays. Today, and thanks to advancements such as the successful development of the blue LED in the late 90's which allowed having emitters for the RGB components of light, LEDs occupy crucial roles in all aspects of life in displays, room lighting, vehicle headlights, etc.

In order to specialize to the requirements of each of the varied applications of LEDs, there exist multiple LED structures and materials, including bulk II-VI and III-V semiconductors, OLEDs, and quantum dots/nanocrystals. Depending on the application, some properties are given preference; for example, research of LEDs for display applications is concerned with providing narrow FWHM emission spectra, as that improves the perceived color saturation and richness of the display.[260] Indeed, the possibility of LEDs to provide extremely narrow emission spectra (<20 nm) for display

applications has been one of the drivers of LED technology, with OLED and QLED displays thriving thanks to their unparalleled color accuracy.

Emission by EL can be mediated by a number of mechanisms of which exciton recombination is the most common type. Here, a hole and an electron meet within an emissive layer, with the energy being released in the form of light. In this type of LED, one of the most crucial elements is arguably the emissive layer, as that determines the properties of the light emitted, and places constraints on the rest of the device fabrication process. Important emitter materials include group III/V semiconductors such as GaAs, GaN and related compounds for blue LEDs and organic emitters such as Alq_3 (Tris(8-hydroxyquinoline)aluminum) in OLED.

While the most basic device structure of exciton recombination LEDs can be realized in a p-n homojunction, a p-i-n heterojunction can offer improved emission efficiency due to the confinement of charge carriers around the emissive intrinsic layer (Fig. 2.18). In a p-i-n LED structure, electrons and holes are injected from opposite contacts in the device and directed towards an active emissive layer. If the device structure is adequate, they will recombine in the active layer, releasing energy which will be converted into photons corresponding to the bandgap energy. The wavelength of the light emitted will depend on the energy transitions in the active layer, being ideally equal to the bandgap energy. Thus, by selection of the active layer, the light emitted can be tuned.
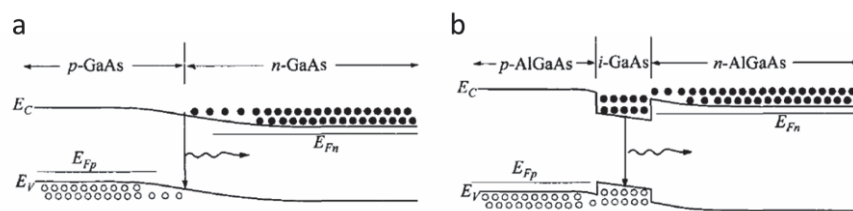
Fig. 2.18 Examples of p-n homojunction (a) and pin heterojunction (b), showing the confinement of charge carriers in the p-i-n structure, which leads to increased emission efficiency. Reprinted from *Ref*[261].

In this thesis, the metal halide perovskite $CsPbBr_3$ in the form of nanocrystals is demonstrated and studied as an electroluminescent emitter in thin film LEDs. Thanks to the compatibility of materials, fabrication processes, and convenient energy band alignment, the field of perovskite LEDs has borrowed substantially from the field of OLEDs, benefitting from its mature materials and fabrication processes. This translates

into the use of materials, structures, and terminology from the OLED field. While organic materials are known to offer excellent performance, their lifetime and chemical stability is known to be limited.

2.3.4.1 Light sources in current display technologies

Display technologies have come a long way since the now outdated bulky cathode ray tube sets, improving in size, color quality, consumption, and cost. Current display technologies may be divided into two main families according to how they generate and display images. Some displays generate light through a backlight setup, that is later filtered through filters and polarizers at the different RGB sub-pixels (backlight-based displays), as opposed to directly generating light at the subpixels (EL-based displays). In the following section, we will see how perovskites may be employed in either family to obtain high-quality color reproduction.

► Current backlight-based displays

This family of displays is characterized by a method of illumination based on a backlight model. In these displays, a white backlight is shone uniformly behind the screen. When a color is to be represented, an array of RGB-filtering subpixels is engaged, blocking a portion of the respective RGB components of the incoming white light, thus generating the desired color. This is generally achieved by a combination of polarizing layers and the use of electrically activated liquid crystals. Backlight-based displays have an inherent energy efficiency limitation, as light that is not needed is discarded.

First models employed a cold cathode fluorescent lamp (CCFL) backlight to provide white illumination. While this method provides an appropriate backlight spectrum, CCFLs are relatively energy inefficient and need supply voltages up to 1000V,[262] thus requiring inverter transformers that are expensive and bulky. CCFL sources can be swapped by white LEDs (WLED).[263] These provide a similar white backlight at a reduced cost and complexity, as LEDs require much simpler power delivery compared to CCFLs. However, the color reproduction of these screens is still limited due to limitations of the color filters. These color filters have a limited capacity to filter a narrow spectrum of light, which, coupled with the wide spectrum white light, leads to RGB components with wide spectra (Fig. 2.19 a).

The color purity of LCD display technology may be improved by narrowing the emission spectrum of the backlight itself. By using a backlight composed of an array of red, green and blue LEDs, that backlight spectrum becomes more specific to the RGB components, and the crosstalk between components can be greatly reduced, increasing color quality. This concept can be further improved by narrowing the RGB emission spectra, such as by using QD fluorescent emitters to down-convert blue light from an emitting panel into red and green, commercially known as QLED (Fig. 2.19a). Thanks to the narrow and symmetrical emission spectrum FWHM of QD emitters (≈30 nm for commercial chalcogenide QDs, ≈20 nm for metal halide perovskites),[264] the color reproduction of these QLEDs displays can surpass that of OLED, as organic emitters display comparatively broader (>40 nm)[264], more asymmetrical spectra.[265] Perovskite quantum dots may be used for color conversion[211] instead of CdSe quantum dots at improved emission FWHM and reduced toxicity and a reduced cost thanks to the availability of materials and facile fabrication routes.
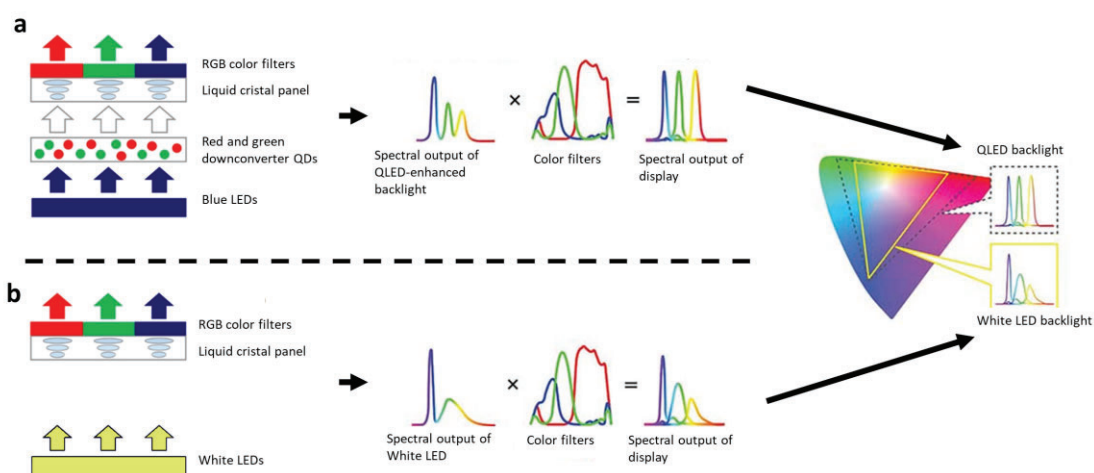
Fig. 2.19 Comparison of QLED (a) and standard white LED LCD display technologies (b), showing increased color purity with QD-enhanced backlight displays. Adapted from Refs[266,267].

► Current electroluminescence-based displays

In terms of commercial display applications, OLED is the most relevant EL technology due to its high color reproduction quality. OLEDs are LEDs that are composed of organic material thin films. OLEDs can emit narrow-band single colors, can be

fabricated in a patterned way on top of a substrate and have fast response times. This enables OLEDs to be used as light sources in displays. They may also be fabricated to emit white light for lighting applications.[62]

OLED displays have become commonplace in smartphones, where their color accuracy and wide viewing angles give them an edge over LCD displays. They can also be fabricated on flexible substrates, being able to withstand bending, twisting, and stretching. This enables OLEDs to be used in wearable displays and other applications where it is required to conform to a non-planar surface. Besides display applications, OLEDs have been used in room illumination, where they offer particularly comfortable light.

The current main challenges of OLED technology involve the chemical stability of the materials used and quality of the material interfaces. Different interactions can degrade device performance and lifetime, including degradation by exposure to moisture and oxygen, photooxidation, corrosion of the substrate, electrical migration of ions, and thermal degradation.[268] Obtaining good organic-inorganic interfaces can be difficult, and, over time, metallic ion migration into the organic layer can induce further degradation. In addition, the fabrication cost of OLEDs is significant, as the organic materials required tend to be expensive.

Perovskite materials can be used as an active layer in a structure similar to that of OLED devices. Thanks to their narrow emission FWHM EL, they have received interest as pure color light sources. This application will be the focus of this chapter and will be explored in the next section.

2.3.4.2 Perovskite LEDs (PeLEDs)

PeLEDs share a few similarities with OLEDs, both in terms of structure, general working principle, and in some of the challenges involved in application. In general, PeLEDs have similar challenges compared to OLEDs, as perovskite materials tend to be sensitive to moisture and oxygen. Nonetheless, PeLEDs have a potential advantage in cost, as perovskites can be manufactured at a considerably lower cost than organic emitters. The cost can be brought down further by employing inorganic charge transport and blocking layers.

In PeLEDs, the active layer is a perovskite material, which is sandwiched between charge transport and blocking layers that may be either organic or inorganic. Like OLEDs, perovskite LEDs can emit very pure colors with narrow emission spectra.

►   Structure and Band matching in Perovskite NC LEDs

The basic architecture of a PeLED consists of an emissive layer sandwiched between p-type and n-type Hole/Electron Transport Layers. Either transport layer injects the respective type of charge carrier, recombining at the emissive layer and producing light. This can be configured in n-i-p or p-i-n configurations, commonly known as "conventional" and "inverted" structures.[269] The radiative recombination of electron-hole pairs in the perovskite layer is, however, not intrinsically guaranteed, so the device structure must be engineered to promote radiative recombination in the emissive layer and improve device efficiency.[270]

An important parameter in the study of LEDs is the *external quantum efficiency* (EQE), a measure of emitted photons out of a device structure per amount of injected charge carriers. EQE loss in lead halide perovskites is generally caused by two non-radiative recombination processes: trap mediated recombination, which can be addressed by improving layer quality and passivating defect traps, and Auger recombination (Fig. 2.20), wherein the energy from electron and hole recombination is transferred to a third charge carrier non-radiatively, which eventually releases the energy through thermalization, causing Joule heating and stressing the device.[270–274] Compared to other materials, Auger non-radiative recombination is considerably strong in perovskites.[275] Whereas the trap-assisted recombination occurs at both high and low current injection, Auger non-radiative recombination processes take importance at high driving currents, manifesting as an efficiency roll-off at high operating currents.[270,276] Additionally, perovskite QDs suffer permanent degradation due to the exposure to high current densities and temperatures due to Joule heating (up to ≳10-1000 A cm^{-2} in some reported structures).[276,277]
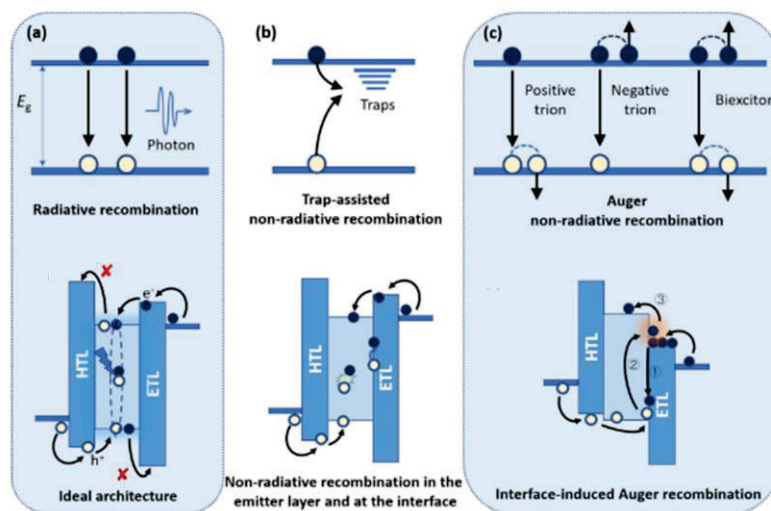
Fig. 2.20 Radiative and nonradiative recombination routes in LEDs: (a) Radiative recombination thanks to balanced charge injection and low trap density, (b) non-radiative recombination due to defective materials and interfaced, (c) Auger nonradiative recombination due to accumulation of charge carriers. Reproduced from Ref [270].

The efficiency of a perovskite LED can be improved by addressing the following: ensuring balanced charge injection and no parasitic currents (e.g. due to pinholes), improving the intrinsic emission efficiency of the perovskite (measured by the quantity *electroluminescence quantum yield,* ELQY), and improving the light outcoupling.[269] ELQY is generally assumed to correspond to the intrinsic PLQY of the material,[269] whereas light outcoupling can be improved by strategies including the adaption of the refractive indices of the material[278] and the use of textured layers.[279]h Thanks to the tendency of MHP to form shallow traps due to surface defects, these can easily be passivated by modifying the surface of the perovskite QDs.[270] Following, the improvement of EQE through charge injection balance and device structure optimization will be addressed.

Due to the long diffusion length of excitons in metal halide perovskites (up to 100-1000 nm),[280,281] in an unoptimized device structure charge carriers may be able to traverse the perovskite film and reach the charge transport layer of the opposite polarity,[280,281] recombining there. This recombination at the charge transport layer may either be non-radiative, reducing EQE, or radiative at an unwanted emission wavelength. In either case, this unwanted recombination is to be avoided, which can be achieved by adding Charge Blocking Layers (CBLs), materials with a deeper conduction band minimum (CBM) or

valence band maximum (VBM) level (*highest occupied molecular orbital* - HOMO or *lowest unoccupied molecular orbital* – LUMO, respectively, in the case of organic materials) that confine holes and electrons within the emissive layer. This blocking ability increases the probability of a hole and electron to meet in the active layer and recombine radiatively, increasing the efficiency of the LED.

However, even if charges are effectively confined at the perovskite layer, non-radiative recombination may still occur due to improper charge injection balance into the perovskite layer. Ideally, the same number of electrons and holes should be injected into the active layer to radiatively recombine there. If charge injection into the perovskite layer is not balanced, excess carriers may accumulate in either the perovskite/ETL or HTL/perovskite interfaces.[272,282,283] In Fig. 2.21 a, hole injection from the HTL into the perovskite is lower than electron injection the ETL, leading to an accumulation of electrons in the perovskite layer. In addition to the decrease in EQE due to the excess charge carriers that are lost,[276] this can lead to increased Auger nonradiative recombination, again translating into low EQE and reduced device stability.
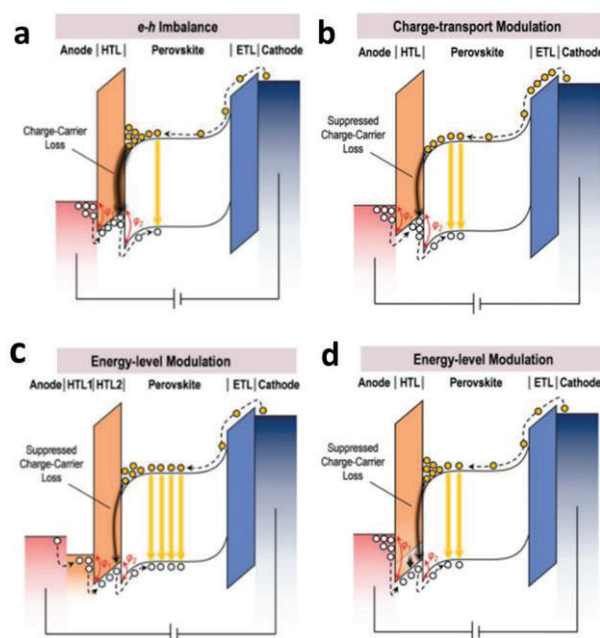
Fig. 2.21 Addressing inefficiencies in PeLED device structures containing blocking layers. (a) Effect of charge injection imbalance (b) charge injection balancing by interface engineering and modification of charge transport properties (ETL here), (c) by reducing band mismatch with an interfacial layer and (d) by intentional creation of a high injection barrier (HTL here) to equate hole and electron injection. Reproduced from Ref [269].

Such charge injection imbalance may be caused by several reasons. One source of imbalanced charge injection is due to asymmetrical charge transport properties for the ETL and HTL (not pictured). Charge injection balance can be improved by tuning the charge injection properties of either the HTL or ETL in order to increase the injection of deficit carriers or reduce that of excess carriers. This may be achieved by doping the charge transport layers or to some extent by tuning the charge transport layer thickness, as seen in Fig. 2.21 b. In doing so, the respective charge carriers can be injected equally, reducing charge accumulation.[269]

Charge injection imbalance may also be caused not by the transport properties of the materials, but by an energy band mismatch in interfaces Fig. 2.21 a. When a considerable mismatch between layers exists, an undesirable high barrier of injection is created, leading to accumulation of charge carriers at the interface and slowing down of injection. As before, the result is that the opposite charge carriers are injected in excess, accumulating at the perovskite interface with the HTL. In addition, here the non-radiative auger recombination effects at the interface may be exacerbated by the accumulation of both types of charge carriers at either side.[270]

In the case of mismatched energy levels, imbalanced charge injection may be addressed by increasing or decreasing the respective charge carrier injection of the HTL/ETL to eliminate excess charge carriers in the perovskite layer Fig. 2.21 c. Yet, another effective solution to mismatched energy levels consists of inserting an additional layer with an intermediate energy, reducing the high injection barrier, as can be seen in Fig. 2.21 c. As a result, carrier accumulation is reduced, and injection is improved. This is typically the case for PEDOT:PSS, a common reference HTL which has a relatively shallow VBM, so device efficiency tends to benefit from the addition of an interlayer.

Intentional charge blocking at strategically chosen interfaces can also be used to reduce excess charge carrier flow, as in Fig. 2.21 d. Some groups have proposed using an HTL/ETL with a deeper VBM/CBM to regulate the injection of charge carriers into the perovskite.[281] While this does not completely remove the accumulation of holes, instead promoting it in a different interface, the negative effects of Auger recombination on the perovskite/CTL layer on EQE are less marked than those of accumulation at the

HTL/perovskite interface.

During the PeLED fabrication throughout this thesis, several charge blocking layers were implemented in **_Chapter 6_**. The electron blocking ability of an inorganic NiO interlayer was demonstrated in two device architectures comparing a PEDOT:PSS/CsPBBr3/PO-T2T/LiF/Al and PEDOT:PSS/NiO/CsPbBr3/PO-T2T/LiF/Al. In addition, the n-type materials PO-T2T and inkjet-printed inorganic SnO_2 function as hole blocking layers due to their deep LUMO/CBM levels.

REFERENCES

1. Chang, J., Zhang, X., Ge, T. & Zhou, J. Fully printed electronics on flexible substrates: High gain amplifiers and DAC. *Org Electron* **15**, 701–710 (2014).

2. Yeo, J. *et al.* Next Generation Non-Vacuum, Maskless, Low Temperature Nanoparticle Ink Laser Digital Direct Metal Patterning for a Large Area Flexible Electronics. *PLoS One* **7**, e42315 (2012).

3. Hösel, M. *et al.* High-Volume Processed, ITO-Free Superstrates and Substrates for Roll-to-Roll Development of Organic Electronics. *Advanced Science* **1**, 1400002 (2014).

4. Suganuma, K. *Introduction to Printed Electronics*. vol. 74 (Springer New York, 2014).

5. Sekine, C., Tsubata, Y., Yamada, T., Kitano, M. & Doi, S. Recent progress of high performance polymer OLED and OPV materials for organic printed electronics. *Sci Technol Adv Mater* **15**, 034203 (2014).

6. *Applications of Organic and Printed Electronics*. (Springer US, 2013). doi:10.1007/978-1-4614-3160-2.

7. Hast, J. *et al.* 18.1: Invited Paper : Roll-to-Roll Manufacturing of Printed OLEDs. *SID Symposium Digest of Technical Papers* **44**, 192–195 (2013).

8. Ling, H., Liu, S., Zheng, Z. & Yan, F. Organic Flexible Electronics. *Small Methods* **2**, 1800070 (2018).

9. Khan, Y. *et al.* A New Frontier of Printed Electronics: Flexible Hybrid Electronics. *Advanced Materials* **32**, (2020).

10. Hennig, G. Lasersonic® LIFT Process for Large Area Digital Printing. *Journal of Laser Micro/Nanoengineering* **7**, 299–305 (2012).

11. Sopeña, P., Sieiro, J., Fernández-Pradas, J. M., López-Villegas, J. M. & Serra, P. Laser-Induced Forward Transfer: A Digital Approach for Printing Devices on Regular Paper. *Adv Mater Technol* **5**, (2020).

12. Makrygianni, M. *et al.* Eco-Friendly Lead-Free Solder Paste Printing via Laser-Induced Forward Transfer for the Assembly of Ultra-Fine Pitch Electronic Components. *Materials* **14**, 3353 (2021).

13. Shan, Y., Zhang, X., Li, H. & Zhan, Z. Single-step printing of high-resolution, high-aspect ratio silver lines through laser-induced forward transfer. *Opt Laser Technol* **133**, 106514 (2021).

14. Tobjörk, D. & Österbacka, R. Paper Electronics. *Advanced Materials* **23**, 1935–1961 (2011).

15. Abbel, R. *et al.* Industrial-scale inkjet printed electronics manufacturing—production up-scaling from concept tools to a roll-to-roll pilot line. *Translational Materials Research* **1**,

015002 (2014).

16. *OLED Fundamentals*. (CRC Press, 2015). doi:10.1201/b18485.

17. Travis, T. A history of screen printing: how an art evolved into an industry. Guido Lengwiler. Cincinnati, OH: ST Media Group International, 2013. 484 p. ill. ISBN 9780944094747 $75.00 (hardcover). *Art Libraries Journal* **41**, 65–67 (2016).

18. Hobby, A. Fundamentals of Screens for Electronics Screen Printing. *Circuit World* **16**, 16–28 (1990).

19. Zhou, L. *et al.* Screen-Printed Poly(3,4-Ethylenedioxythiophene):Poly(Styrenesulfonate) Grids as ITO-Free Anodes for Flexible Organic Light-Emitting Diodes. *Adv Funct Mater* **28**, 1705955 (2018).

20. Zhao, C. *et al.* Fully Screen-Printed, Multicolor, and Stretchable Electroluminescent Displays for Epidermal Electronics. *ACS Appl Mater Interfaces* **12**, 47902–47910 (2020).

21. Birnstock, J. *et al.* Screen-printed passive matrix displays based on light-emitting polymers. *Appl Phys Lett* **78**, 3905–3907 (2001).

22. Birnstock, J. *et al.* Screen-printed passive matrix displays and multicolor devices. in (ed. Kafafi, Z. H.) 68 (2002). doi:10.1117/12.457461.

23. Chen, C. *et al.* Perovskite solar cells based on screen-printed thin films. *Nature* **612**, 266–271 (2022).

24. Hennig, G., Selbmann, K.-H., Pfinninger, S., Brendel, J. & Brüning, S. Large scale laser microstructuring of gravure print rollers. in (eds. Holmes, A. S. et al.) 68790O (2008). doi:10.1117/12.774967.

25. Hennig, G., Selbmann, K.-H. & Brockelt, A. Laser engraving in gravure industry. in (eds. Gries, W. & Pearsall, T. P.) 61570C (2005). doi:10.1117/12.660938.

26. Grau, G. *et al.* Gravure-printed electronics: recent progress in tooling development, understanding of printing physics, and realization of printed devices. *Flexible and Printed Electronics* **1**, 023002 (2016).

27. Tobjörk, D. & Österbacka, R. Paper Electronics. *Advanced Materials* **23**, 1935–1961 (2011).

28. Rathschlag, T. Colorants in printing applications. *Physical Sciences Reviews* **7**, 163–195 (2022).

29. Saive, R. *et al.* Effectively Transparent Front Contacts for Optoelectronic Devices. *Adv Opt Mater* **4**, 1470–1474 (2016).

30. Kim, Y. Y. *et al.* Gravure-Printed Flexible Perovskite Solar Cells: Toward Roll-to-Roll Manufacturing. *Advanced Science* **6**, 1802094 (2019).

31. Merklein, L. *et al.* Comparative Study of Printed Multilayer OLED Fabrication through

Slot Die Coating, Gravure and Inkjet Printing, and Their Combination. *Colloids and Interfaces* **3**, 32 (2019).

32. Zhu, H. *et al.* A gravure printed antenna on shape-stable transparent nanopaper. *Nanoscale* **6**, 9110 (2014).

33. de la Fuente Vornbrock, A., Sung, D., Kang, H., Kitsomboonloha, R. & Subramanian, V. Fully gravure and ink-jet printed high speed pBTTT organic thin film transistors. *Org Electron* **11**, 2037–2044 (2010).

34. Kim, C. H., Jo, J. & Lee, S.-H. Design of roll-to-roll printing equipment with multiple printing methods for multi-layer printing. *Review of Scientific Instruments* **83**, (2012).

35. Schmidt, G. *et al.* Challenges and perspectives of printed electronics. in (eds. Bao, Z. & Gundlach, D. J.) 633610 (2006). doi:10.1117/12.680256.

36. Guo, Z. *et al.* Application Research of Nano Silver Conductive Ink in Flexographic Printed RFID Antenna. in 480–487 (2019). doi:10.1007/978-981-13-3663-8_65.

37. Wang, Y. *et al.* A facile process combined with roll-to-roll flexographic printing and electroless deposition to fabricate RFID tag antenna on paper substrates. *Compos B Eng* **224**, 109194 (2021).

38. Furukawa, T., Kawamura, N., Inoue, J., Nakada, H. & Koden, M. P-57: OLED Lighting Devices Fabricated by Flexography Printing of Silver Nanowire and Conducting Polymer. *SID Symposium Digest of Technical Papers* **46**, 1355–1358 (2015).

39. Raupp, S. *et al.* Slot Die Coated and Flexo Printed Highly Efficient SMOLEDs. *Adv Mater Technol* **2**, 1600230 (2017).

40. Sopeña, P., González-Torres, S., Fernández-Pradas, J. M. & Serra, P. Spraying dynamics in continuous wave laser printing of conductive inks. *Sci Rep* **8**, 7999 (2018).

41. Piqué, A. & Serra, P. *Laser Printing of Functional Materials*. (Wiley, 2018). doi:10.1002/9783527805105.

42. Sopeña, P., Fernández-Pradas, J. M. & Serra, P. Laser-induced forward transfer of conductive screen-printing inks. *Appl Surf Sci* **507**, 145047 (2020).

43. Sopeña, P., Serra, P. & Fernández-Pradas, J. M. Transparent and conductive silver nanowires networks printed by laser-induced forward transfer. *Appl Surf Sci* **476**, 828–833 (2019).

44. Li, J., Rossignol, F. & Macdonald, J. Inkjet printing for biosensor fabrication: combining chemistry and technology for advanced manufacturing. *Lab Chip* **15**, 2538–2558 (2015).

45. Wijshoff, H. The dynamics of the piezo inkjet printhead operation☆. *Phys Rep* **491**, 77–177 (2010).

46. Derby, B. Inkjet Printing of Functional and Structural Materials: Fluid Property Requirements, Feature Stability, and Resolution. *Annu Rev Mater Res* **40**, 395–414

(2010).

47.   Derby, B. Inkjet Printing of Functional and Structural Materials: Fluid Property Requirements, Feature Stability, and Resolution. *Annu Rev Mater Res* **40**, 395–414 (2010).

48.   Fromm, J. E. Numerical Calculation of the Fluid Dynamics of Drop-on-Demand Jets. *IBM J Res Dev* **28**, 322–333 (1984).

49.   Reis, N. & Derby, B. Ink Jet Deposition of Ceramic Suspensions: Modeling and Experiments of Droplet Formation. *MRS Proceedings* **625**, 117 (2000).

50.   Jang, D., Kim, D. & Moon, J. Influence of Fluid Physical Properties on Ink-Jet Printability. *Langmuir* **25**, 2629–2635 (2009).

51.   Duineveld, P. C. *et al.* Ink-jet printing of polymer light-emitting devices. in (ed. Kafafi, Z. H.) 59 (2002). doi:10.1117/12.457460.

52.   An experimental investigation of fluid flow resulting from the impact of a water drop with an unyielding dry surface. *Proceedings of the Royal Society of London. A. Mathematical and Physical Sciences* **373**, 419–441 (1981).

53.   Bhola, R. & Chandra, S. Parameters controlling solidification of molten wax droplets falling on a solid surface. *J Mater Sci* **34**, 4883–4894 (1999).

54.   Werner Zapka - Handbook of Industrial Inkjet Printing_ A Full System Approach-Wiley-VCH (2017).pdf.

55.   Soltman, D. & Subramanian, V. Inkjet-Printed Line Morphologies and Temperature Control of the Coffee Ring Effect. *Langmuir* **24**, 2224–2231 (2008).

56.   Fukai, J. *et al.* Effects of droplet size and solute concentration on drying process of polymer solution droplets deposited on homogeneous surfaces. *International Journal of Heat and Mass Transfer* vol. 49 3561–3567 Preprint at https://doi.org/10.1016/j.ijheatmasstransfer.2006.02.049 (2006).

57.   Grant, T. D. *et al.* Inkjet printing of high-concentration particle-free platinum inks. *Mater Des* **214**, 110377 (2022).

58.   Aydemir, C., Altay, B. N. & Akyol, M. Surface analysis of polymer films for wettability and ink adhesion. *Color Res Appl* **46**, 489–499 (2021).

59.   Mackley, M. R., Vadillo, D. C. & Tuladhar, T. R. Inkjet Fluid Characterization. in *Fundamentals of Inkjet Printing* 339–364 (Wiley-VCH Verlag GmbH & Co. KGaA, 2015). doi:10.1002/9783527684724.ch13.

60.   Soltman, D. & Subramanian, V. Inkjet-Printed Line Morphologies and Temperature Control of the Coffee Ring Effect. *Langmuir* **24**, 2224–2231 (2008).

61.   Hu, H. & Larson, R. G. Marangoni Effect Reverses Coffee-Ring Depositions. *J Phys Chem B* **110**, 7090–7094 (2006).

62. Gaspar, D. J. & Polikarpov, E. *OLED fundamentals: Materials, devices, and processing of organic light-emitting diodes. OLED Fundamentals: Materials, Devices, and Processing of Organic Light-Emitting Diodes* (2015). doi:10.1201/b18485.

63. Aziz, H. & Popovic, Z. D. Degradation Phenomena in Small-Molecule Organic Light-Emitting Devices. *Chemistry of Materials* **16**, 4522–4532 (2004).

64. Baldacchini, G., Baldacchini, T., Pace, A. & Pode, R. B. Emission Intensity and Degradation Processes of Alq[sub 3] Films. *Electrochemical and Solid-State Letters* **8**, J24 (2005).

65. McAleer, J. F., Moseley, P. T., Norris, J. O. W. & Williams, D. E. Tin dioxide gas sensors. Part 1.—Aspects of the surface chemistry revealed by electrical conductance variations. *Journal of the Chemical Society, Faraday Transactions 1: Physical Chemistry in Condensed Phases* **83**, 1323 (1987).

66. Jing, X., Puglisi, F., Akinwande, D. & Lanza, M. Chemical vapor deposition of hexagonal boron nitride on metal-coated wafers and transfer-free fabrication of resistive switching devices. *2d Mater* **6**, 035021 (2019).

67. Kiaee, Z. *et al.* Inkjet- and flextrail-printing of silicon polymer-based inks for local passivating contacts. in 110002 (2022). doi:10.1063/5.0089256.

68. Cherian, D., Mitra, K. Y., Hartwig, M., Malinowski, P. E. & Baumann, R. R. Fabrication of Organic Photo Detectors Using Inkjet Technology and Its Comparison to Conventional Deposition Processes. *IEEE Sens J* **18**, 94–105 (2018).

69. Fang, X. *et al.* Patterning Liquid Crystalline Organic Semiconductors via Inkjet Printing for High-Performance Transistor Arrays and Circuits. *Adv Funct Mater* **31**, (2021).

70. Sui, Y. & Zorman, C. A. Review—Inkjet Printing of Metal Structures for Electrochemical Sensor Applications. *J Electrochem Soc* **167**, 037571 (2020).

71. Zikulnig, J. *et al.* Printed Electronics Technologies for Additive Manufacturing of Hybrid Electronic Sensor Systems. *Advanced Sensor Research* **2**, (2023).

72. Yin, J. *et al.* Boron Nitride Nanostructures: Fabrication, Functionalization and Applications. *Small* **12**, 2942–2968 (2016).

73. Lin, Y. & Connell, J. W. Advances in 2D boron nitride nanostructures: nanosheets, nanoribbons, nanomeshes, and hybrids with graphene. *Nanoscale* **4**, 6908 (2012).

74. Moon, S. *et al.* Hexagonal Boron Nitride for Next-Generation Photonics and Electronics. *Advanced Materials* **35**, (2023).

75. Dean, C. R. *et al.* Boron nitride substrates for high-quality graphene electronics. *Nat Nanotechnol* **5**, 722–726 (2010).

76. Chowdhury, C., Karmakar, S. & Datta, A. Capping Black Phosphorene by h-BN Enhances Performances in Anodes for Li and Na Ion Batteries. *ACS Energy Lett* **1**, 253–

259 (2016).

77. Lo, C.-L. *et al.* Studies of two-dimensional h-BN and MoS2 for potential diffusion barrier application in copper interconnect technology. *NPJ 2D Mater Appl* **1**, 42 (2017).

78. Kim, K. K. *et al.* Synthesis and Characterization of Hexagonal Boron Nitride Film as a Dielectric Layer for Graphene Devices. *ACS Nano* **6**, 8583–8590 (2012).

79. Cheng, S., Zhou, Y., Hu, J., He, J. & Li, Q. Polyimide films coated by magnetron sputtered boron nitride for high-temperature capacitor dielectrics. *IEEE Transactions on Dielectrics and Electrical Insulation* **27**, 498–503 (2020).

80. Li, H., Ren, L., Zhou, Y., Yao, B. & Wang, Q. Recent progress in polymer dielectrics containing boron nitride nanosheets for high energy density capacitors. *High Voltage* **5**, 365–376 (2020).

81. Constantinescu, G. C. & Hine, N. D. M. Multipurpose Black-Phosphorus/hBN Heterostructures. *Nano Lett* **16**, 2586–2594 (2016).

82. Caldwell, J. D. *et al.* Photonics with hexagonal boron nitride. *Nat Rev Mater* **4**, 552–567 (2019).

83. Chen, T.-A. *et al.* Wafer-scale single-crystal hexagonal boron nitride monolayers on Cu (111). *Nature* **579**, 219–223 (2020).

84. Weng, M. H. *et al.* Recent advance in high manufacturing readiness level and high temperature CMOS mixed-signal integrated circuits on silicon carbide. *Semicond Sci Technol* **32**, 054003 (2017).

85. Sedky, S., Witvrouw, A., Bender, H. & Baert, K. Experimental determination of the maximum post-process annealing temperature for standard CMOS wafers. *IEEE Trans Electron Devices* **48**, 377–385 (2001).

86. Sedky, S. Electrical Properties and Noise of Poly SiGe Deposited at Temperatures Compatible With MEMS Integration on Top of Standard CMOS. *MRS Proceedings* **729**, U3.2 (2002).

87. Shen, Y. *et al.* Variability and Yield in h-BN-Based Memristive Circuits: The Role of Each Type of Defect. *Advanced Materials* **33**, (2021).

88. Xie, J., Afshari, S. & Sanchez Esqueda, I. Hexagonal boron nitride (h-BN) memristor arrays for analog-based machine learning hardware. *NPJ 2D Mater Appl* **6**, 50 (2022).

89. Shi, Y. *et al.* Electronic synapses made of layered two-dimensional materials. *Nat Electron* **1**, 458–465 (2018).

90. Pan, C. *et al.* Model for multi-filamentary conduction in graphene/hexagonal-boron-nitride/graphene based resistive switching devices. *2d Mater* **4**, 025099 (2017).

91. Pan, C. *et al.* Coexistence of Grain-Boundaries-Assisted Bipolar and Threshold Resistive Switching in Multilayer Hexagonal Boron Nitride. *Adv Funct Mater* **27**, (2017).

92.   Yuan, B. *et al.* 150 nm × 200 nm Cross-Point Hexagonal Boron Nitride-Based Memristors. *Adv Electron Mater* **6**, (2020).

93.   Wen, C. *et al.* Advanced Data Encryption using 2D Materials. *Advanced Materials* **33**, (2021).

94.   Kamiya, T. & Hosono, H. Material characteristics and applications of transparent amorphous oxide semiconductors. *NPG Asia Mater* **2**, 15–22 (2010).

95.   Nomura, K. *et al.* Amorphous oxide semiconductors for high-performance flexible thin-film transistors. *Japanese Journal of Applied Physics, Part 1: Regular Papers and Short Notes and Review Papers* **45**, 4303–4308 (2006).

96.   Yu, X., Marks, T. J. & Facchetti, A. Metal oxides for optoelectronic applications. *Nat Mater* **15**, 383–396 (2016).

97.   You, J. *et al.* Improved air stability of perovskite solar cells via solution-processed metal oxide transport layers. *Nat Nanotechnol* **11**, 75–81 (2016).

98.   Jiang, Q., Zhang, X. & You, J. SnO 2 : A Wonderful Electron Transport Layer for Perovskite Solar Cells. *Small* **14**, 1801154 (2018).

99.   Nomura, K. *et al.* Room-temperature fabrication of transparent flexible thin-film transistors using amorphous oxide semiconductors. *Nature* **432**, 488–492 (2004).

100.   Park, J. S., Maeng, W. J., Kim, H. S. & Park, J. S. Review of recent developments in amorphous oxide semiconductor thin-film transistor devices. *Thin Solid Films* **520**, 1679–1693 (2012).

101.   Berry, J. J. *et al.* Surface Treatment of NiO Hole Transport Layers for Organic Solar Cells. *IEEE Journal of Selected Topics in Quantum Electronics* **16**, 1649–1655 (2010).

102.   Steirer, K. X. *et al.* Solution deposited NiO thin-films as hole transport layers in organic photovoltaics. *Org Electron* **11**, 1414–1418 (2010).

103.   Yu, X., Marks, T. J. & Facchetti, A. Metal oxides for optoelectronic applications. *Nat Mater* **15**, 383–396 (2016).

104.   Chung, S., Cho, K. & Lee, T. Recent Progress in Inkjet-Printed Thin-Film Transistors. *Advanced Science* **6**, 1801445 (2019).

105.   Garlapati, S. K. *et al.* Printed Electronics Based on Inorganic Semiconductors: From Processes and Materials to Devices. *Advanced Materials* **30**, 1707600 (2018).

106.   Das, S. & Jayaraman, V. SnO2: A comprehensive review on structures and gas sensors. *Prog Mater Sci* **66**, 112–255 (2014).

107.   Gong, Y. *et al.* Recent advances and comprehensive insights on nickel oxide in emerging optoelectronic devices. *Sustain Energy Fuels* **4**, 4415–4458 (2020).

108.   Vasanthi, V., Sivanantham, N., Saathvika, L. & Gopalakrishnan, N. Metal oxide charge

transport materials for light emitting diodes - An overview. *Mater Sci Semicond Process* **165**, 107679 (2023).

109. Lewicka, Z. A., Yu, W. W., Oliva, B. L., Contreras, E. Q. & Colvin, V. L. Photochemical behavior of nanoscale TiO2 and ZnO sunscreen ingredients. *J Photochem Photobiol A Chem* **263**, 24–33 (2013).

110. Sirelkhatim, A. *et al.* Review on Zinc Oxide Nanoparticles: Antibacterial Activity and Toxicity Mechanism. *Nanomicro Lett* **7**, 219–242 (2015).

111. Li, C., Li, Y., Wu, Y., Ong, B.-S. & Loutfy, R.-O. Fabrication conditions for solution-processed high-mobility ZnO thin-film transistors. *J Mater Chem* **19**, 1626 (2009).

112. Liu, C., Xiao, C. & Li, W. Zinc oxide nanoparticles as electron transporting interlayer in organic solar cells. *J Mater Chem C Mater* **9**, 14093–14114 (2021).

113. Cao, S. *et al.* Enhancing the Performance of Quantum Dot Light-Emitting Diodes Using Room-Temperature-Processed Ga-Doped ZnO Nanoparticles as the Electron Transport Layer. *ACS Appl Mater Interfaces* **9**, 15605–15614 (2017).

114. Maouche, D., Saoud, F. S. & Louail, L. Dependence of structural properties of ZnO on high pressure. *Mater Chem Phys* **106**, 11–15 (2007).

115. Kim, D.-H., Lee, G.-W. & Kim, Y.-C. Interaction of zinc interstitial with oxygen vacancy in zinc oxide: An origin of n-type doping. *Solid State Commun* **152**, 1711–1714 (2012).

116. Kim, Y.-S. & Park, C. H. Rich Variety of Defects in ZnO via an Attractive Interaction between O Vacancies and Zn Interstitials: Origin of n-Type Doping. *Phys Rev Lett* **102**, 086403 (2009).

117. Xie, X., Li, B., Zhang, Z. & Shen, D. Reinventing a p-type doping process for stable ZnO light emitting devices. *J Phys D Appl Phys* **51**, 225104 (2018).

118. Özgür, Ü. *et al.* A comprehensive review of ZnO materials and devices. *J Appl Phys* **98**, 1–103 (2005).

119. Hwang, D.-K. *et al.* p -ZnO/n-GaN heterostructure ZnO light-emitting diodes. *Appl Phys Lett* **86**, (2005).

120. Nanishi, Y. The birth of the blue LED. *Nat Photonics* **8**, 884–886 (2014).

121. Frieiro, J. L. L. *et al.* Toward RGB LEDs based on rare earth-doped ZnO. *Nanotechnology* **31**, 465207 (2020).

122. Ryu, Y. R. *et al.* ZnO devices: Photodiodes and p-type field-effect transistors. *Appl Phys Lett* **87**, (2005).

123. Yan, M.-M. *et al.* Enhancing the Performance of Blue Quantum-Dot Light-Emitting Diodes Based on Mg-Doped ZnO as an Electron Transport Layer. *IEEE Photonics J* **9**, 1–8 (2017).

124. Jiang, C. *et al.* Coffee-Ring-Free Quantum Dot Thin Film Using Inkjet Printing from a Mixed-Solvent System on Modified ZnO Transport Layer for Light-Emitting Devices. *ACS Appl Mater Interfaces* **8**, 26162–26168 (2016).

125. Tang, C. *et al.* Optimizing the Performance of Perovskite Nanocrystal LEDs Utilizing Cobalt Doping on a ZnO Electron Transport Layer. *J Phys Chem Lett* **12**, 10112–10119 (2021).

126. Kirkwood, N., Singh, B. & Mulvaney, P. Enhancing Quantum Dot LED Efficiency by Tuning Electron Mobility in the ZnO Electron Transport Layer. *Adv Mater Interfaces* **3**, 1600868 (2016).

127. Vasanthi, V., Sivanantham, N., Saathvika, L. & Gopalakrishnan, N. Metal oxide charge transport materials for light emitting diodes - An overview. *Mater Sci Semicond Process* **165**, 107679 (2023).

128. Chen, M. *et al.* Highly Stable SnO 2 -Based Quantum-Dot Light-Emitting Diodes with the Conventional Device Structure. *ACS Nano* **16**, 9631–9639 (2022).

129. Zeng, J. *et al.* ZnO-Based Electron-Transporting Layers for Perovskite Light-Emitting Diodes: Controlling the Interfacial Reactions. *J Phys Chem Lett* **13**, 694–703 (2022).

130. Gunnarsson, W. B., Xu, Z., Noel, N. K. & Rand, B. P. Improved Charge Balance in Green Perovskite Light-Emitting Diodes with Atomic-Layer-Deposited Al 2 O 3. *ACS Appl Mater Interfaces* **14**, 34247–34252 (2022).

131. Pang, Z. *et al.* Hydrophobic PbS QDs layer decorated ZnO electron transport layer to boost photovoltaic performance of perovskite solar cells. *Chemical Engineering Journal* **439**, 135701 (2022).

132. Sun, Y. *et al.* Efficient quantum dot light-emitting diodes with a Zn 0.85 Mg 0.15 O interfacial modification layer. *Nanoscale* **9**, 8962–8969 (2017).

133. Heo, S. B. *et al.* Highly efficient and low turn-on voltage quantum-dot light-emitting diodes using a ZnMgO/ZnO double electron transport layer. *Current Applied Physics* **29**, 107–113 (2021).

134. Wang, Y., Zhang, H. & Ji, W. Efficient Quantum-Dot Light-Emitting Diodes Based on Solvent-Annealed SnO 2 Electron-Transport Layers. *ACS Appl Electron Mater* **5**, 537–543 (2023).

135. Wang, H. *et al.* Efficient perovskite light-emitting diodes based on a solution-processed tin dioxide electron transport layer. *J Mater Chem C Mater* **6**, 6996–7002 (2018).

136. Tran, V.-H., Eom, S. H., Yoon, S. C., Kim, S.-K. & Lee, S.-H. Enhancing device performance of inverted organic solar cells with SnO2/Cs2CO3 as dual electron transport layers. *Org Electron* **68**, 85–95 (2019).

137. Haque, M. A., Sheikh, A. D., Guan, X. & Wu, T. Metal Oxides as Efficient Charge Transporters in Perovskite Solar Cells. *Adv Energy Mater* **7**, 1–23 (2017).

138. Zhang, Z. *et al.* Morphology-controlled synthesis and a comparative study of the physical properties of SnO 2 nanostructures: from ultrathin nanowires to ultrawide nanobelts. *Nanotechnology* **20**, 135605 (2009).

139. Das, S. & Jayaraman, V. SnO2: A comprehensive review on structures and gas sensors. *Prog Mater Sci* **66**, 112–255 (2014).

140. Wang, H. *et al.* Efficient perovskite light-emitting diodes based on a solution-processed tin dioxide electron transport layer. *J Mater Chem C Mater* **6**, 6996–7002 (2018).

141. Huang, H. *et al.* Semiconductor gas sensor based on tin oxide nanorods prepared by plasma-enhanced chemical vapor deposition with postplasma treatment. *Appl Phys Lett* **87**, 163123 (2005).

142. Coles, G. S. V, Williams, G. & Smith, B. The effect of oxygen partial pressure on the response of tin (IV) oxide based gas sensors. *J Phys D Appl Phys* **24**, 633–641 (1991).

143. Khanna, A., Kumar, R. & Bhatti, S. S. CuO-doped SnO2 thin films as hydrogen sulfide gas sensor. *Appl Phys Lett* **82**, 4388–4390 (2003).

144. Comini, E., Faglia, G., Sberveglieri, G., Pan, Z. & Wang, Z. L. Stable and highly sensitive gas sensors based on semiconducting oxide nanobelts. *Appl Phys Lett* **81**, 1869–1871 (2002).

145. Correa Baena, J. P. *et al.* Highly efficient planar perovskite solar cells through band alignment engineering. *Energy Environ Sci* **8**, 2928–2934 (2015).

146. Ke, W. *et al.* Low-Temperature Solution-Processed Tin Oxide as an Alternative Electron Transporting Layer for Efficient Perovskite Solar Cells. *J Am Chem Soc* **137**, 6730–6733 (2015).

147. Park, M. *et al.* Colloidal quantum dot light-emitting diodes employing solution-processable tin dioxide nanoparticles in an electron transport layer. *RSC Adv* **10**, 8261–8265 (2020).

148. Wang, Y. *et al.* Electron transport mechanism in colloidal SnO 2 nanoparticle films and its implications for quantum-dot light-emitting diodes. *J Phys D Appl Phys* **55**, 374004 (2022).

149. Wang, H. *et al.* Efficient perovskite light-emitting diodes based on a solution-processed tin dioxide electron transport layer. *J Mater Chem C Mater* **6**, 6996–7002 (2018).

150. Tran, V.-H., Park, H., Eom, S. H., Yoon, S. C. & Lee, S.-H. Modified SnO 2 with Alkali Carbonates as Robust Electron-Transport Layers for Inverted Organic Solar Cells. *ACS Omega* **3**, 18398–18410 (2018).

151. Lee, S. *et al.* Control of Interface Defects for Efficient and Stable Quasi-2D Perovskite Light-Emitting Diodes Using Nickel Oxide Hole Injection Layer. *Advanced Science* **5**, 1801350 (2018).

152. Wang, H. *et al.* Boosting the Efficiency of NiO x -Based Perovskite Light-Emitting Diodes by Interface Engineering. *ACS Appl Mater Interfaces* **12**, 53528–53536 (2020).

153. Zhuang, S., Ma, X., Hu, D., Dong, X. & Zhang, B. Air-stable all inorganic green perovskite light emitting diodes based on ZnO/CsPbBr3/NiO heterojunction structure. *Ceram Int* **44**, 4685–4688 (2018).

154. Luo, D. *et al.* Device Engineering for All-Inorganic Perovskite Light-Emitting Diodes. *Nanomaterials* **9**, 1007 (2019).

155. Zheng, W. *et al.* High-efficiency perovskite nanocrystal light-emitting diodes via decorating NiO x on the nanocrystal surface. *Nanoscale* **12**, 8711–8719 (2020).

156. Zhuang, S. *et al.* Fabrication and optimization of hole transport layer NiO for all inorganic perovskite light emitting diodes. *Mater Sci Semicond Process* **109**, 104924 (2020).

157. Yu, J., Rosso, K. M. & Bruemmer, S. M. Charge and Ion Transport in NiO and Aspects of Ni Oxidation from First Principles. *The Journal of Physical Chemistry C* **116**, 1948–1954 (2012).

158. Jang, W.-L., Lu, Y.-M., Hwang, W.-S., Hsiung, T.-L. & Wang, H. P. Point defects in sputtered NiO films. *Appl Phys Lett* **94**, (2009).

159. Jeng, J.-Y. *et al.* Nickel Oxide Electrode Interlayer in CH 3 NH 3 PbI 3 Perovskite/PCBM Planar-Heterojunction Hybrid Solar Cells. *Advanced Materials* **26**, 4107–4113 (2014).

160. Zhang, Y., Zhao, L., Jia, H. & Li, P. Study of the electroluminescence performance of NiO-based quantum dot light-emitting diodes: The effect of annealing atmosphere. *Appl Surf Sci* **526**, 146732 (2020).

161. Nguyen, H. T., Jeong, H., Park, J.-Y., Ahn, Y. H. & Lee, S. Charge Transport in Light Emitting Devices Based on Colloidal Quantum Dots and a Solution-Processed Nickel Oxide Layer. *ACS Appl Mater Interfaces* **6**, 7286–7291 (2014).

162. Chan, I.-M., Hsu, T.-Y. & Hong, F. C. Enhanced hole injections in organic light-emitting devices by depositing nickel oxide on indium tin oxide anode. *Appl Phys Lett* **81**, 1899–1901 (2002).

163. Hsu, C.-M., Wu, W.-T. & Lee, H.-H. Turn-on voltage reduction of organic light-emitting diode using a nickel-doped indium tin oxide anode prepared by single target sputtering. *Displays* **29**, 268–272 (2008).

164. Im, H. C. *et al.* Highly efficient organic light-emitting diodes fabricated utilizing nickel-oxide buffer layers between the anodes and the hole transport layers. *Thin Solid Films* **515**, 5099–5102 (2007).

165. Tan, S. *et al.* Stability-limiting heterointerfaces of perovskite photovoltaics. *Nature* **605**, 268–273 (2022).

166. Berggren, M., Nilsson, D. & Robinson, N. D. Organic materials for printed electronics.

Nat Mater **6**, 3–5 (2007).

167. Chu, Y., Qian, C., Chahal, P. & Cao, C. Printed Diodes: Materials Processing, Fabrication, and Applications. *Advanced Science* **6**, 1801653 (2019).

168. Kraft, T. M., Berger, P. R. & Lupo, D. Printed and organic diodes: devices, circuits and applications. *Flexible and Printed Electronics* **2**, 033001 (2017).

169. *Physics of Organic Semiconductors*. (Wiley, 2005). doi:10.1002/3527606637.

170. Hong, G. *et al.* A Brief History of OLEDs—Emitter Development and Industry Milestones. *Advanced Materials* **33**, 2005630 (2021).

171. Sun, Y. *et al.* Solution-processed small-molecule solar cells with 6.7% efficiency. *Nat Mater* **11**, 44–48 (2012).

172. Kraft, T. M., Berger, P. R. & Lupo, D. Printed and organic diodes: devices, circuits and applications. *Flexible and Printed Electronics* **2**, 033001 (2017).

173. Sirringhaus, H. Device Physics of Solution-Processed Organic Field-Effect Transistors. *Advanced Materials* **17**, 2411–2425 (2005).

174. Chu, Y., Qian, C., Chahal, P. & Cao, C. Printed Diodes: Materials Processing, Fabrication, and Applications. *Advanced Science* **6**, 1801653 (2019).

175. Coropceanu, V. *et al.* Charge Transport in Organic Semiconductors. *Chem Rev* **107**, 926–952 (2007).

176. Coehoorn, R., Pasveer, W. F., Bobbert, P. A. & Michels, M. A. J. Charge-carrier concentration dependence of the hopping mobility in organic materials with Gaussian disorder. *Phys Rev B* **72**, 155206 (2005).

177. Xia, Y. & Dai, S. Review on applications of PEDOTs and PEDOT:PSS in perovskite solar cells. *Journal of Materials Science: Materials in Electronics* **32**, 12746–12757 (2021).

178. Sun, Z. *et al.* Performance-Enhancing Approaches for PEDOT:PSS-Si Hybrid Solar Cells. *Angewandte Chemie International Edition* **60**, 5036–5055 (2021).

179. Xia, Y., Sun, K. & Ouyang, J. Solution-Processed Metallic Conducting Polymer Films as Transparent Electrode of Optoelectronic Devices. *Advanced Materials* **24**, 2436–2440 (2012).

180. Kim, N. *et al.* Highly Conductive PEDOT:PSS Nanofibrils Induced by Solution-Processed Crystallization. *Advanced Materials* **26**, 2268–2272 (2014).

181. Allard, S., Forster, M., Souharce, B., Thiem, H. & Scherf, U. Organic Semiconductors for Solution-Processable Field-Effect Transistors (OFETs). *Angewandte Chemie International Edition* **47**, 4070–4098 (2008).

182. Kim, N. *et al.* Highly Conductive All-Plastic Electrodes Fabricated Using a Novel

Chemically Controlled Transfer-Printing Method. *Advanced Materials* **27**, 2317–2323 (2015).

183. Yu, J. C. *et al.* Highly Efficient Polymer-Based Optoelectronic Devices Using PEDOT:PSS and a GO Composite Layer as a Hole Transport Layer. *ACS Appl Mater Interfaces* **6**, 2067–2073 (2014).

184. Han, W. *et al.* Recent Progress of Inverted Perovskite Solar Cells with a Modified PEDOT:PSS Hole Transport Layer. *ACS Appl Mater Interfaces* **12**, 49297–49322 (2020).

185. Eom, S. H. *et al.* Polymer solar cells based on inkjet-printed PEDOT:PSS layer. *Org Electron* **10**, 536–542 (2009).

186. Lo, L.-W. *et al.* An Inkjet-Printed PEDOT:PSS-Based Stretchable Conductor for Wearable Health Monitoring Device Applications. *ACS Appl Mater Interfaces* **13**, 21693–21702 (2021).

187. Bihar, E. *et al.* Inkjet-Printed PEDOT:PSS Electrodes on Paper for Electrocardiography. *Adv Healthc Mater* **6**, 1601167 (2017).

188. Srichan, C. *et al.* Inkjet printing PEDOT:PSS using desktop inkjet printer. in *2009 6th International Conference on Electrical Engineering/Electronics, Computer, Telecommunications and Information Technology* 465–468 (IEEE, 2009). doi:10.1109/ECTICON.2009.5137049.

189. Bhalla, A. S., Guo, R. & Roy, R. The perovskite structure—a review of its role in ceramic science and technology. *Materials Research Innovations* **4**, 3–26 (2000).

190. Cohen, R. E. Origin of ferroelectricity in perovskite oxides. *Nature* **358**, 136–138 (1992).

191. Peña, M. A. & Fierro, J. L. G. Chemical Structures and Performance of Perovskite Oxides. *Chem Rev* **101**, 1981–2018 (2001).

192. Chung, I., Lee, B., He, J., Chang, R. P. H. & Kanatzidis, M. G. All-solid-state dye-sensitized solar cells with high efficiency. *Nature* **485**, 486–489 (2012).

193. Salim, T. *et al.* Perovskite-based solar cells: impact of morphology and device architecture on device performance. *J Mater Chem A Mater* **3**, 8943–8969 (2015).

194. Gao, P., Grätzel, M. & Nazeeruddin, M. K. Organohalide lead perovskites for photovoltaic applications. *Energy Environ. Sci.* **7**, 2448–2463 (2014).

195. Bretschneider, S. A., Weickert, J., Dorman, J. A. & Schmidt-Mende, L. Research Update: Physical and electrical characteristics of lead halide perovskites for solar cell applications. *APL Mater* **2**, (2014).

196. Kojima, A., Teshima, K., Shirai, Y. & Miyasaka, T. Organometal Halide Perovskites as Visible-Light Sensitizers for Photovoltaic Cells. *J Am Chem Soc* **131**, 6050–6051 (2009).

197. Park, N.-G. Perovskite solar cells: an emerging photovoltaic technology. *Materials Today* **18**, 65–72 (2015).

198. Green, M. A., Ho-Baillie, A. & Snaith, H. J. The emergence of perovskite solar cells. *Nat Photonics* **8**, 506–514 (2014).

199. Park, N.-G. Organometal Perovskite Light Absorbers Toward a 20% Efficiency Low-Cost Solid-State Mesoscopic Solar Cell. *J Phys Chem Lett* **4**, 2423–2429 (2013).

200. Rhee, J. H., Chung, C.-C. & Diau, E. W.-G. A perspective of mesoscopic solar cells based on metal chalcogenide quantum dots and organometal-halide perovskites. *NPG Asia Mater* **5**, e68–e68 (2013).

201. McGehee, M. D. Continuing to soar. *Nat Mater* **13**, 845–846 (2014).

202. Snaith, H. J. Perovskites: The Emergence of a New Era for Low-Cost, High-Efficiency Solar Cells. *J Phys Chem Lett* **4**, 3623–3630 (2013).

203. Snaith, H. J. Perovskites: The Emergence of a New Era for Low-Cost, High-Efficiency Solar Cells. *J Phys Chem Lett* **4**, 3623–3630 (2013).

204. Liu, M., Johnston, M. B. & Snaith, H. J. Efficient planar heterojunction perovskite solar cells by vapour deposition. *Nature* **501**, 395–398 (2013).

205. Lee, M. M., Teuscher, J., Miyasaka, T., Murakami, T. N. & Snaith, H. J. Efficient Hybrid Solar Cells Based on Meso-Superstructured Organometal Halide Perovskites. *Science (1979)* **338**, 643–647 (2012).

206. Akkerman, Q. A. & Manna, L. What Defines a Halide Perovskite? *ACS Energy Lett* **5**, 604–610 (2020).

207. Kovalenko, M. V., Protesescu, L. & Bodnarchuk, M. I. Properties and potential optoelectronic applications of lead halide perovskite nanocrystals. *Science (1979)* **358**, 745–750 (2017).

208. Liang, J. *et al.* Solution synthesis and phase control of inorganic perovskites for high-performance optoelectronic devices. *Nanoscale* **9**, 11841–11845 (2017).

209. Hu, Y. *et al.* Vacuum-evaporated all-inorganic cesium lead bromine perovskites for high-performance light-emitting diodes. *J Mater Chem C Mater* **5**, 8144–8149 (2017).

210. Kovalenko, M. V., Protesescu, L. & Bodnarchuk, M. I. Properties and potential optoelectronic applications of lead halide perovskite nanocrystals. *Science (1979)* **358**, 745–750 (2017).

211. Vescio, G. *et al.* High Quality Inkjet Printed-Emissive Nanocrystalline Perovskite CsPbBr 3 Layers for Color Conversion Layer and LEDs Applications. *Adv Mater Technol* **7**, 2101525 (2022).

212. Chondroudis, K. & Mitzi, D. B. Electroluminescence from an Organic−Inorganic Perovskite Incorporating a Quaterthiophene Dye within Lead Halide Perovskite Layers. *Chemistry of Materials* **11**, 3028–3030 (1999).

213. Era, M., Morimoto, S., Tsutsui, T. & Saito, S. Organic-inorganic heterostructure

electroluminescent device using a layered perovskite semiconductor (C6H5C2H4NH3)2PbI4. *Appl Phys Lett* **65**, 676–678 (1994).

214. Tan, Z.-K. *et al.* Bright light-emitting diodes based on organometal halide perovskite. *Nat Nanotechnol* **9**, 687–692 (2014).

215. Kim, J. S. *et al.* Ultra-bright, efficient and stable perovskite light-emitting diodes. *Nature* **611**, 688–694 (2022).

216. Green, M. A. & Ho-Baillie, A. Perovskite Solar Cells: The Birth of a New Era in Photovoltaics. *ACS Energy Lett* **2**, 822–830 (2017).

217. Isikgor, F. H. *et al.* Molecular engineering of contact interfaces for high-performance perovskite solar cells. *Nat Rev Mater* **8**, 89–108 (2022).

218. Makers of quantum dots share 2023 Nobel Prize in Chemistry. *Phys Today* **2023**, 1004a (2023).

219. Alivisatos, A. P. Perspectives on the Physical Chemistry of Semiconductor Nanocrystals. *J Phys Chem* **100**, 13226–13239 (1996).

220. Rabouw, F. T. & de Mello Donega, C. Excited-State Dynamics in Colloidal Semiconductor Nanocrystals. *Top Curr Chem* **374**, 58 (2016).

221. *Nanoparticles*. (Springer Berlin Heidelberg, 2014). doi:10.1007/978-3-662-44823-6.

222. Kovalenko, M. V., Protesescu, L. & Bodnarchuk, M. I. Properties and potential optoelectronic applications of lead halide perovskite nanocrystals. *Science (1979)* **358**, 745–750 (2017).

223. Gualdrón-Reyes, A. F., Masi, S. & Mora-Seró, I. Progress in halide-perovskite nanocrystals with near-unity photoluminescence quantum yield. *Trends Chem* **3**, 499–511 (2021).

224. Wei, Y., Cheng, Z. & Lin, J. An overview on enhancing the stability of lead halide perovskite quantum dots and their applications in phosphor-converted LEDs. *Chem Soc Rev* **48**, 310–350 (2019).

225. Protesescu, L. *et al.* Nanocrystals of Cesium Lead Halide Perovskites (CsPbX 3 , X = Cl, Br, and I): Novel Optoelectronic Materials Showing Bright Emission with Wide Color Gamut. *Nano Lett* **15**, 3692–3696 (2015).

226. Wang, L. *et al.* Blue Quantum Dot Light-Emitting Diodes with High Electroluminescent Efficiency. *ACS Appl Mater Interfaces* **9**, 38755–38760 (2017).

227. Leng, J. *et al.* Tuning the Emission Wavelength of Lead Halide Perovskite NCs via Size and Shape Control. *ACS Omega* **7**, 565–577 (2022).

228. Du, J. S. *et al.* Halide perovskite nanocrystal arrays: Multiplexed synthesis and size-dependent emission. *Sci Adv* **6**, (2020).

229. Dai, X., Deng, Y., Peng, X. & Jin, Y. Quantum-Dot Light-Emitting Diodes for Large-Area Displays: Towards the Dawn of Commercialization. *Advanced Materials* **29**, 1607022 (2017).

230. Protesescu, L. *et al.* Nanocrystals of Cesium Lead Halide Perovskites (CsPbX 3 , X = Cl, Br, and I): Novel Optoelectronic Materials Showing Bright Emission with Wide Color Gamut. *Nano Lett* **15**, 3692–3696 (2015).

231. Clasen Hames, B., Sánchez Sánchez, R., Fakharuddin, A. & Mora-Seró, I. A Comparative Study of Light-Emitting Diodes Based on All-Inorganic Perovskite Nanoparticles (CsPbBr 3) Synthesized at Room Temperature and by a Hot-Injection Method. *Chempluschem* **83**, 294–299 (2018).

232. Vescio, G. *et al.* 2D PEA 2 SnI 4 Inkjet-Printed Halide Perovskite LEDs on Rigid and Flexible Substrates. *ACS Energy Lett* **7**, 3653–3655 (2022).

233. Ma, Z. *et al.* Electrically-Driven Violet Light-Emitting Devices Based on Highly Stable Lead-Free Perovskite Cs 3 Sb 2 Br 9 Quantum Dots. *ACS Energy Lett* **5**, 385–394 (2020).

234. Li, X. *et al.* Lead-Free Halide Perovskites for Light Emission: Recent Advances and Perspectives. *Advanced Science* **8**, 2003334 (2021).

235. Yuan, F. *et al.* Color-pure red light-emitting diodes based on two-dimensional lead-free perovskites. *Sci Adv* **6**, (2020).

236. Wang, R. *et al.* Opportunities and Challenges of Lead-Free Perovskite Optoelectronic Devices. *Trends Chem* **1**, 368–379 (2019).

237. Liang, H. *et al.* High Color Purity Lead-Free Perovskite Light-Emitting Diodes via Sn Stabilization. *Advanced Science* **7**, 1903213 (2020).

238. Hong, W.-L. *et al.* Efficient Low-Temperature Solution-Processed Lead-Free Perovskite Infrared Light-Emitting Diodes. *Advanced Materials* **28**, 8029–8036 (2016).

239. Wang, J. *et al.* Two-dimensional lead-free halide perovskite materials and devices. *J Mater Chem A Mater* **7**, 23563–23576 (2019).

240. Brandt, R. E. *et al.* Searching for "Defect-Tolerant" Photovoltaic Materials: Combined Theoretical and Experimental Screening. *Chemistry of Materials* **29**, 4667–4674 (2017).

241. Yin, W.-J., Shi, T. & Yan, Y. Unusual defect physics in CH3NH3PbI3 perovskite solar cell absorber. *Appl Phys Lett* **104**, (2014).

242. Zhou, Y., Poli, I., Meggiolaro, D., De Angelis, F. & Petrozza, A. Defect activity in metal halide perovskites with wide and narrow bandgap. *Nature Reviews Materials 2021 6:11* **6**, 986–1002 (2021).

243. Lee, J. S., Lee, S. & Noh, T. W. Resistive switching phenomena: A review of statistical physics approaches. *Appl Phys Rev* **2**, (2015).

244. Chua, L. O. IEEE Transactions on Circuit Theory. *IEEE Transactions on Circuit Theory*

CT-18, 5 (1971).

245. Sun, W. *et al.* Understanding memristive switching via in situ characterization and device modeling. *Nat Commun* **10**, 3453 (2019).

246. Wang, W. *et al.* Surface diffusion-limited lifetime of silver and copper nanofilaments in resistive switching devices. *Nat Commun* **10**, 81 (2019).

247. Yang, Y. *et al.* Observation of conducting filament growth in nanoscale resistive memories. *Nat Commun* **3**, 732 (2012).

248. Lanza, M. *et al.* Standards for the Characterization of Endurance in Resistive Switching Devices. *ACS Nano* **15**, 17214–17231 (2021).

249. Wouters, D. J., Waser, R. & Wuttig, M. Phase-Change and Redox-Based Resistive Switching Memories. *Proceedings of the IEEE* **103**, 1274–1288 (2015).

250. Celano, U. *et al.* Scalability of valence change memory: From devices to tip-induced filaments. *AIP Adv* **6**, (2016).

251. Waser, R., Dittmann, R., Staikov, G. & Szot, K. Redox-Based Resistive Switching Memories – Nanoionic Mechanisms, Prospects, and Challenges. *Advanced Materials* **21**, 2632–2663 (2009).

252. Kim, S., Choi, S. & Lu, W. Comprehensive Physical Model of Dynamic Resistive Switching in an Oxide Memristor. *ACS Nano* **8**, 2369–2376 (2014).

253. Wei, T. *et al.* Three-Dimensional Reconstruction of Conductive Filaments in HfO$_x$-Based Memristor. *Advanced Materials* **35**, (2023).

254. Assaf, H., Savaria, Y. & Sawan, M. Vector Matrix Multiplication Using Crossbar Arrays: A Comparative Analysis. in *2018 25th IEEE International Conference on Electronics, Circuits and Systems (ICECS)* 609–612 (IEEE, 2018). doi:10.1109/ICECS.2018.8617942.

255. Amirsoleimani, A. *et al.* In-Memory Vector-Matrix Multiplication in Monolithic Complementary Metal–Oxide–Semiconductor-Memristor Integrated Circuits: Design Choices, Challenges, and Perspectives. *Advanced Intelligent Systems* **2**, (2020).

256. Hua, Q. *et al.* Low-Voltage Oscillatory Neurons for Memristor-Based Neuromorphic Systems. *Global Challenges* **3**, (2019).

257. Zhang, L. *et al.* Analysis of vertical cross-point resistive memory (VRRAM) for 3D RRAM design. in *2013 5th IEEE International Memory Workshop* 155–158 (IEEE, 2013). doi:10.1109/IMW.2013.6582122.

258. Pang, Y., Gao, B., Lin, B., Qian, H. & Wu, H. Memristors for Hardware Security Applications. *Adv Electron Mater* **5**, (2019).

259. Wang, S. *et al.* Memristor-Based Intelligent Human-Like Neural Computing. *Adv Electron Mater* **9**, (2023).

260. Kovalenko, M. V., Protesescu, L. & Bodnarchuk, M. I. Properties and potential optoelectronic applications of lead halide perovskite nanocrystals. *Science (1979)* **358**, 745–750 (2017).

261. Sze, S. M. & Ng, K. K. *Physics of Semiconductor Devices: Third Edition*. *Physics of Semiconductor Devices: Third Edition* (2006). doi:10.1002/9780470068328.

262. Cho, J.-H. *et al.* Digital CCFL drive system using individual current modulation for LCD-TV. in *2010 IEEE Energy Conversion Congress and Exposition* 1335–1342 (IEEE, 2010). doi:10.1109/ECCE.2010.5618278.

263. Singh, R. K. *et al.* Progress of Backlight Devices: Emergence of Halide Perovskite Quantum Dots/Nanomaterials. *Frontiers in Nanotechnology* **4**, (2022).

264. Ren, A. *et al.* Emerging light-emitting diodes for next-generation data communications. *Nat Electron* **4**, 559–572 (2021).

265. Shu, Y. *et al.* Quantum Dots for Display Applications. *Angewandte Chemie* **132**, 22496–22507 (2020).

266. Luo, Z. & Yurek, J. Quantum dots: The technology platform for all future displays. in *Light-Emitting Devices, Materials, and Applications* (eds. Strassburg, M., Kim, J. K. & Krames, M. R.) 36 (SPIE, 2019). doi:10.1117/12.2508088.

267. Sun, Y., Jiang, Y., Sun, X. W., Zhang, S. & Chen, S. Beyond OLED: Efficient Quantum Dot Light-Emitting Diodes for Display and Lighting Application. *The Chemical Record* **19**, 1729–1752 (2019).

268. Scholz, S., Kondakov, D., Lüssem, B. & Leo, K. Degradation Mechanisms and Reactions in Organic Light-Emitting Devices. *Chem Rev* **115**, 8449–8503 (2015).

269. Chen, Z., Li, Z., Hopper, T. R., Bakulin, A. A. & Yip, H.-L. Materials, photophysics and device engineering of perovskite light-emitting diodes. *Reports on Progress in Physics* **84**, 046401 (2021).

270. Cheng, H. *et al.* Understanding and minimizing non-radiative recombination losses in perovskite light-emitting diodes. *J Mater Chem C Mater* **10**, 13590–13610 (2022).

271. Park, M.-H. *et al.* Unravelling additive-based nanocrystal pinning for high efficiency organic-inorganic halide perovskite light-emitting diodes. *Nano Energy* **42**, 157–165 (2017).

272. Zhu, Z. *et al.* Spatial Control of the Hole Accumulation Zone for Hole-Dominated Perovskite Light-Emitting Diodes by Inserting a CsAc Layer. *ACS Appl Mater Interfaces* **15**, 7044–7052 (2023).

273. Jin, X. *et al.* Balancing the Electron and Hole Transfer for Efficient Quantum Dot Light-Emitting Diodes by Employing a Versatile Organic Electron-Blocking Layer. *ACS Appl Mater Interfaces* **10**, 15803–15811 (2018).

274. Yao, Z., Bi, C., Liu, A., Zhang, M. & Tian, J. High brightness and stability pure-blue perovskite light-emitting diodes based on a novel structural quantum-dot film. *Nano Energy* **95**, 106974 (2022).

275. Chen, J. & Park, N. Causes and Solutions of Recombination in Perovskite Solar Cells. *Advanced Materials* **31**, (2019).

276. Yan, F., Tan, S. T., Li, X. & Demir, H. V. Light Generation in Lead Halide Perovskite Nanocrystals: LEDs, Color Converters, Lasers, and Other Applications. *Small* **15**, (2019).

277. Kim, H. *et al.* Hybrid perovskite light emitting diodes under intense electrical excitation. *Nat Commun* **9**, 4893 (2018).

278. Saleem, M. I., Choi, R. & Lee, J.-H. Light outcoupling strategies in oriented perovskite light-emitting-diodes: recent trends, opportunities, and challenges toward innovation. *Mater Chem Front* **7**, 2316–2336 (2023).

279. Qi, H. *et al.* Synchronous Outcoupling of Tri-Colored Light for Ultra-Bright White Quantum Dot Light-Emitting Diodes by Using External Wrinkle Pattern. *Adv Opt Mater* **10**, (2022).

280. Yoon, E., Jang, K. Y., Park, J. & Lee, T. Understanding the Synergistic Effect of Device Architecture Design toward Efficient Perovskite Light-Emitting Diodes Using Interfacial Layer Engineering. *Adv Mater Interfaces* **8**, 2001712 (2021).

281. Subramanian, A. *et al.* Interfacial Energy-Level Alignment for High-Performance All-Inorganic Perovskite CsPbBr 3 Quantum Dot-Based Inverted Light-Emitting Diodes. *ACS Appl Mater Interfaces* **10**, 13236–13243 (2018).

282. Li, Z. *et al.* Modification of interface between PEDOT:PSS and perovskite film inserting an ultrathin LiF layer for enhancing efficiency of perovskite light-emitting diodes. *Org Electron* **81**, 105675 (2020).

283. Zhou, X. *et al.* Enhanced performance of inverted CsPbBr3 nanocrystal LEDs via Zn(II) doping. *Org Electron* **96**, 106253 (2021).

Chapter 3

Fabrication and characterization methods

Fully inkjet-printed device fabrication requires compliance with multiple constraints, including solvent orthogonality, wettability, and compatible thermal post-treatment conditions. While the work developed in this thesis is focused on the demonstration of inkjet printing as a scalable fabrication technology, more established deposition methods are used both as a benchmark to validate the quality of the layers obtained through inkjet printing, and to fabricate partially inkjet-printed devices to validate inkjet-printed layers individually. In addition, the different families of devices presented in the following chapters require specialized measurement setups for optimal characterization conditions.

This chapter presents a summary of the most relevant fabrication and characterization techniques, as well as the deposition parameters and properties of the materials and inks employed throughout this thesis.

3.1. Fabrication methods

For all the devices shown in this thesis, except for vacuum evaporation processes for top transport layers and metal contacts, all the deposited layers have been carried out in ambient atmosphere. Although more performing devices might be achieved through fabrication in a controlled atmosphere such as a glovebox, fabrication in ambient atmosphere is a vital step for demonstration of the viability of a scalable R2R manufacturing process, as processes demonstrated in glovebox are not cost-efficient compared to ambient manufacture and generally not applicable to a real manufacturing plant.[1]

3.1.1. Spin coating for benchmark LED transport layers

Spin coating is a well-known processing method to deposit thin films from novel inks and materials with high accuracy and reproducibility, common for the fabrication of optoelectronic devices such as OLEDs in a research setting. It consists of a spinning chuck where a substrate is placed (Fig. 3.1 a), on top of which the material of interest is deposited in solution form (on the order of 10-100 µL for a 4 cm^2 substrate). The substrate is then

spun at a speed of generally 1000-6000 rpm, at a specific accelerationwhich causes most of the solution to be rapidly flung away and to partially evaporate, leaving a thin wet layer that can then be submitted to a thermal post-treatment (Fig. 3.1 b). The primary advantage of this technique is its high repeatability combined with a simple fabrication process, with each layer taking 1-2 minutes of processing time per sample.
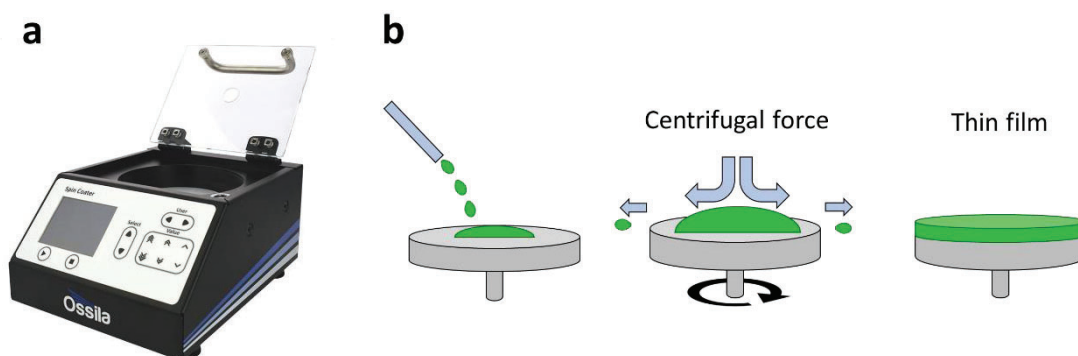
Fig. 3.1 (a) Spin coating unit from Ossila. (b) Schematic representation of the spin coating process

Although a simple process, care should be taken to ensure optimal layer properties when using spin coating. The ink and the wet layers should be free from contamination in the form of particles or dust, and enough ink-substrate wetting should be ensured. Similar to other solution processing techniques, wetting may be improved by the optimization of solvents/additives, or by UV-ozone/plasma treatment of the substrate.

The final thickness of the layer depends on several parameters, including spin speed, spin time, ink viscosity, and ink concentration. To ensure consistency, spin time is generally set so that most of the solvent is removed/evaporated, which is around 30s for most of the common solvents. Of the remaining parameters, spin speed and ink concentration are the most convenient to tune for layer thickness, with an inverse square root law dependence for spin speed and a linear relationship for ink concentration.

Despite the advantages discussed above, spin coating has several drawbacks that constrain its scalability as a process for thin film deposition. First, it is very material inefficient, as most of the solution is discarded. Secondly, the substrate size is limited, with no compatibility with R2R processing. Moreover, it does not allow digital patterning, instead relying on other pattern-definition methods.

Spin coating is introduced in this thesis to fabricate the reference transport layers PEDOT:PSS and Poly-TPD for use in PeLEDs (***Chapter 6***), shown in Fig. 3.2. Spin coated organic materials like PEDOT:PSS and Poly-TPD are reference materials in the literature of thin film LEDs, and spin coating helps to ensure a consistent fabrication process. Here, these materials serve as a benchmark device structure to reference against more the challenging to fabricate, fully inkjet-printed, fully inorganic variants. The spin coating parameters of the solutions showcased in this thesis are summarized in Table 3.1.
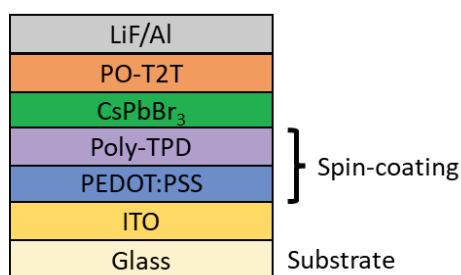
Fig. 3.2 Spin-coated layers demonstrated in ***Chapter 6***.

Table 3.1 Materials deposited by spin coating in this thesis.

Material	Source	Carrier solvent	Solid cnt.	Spin speed	Time	Volume	Thickness per layer
PEDOT:PSS	Heraeus Clevios™ AI 4083	H_2O	1.3-1.7 % wt	3000 rpm	30 s	100 uL	80 nm
Poly-TPD	Lumtec	Chlorobenzene	6 mg/mL	3000 rpm	30 s	50 uL	30 nm

3.1.2. Inkjet printing details

Inkjet printing is the main deposition technology demonstrated in this thesis. It was performed on a Dimatix printer (Fujifilm Dimatix Inc.) with a cartridge of 16 nozzles with a diameter of 21 μm and a nominal drop volume of 10 pL, shown in Fig. 3.3. This printer allows control of drop spacing (printing resolution), platen temperature (up to 60 ºC) during printing, as well as control of jetting parameters including detailed control of waveform shape and amplitude, driving voltage and meniscus pressure, and is compatible with a wide range of solvent families. Waveform control is crucial to achieve jetting of inks a wide range of rheological parameters.[2]

Fig. 3.3 Dimatix DMP-2850 inkjet printer used in this thesis.

The inkjet printing was performed in ambient conditions so, in order to reduce contamination from atmospheric species and particles, the printed layers were placed in a vacuum oven for thermal post-processing soon after deposition. Inkjet printing is the main technology showcased in this thesis, used throughout **Chapters 4-6**. Fig. 3.4 summarizes the materials deposited by inkjet printing.
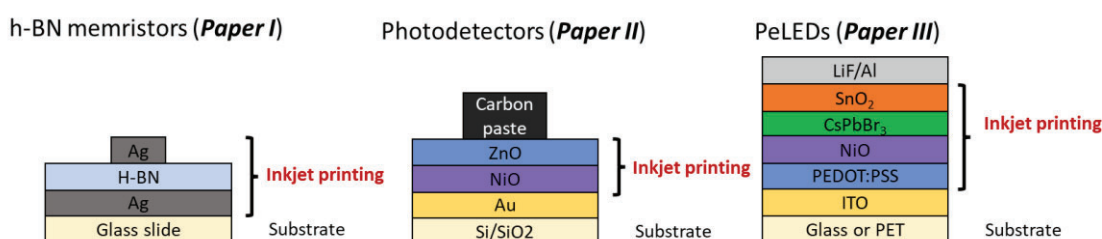
Fig. 3.4 Summary of layers deposited by inkjet printing in **Chapters 4-6**.

The resulting quality of inkjet-printed layers is a complex interplay between ink rheology, ink-substrate interactions, platen temperature, and external parameters such as ambient humidity. As discussed in **Chapter 2**, control of the solvent drying process is paramount to layer homogeneity, which requires the optimization of ink formulation and printing parameters. One of the most common issues is the development of a coffee-ring effect (Fig. 3.5), where the solid content of an ink is dragged to the edges of the wet layer as it dries. Other situations might arise, such as material accumulation in the center of the printed area, which might indicate that a higher platen temperature is required, or a high concentration of pinholes, which indicates insufficient wetting of the ink.
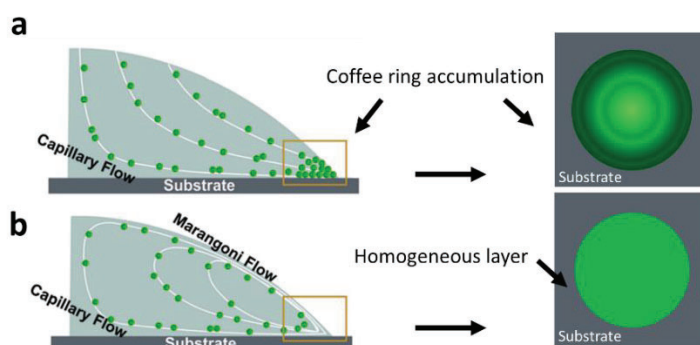
Fig. 3.5 Coffee ring effect: (a) uncontrolled (b) controlled by Marangoni flow. Adapted from.[3]

A summary of the main rheological characteristics and film properties of the inks deposited through inkjet printing in **Chapters 4-6** is presented in Table 3.2.

The following ink parameters affect different deposition conditions and may be modified in order to adapt to printing requirements, such as substrate-ink wetting (carrier solvent/additives), layer thickness (solid content), jettability (viscosity/solvent boiling point), and printed layer roughness (particle size).

Table 3.2 Characteristics of the inks employed in this thesis.

Ink characteristics					
Material	Source	Carrier solvent	Viscosity	Solid cnt.	Particle size
h-BN	In-house formulation	H_2O	2.1 mPa·s	10% wt.	200 nm
Ag	Advanced Nano Products Co.,Ltd	triethylene glycol monoethyl ether	16 mPa·s	40% wt	150 nm
ZnO	Avantama AG	Hexanol	5 mPa·s	2.5% wt	12 nm
NiO	Avantama AG	Hexanol	5 mPa·s	2.5% wt	7 nm
SnO_2	Avantama AG	Hexanol	5 mPa·s	2.5% wt	
PEDOT:PSS	Heraeus Clevios™ AI 4083	H_2O	5-12 mPa·s	1.3-1.7%	80-100 nm (d50-d90)
$CsPbBr_3$	INAM – UJI	Dodecane/Hexane mixture at 3:1 (v/v)	2.3 mPa·s	10 %	7 nm

In addition to the benchmark layers presented in the following sections, screen printing and evaporation have been used to deposit top contacts. Although considerable efforts have been dedicated to the obtention of a fully inkjet-printed photodetector and

PeLED, the deposition of inkjet-printed Ag nanoparticle top contacts has not led to working devices. Unlike the fully inkjet-printed h-BN memristors shown in **Chapter 4**, the fully inkjet-printed photodetector and PeLED architectures discussed in this thesis do not include the top contacts. Attempted photodetectors and PeLEDs with inkjet-printed Ag nanoparticle top-contacts have shown linear (ohmic) I(V) characteristics, suggesting an electrical short circuit between the vertical contacts, perhaps due to Ag^+ ion percolation through the inkjet-printed metal oxide layers. In order to address this challenge, carbon paste (for photodetectors) and evaporated Al contacts (for PeLEDs) have been used for these devices.

The precise deposition conditions optimized for each material to ensure the desired thickness, proper wetting and homogeneous layers are listed and summarized in Table 3.3.

Table 3.3 Inkjet printing parameters for the inks presented in this thesis.

	Printing parameters					
	Material	**Drop spacing**	**Platten temperature**	**Substrate treatment**	**Thickness per layer**	**Post-treatment**
Memristors (**Chapter 4**)	h-BN	20 µm	40 °C	No	50 nm	100ºC or 150 ºC 1h
	Ag	20 µm	No	No	-	100ºC or 150 ºC 1h
Photodetectors (**Chapter 5**)	ZnO	30 µm	No	No	150 nm	200 ºC 1h vacuum
	NiO	30 µm	No	No	150 nm	200 ºC 1h vacuum
LEDs (**Chapter 6**)	PEDOT:PSS	40 µm	40 °C	UV-O_3	300 nm	150 ºC 30' vacuum
	NiO	70 µm	No	No	30 nm	150 ºC 30' vacuum
	$CsPbBr_3$	40 µm	45 °C	No	30 nm 3Layers	95 ºC 10' vacuum
	SnO_2	40 µm	No	No	85 nm	95 ºC 10' vacuum

► h-BN ink details

The h-BN ink was formulated by liquid exfoliation of h-BN powder with a water-carboxy methyl cellulose (CMC) solvent, resulting in a suspension containing multilayer h-BN nanosheets. In order to avoid agglomeration of the nanosheets, CMC-Na was used to stabilize the solution as a result of the steric hindrance and electrostatic repulsive forces from its polar $–CH2–COO^-$ groups. The h-BN flakes in solution have a thickness in the

range of 5-15 nm and a length of around 210 nm, at a concentration of ~1 mg/mL.

► CsPbBr3 NC ink details

The suspensions of CsPbBr3 NCs were prepared by the well-known hot-injection method. After first experiments and device fabrication with ***method 1***, an optimized ***method 2*** was introduced, which improves the removal of excess NC ligands, improving charge injection into the PeLEDs. In either case, the synthesized dodecane and hexane solutions were mixed at a volumetric 3:1 ratio for inkjet-printed deposition. This precise ratio of high and low boiling point solvents was found to counteract the formation of the coffee ring effect, leading to homogeneous perovskite films.

Synthesis method 1: The first synthesis method used is similar to the one presented by Kovalenko's group[4,5] with some modifications. Particularly, the concentrations of oleic acid (OA) and oleylamine (OLA) are increased, leading to a larger concentration of oleylammonium acetate (OLM) ligands at the NC surface, providing enhanced PLQY and stability.[6] All reactants were employed as received.

A Cs-oleate solution is first prepared by loading 0.41 g of Cs_2CO_3 (Sigma-Aldrich, 99.9%), 1.5 mL of oleic acid (OA, Sigma- Aldrich, 90%), and 20 mL of 1-octadecene (1-ODE, Sigma-Aldrich, 90%) into a 50 mL three-necked flask. After vacuum degassing at 120 °C for 1 h under constant stirring, the mixture was purged with N_2 and heated to 150 °C until the Cs_2CO_3 was completely dissolved. The solution was set aside in a N_2 atmosphere at 120 °C.

Following, 10 mL of mixture of OA and oleylamine (OLA, Sigma-Aldrich, 98%) 1:1 in volume is prepared and heated to 130 °C and set aside. After this, 0.85 g of $PbBr_2$ (ABCR, 99.999%) are added to 50 mL of 1-ODE in a 100 mL three-necked flask, and heated at 120°C in vacuum for 1 h with constant stirring, after which the OA and OLA mixture was added to the flask under N_2, and then quickly heated to 170 °C. In addition, 4 mL of the Cs-oleate solution was rapidly added and, after 5 s, the flask was immersed in an ice bath to quench the reaction.

Finally, the NCs are purified. To do this, 60 mL of methyl acetate (99.5%, Sigma-Aldrich) were added to 30 mL of the prepared solution, and then centrifuged at 5000 rpm

for 10 min. Following, the supernatant was discarded to separate the precipitate of NCs, which were redispersed in either dodecane and hexane at a concentration of NCs of 50 mg/mL.

Method 2: Although *method 1* leads to an increased number of OLM ligands at the NC surface, increasing PLQY and stability, these long chain ligands also negatively affect charge injection, reducing PeLED performance.[7,8] Thus, the synthesis is adapted to reduce the number of surface ligands.

First, 0.407 g of Cs_2CO_3 and 1.25 mL of oleic acid are inserted into a 50 mL three-necked flask containing 20 mL of octadecene (ODE) and heated to 120 °C for 1 h in vacuum. Then, the flask was purged with N_2 and heated to 150 °C until the cesium carbonate dissolved completely.

In parallel, 0.345 g of $PbBr_2$, 2.5 mL of OA, and 2.5 mL of OLA were loaded into a 100 mL three-necked flask with 25 mL of ODE, followed by drying at 120 °C in vacuum for 1 h. Then, after establishing a N_2 atmosphere increasing the temperature to 170 °C, 2 mL of Cs-oleate solution was rapidly injected and, after 5 s, the flask was immersed into an ice water bath to quench the reaction.

The solution was centrifuged (5000 rpm, 5 min), and the resulting precipitate was dispersed in hexane (5 mL) after discarding the supernatant. Then, 5 mL of MeOAc was added followed by a second centrifugation (5000 rpm, 5 min). The precipitated solid was redispersed in 1 mL of hexane, and then stored in an Eppendorf vial at -18 °C overnight, after which the solid sediment was removed by decantation. The remaining dispersion was transferred to a glass vial, dried with a N_2 flow, and exposed to vacuum for 15 min, obtaining the $CsPbBr_3$ nanoparticles in solid form.

Finally, in order to obtain the desired concentration (10 mg/mL), the solid was weighed and redispersed in the corresponding volume of hexane or dodecane, and then filtered through a 0.42 μm Teflon filter.

▶   ZnO, NiO and SnO2 details

Successful devices employing metal oxide layers were fabricated with nanoparticle inks based on hexanol provided by Avantama AG. These inks, consist of a stable 2.5 wt%

dispersion in hexanol using an undisclosed dispersant (proprietary information of Avantama AG). The consistent 5 mPa·s viscosity and boiling point of hexane across these inks ensures consistent jetting and allows the obtention of functional layers at boiling points <100 ºC, as demonstrated in *Chapter 6*, crucial for compatibility with the thermal restrictions of perovskites and flexible substrates.

►   Substrates

Substrate choice is crucial for the successful deposition of functional thin films, particularly in inkjet printing, as it affects the properties and performance of the resulting layers in several ways. The surface energy of the substrate plays a role in determining the wettability and contact line pinning properties of the ink-substrate interaction, thus setting an upper limit on drop spacing and the ability to print a defined geometry. In addition, substrate surface roughness affects the final roughness of the printed layer, which is particularly evident in soft, flexible substrates. Moreover, other factors such as substrate maximum tolerable temperature (e.g., in plastic flexible substrates), limit the processability of the printed layers. Thus, these multiple constraints limit the choice of substrate for a certain application.

The memristors in *Chapter 4* were inkjet-printed on glass slides (Ag/h-BN/Ag) and Ti-coated Si/SiO$_2$ wafer (Ag/h-BN/Pt). Similarly, the photodetectors fabricated in *Chapter 5* were deposited on Au-coated Si/SiO$_2$ wafer. Silicon wafer is a standard substrate for reliable vacuum deposition of metal thin films. On the other hand, Ag nanoparticle inks can be readily deposited on standard laboratory glass slides.

The PeLEDs demonstrated in *Chapter 6* were fabricated on standardized ITO-coated substrate formats in order to simplify the fabrication and characterization process. Two formats were used: the first format, provided by Ossila, consists of a 15x20 mm ITO-coated glass with a 6-pixel pattern (Fig. 3.6 a) and is compatible with compact and transportable Ossila's measurement system (explained below). The second format is a 20x20 mm ITO-coated glass substrate (Fig. 3.6 b) compatible with the second measurement system. For flexible LED fabrication, a similar 20x20 mm PET/ITO substrate was introduced. In any of these cases, substrate cleaning and device fabrication follow a similar process, save for adaptation to the different shapes.
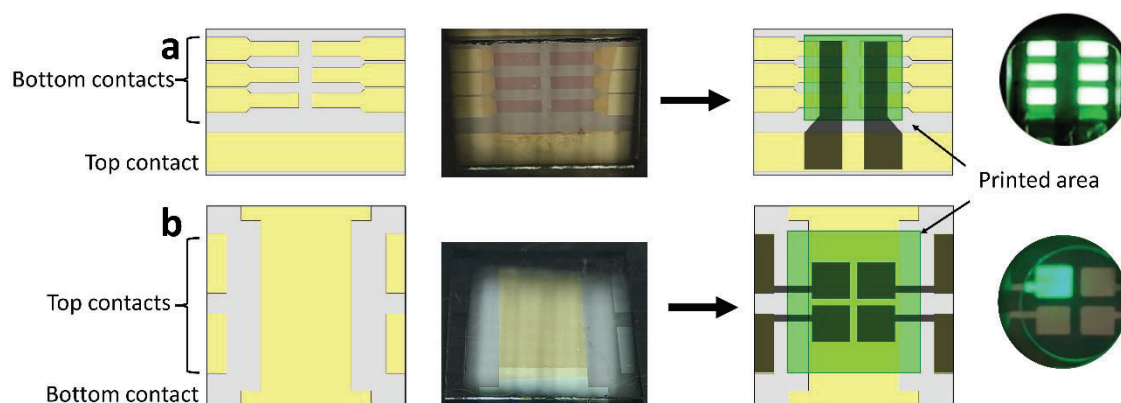
Fig. 3.6 Glass/ITO substrates used for PeLED fabrication (the yellow color corresponds to the ITO contacts). (a) 15x20 mm Ossila substrate (b) 20x20 mm substrate. The rightmost images show the geometry of the top contacts and printed area for each substrate.

Prior to deposition, substrate cleaning is a critical process that removes contamination such as solid particles and organic residue, ensuring optimal wetting characteristics and a smooth, pinhole-free final layer. The substrates for Photodetectors and PeLEDs (***Chapter 5*** and ***Chapter 6***) were first cleaned to remove unwanted particles and residues. First, they were cleaned using a 3% Hellmanex soap solution in an ultrasonic bath for 5 min. Further cleaning was done using deionized water, acetone and isopropanol respectively in an ultrasonic bath each for 5 min. Finally, the substrates were dried with an N_2 gun and stored in a vacuum desiccator for later use.

►   Encapsulation for PeLEDs

While the demonstrated devices should be able to withstand fabrication in ambient conditions, encapsulation is a standard process to insulate devices from the long-term exposure to ambient contaminants over the device's useful life. Encapsulation is a crucial aspect for commercial OLED display manufacture which, like perovskites, are sensitive to species like moisture and oxygen.[9–11]

For the encapsulation of the PeLEDs after fabrication, a photocurable glue acquired from Lumtec (LT-U001) was applied over the device active area, and a glass cover slide (Thermo scientific MENZBC080080A120) was carefully placed on top. To harden the curable glue, the devices were exposed to UV light for 4 minutes.

3.1.3. Thermal vacuum evaporation

Thermal evaporation is a physical deposition technology that is based on the application of heat to a target material to cause either its evaporation or sublimation, depending on the material, depicted in Fig. 3.7. This is an ideal process for organic small molecule materials, which require relatively low temperatures of ~ 300 ºC. However, materials with higher sublimation/evaporation temperatures such as metals or metal oxides may require the use of special crucibles or more specialized techniques such as sputtering or electron beam evaporation. A sufficiently high vacuum is required in order to ensure a long enough mean free path for the target species to reach the substrate, generally a value below 10^{-4}-10^{-5} mbar. The deposited thickness and current rate of deposition are assessed by a quartz crystal sensor exposed to the flux of material, by measuring the change in natural frequency of the quartz crystal in accordance with the deposited mass.
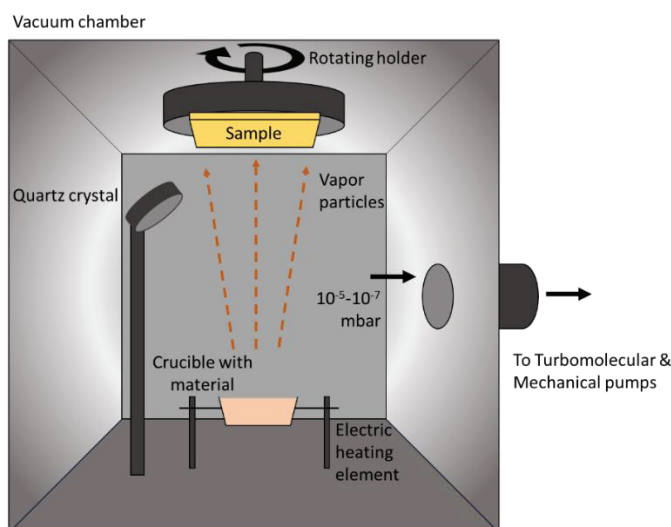
Fig. 3.7 Schematic diagram of a vacuum evaporator chamber.

In order to obtain high quality films, a controlled rate of deposition must be ensured. The ideal rate of deposition, usually measured in Å/s, depends on the specific material: for organic materials, a rate of ~0.1-0.3 Å/s is generally adequate, while for metallic contacts a higher rate of ~0.5-1 Å/s may be employed. The rate of deposition of the material can be controlled simply by tuning the applied heating power. In addition, as is common with other physical deposition processes, the substrate can be kept in rotation to

improve the homogeneity of the deposited layer.

Thermal evaporation requires the use of masks to define layer geometry, and due to size restrictions of the vacuum chamber, a limited number of samples can be processed at once. This process has been employed in this thesis to deposit the top organic electron transport layers (PO-T2T), the metallic contacts (Al) and the LiF interlayer for the PeLEDs of **Chapter 6** and the metallic contacts of the SnO_2/NiO photodetectors presented in Chapter 4 (Fig. 3.8). Evaporated materials in **Chapter 6** serve as reference layers, as the previous layers are spared of the interaction with solvents and other chemical species that would occur with solution processed layers.
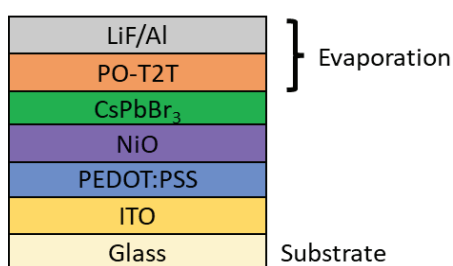
Fig. 3.8 Evaporated PO-T2T, LiF and Al layers demonstrated in **Chapter 6**.

3.2. Morphological and structural characterization methods

3.2.1. h-BN memristors

The h-BN nanoflakes were studied by scanning electron microscopy (Supra 55, Carl Zeiss), atomic force microscopy (Multimode V, Veeco), and transmission electron microscopy (JEOL JEM-2100 with a working voltage of 200 kV).

3.2.2. NiO and ZnO for photodetection

ZnO and NiO layers were studied by FE-SEM (JEOL J-7100) Their crystalline structure was studied by XRD (Japan Rigaku D/Max-IIA X-ray diffractometer using Cu Kα radiation, λ = 1.5406 Å).

3.2.3. CsPbBr3 LEDs

Scanning electron microscope (SEM) images were acquired using the FEGSEM – JEOL 3100F system.

3.3. Device characterization methods

3.3.1. Electrical characterization of h-BN memristors (Chapter 4)

An Agilent B1500 semiconductor analyzer, paired with a Cascade Microtech M-150 probe station, and a temperature control stage (SP72-T2, ERS electronic GmbH) was used for electrical characterization of h-BN memristors (***Chapter 4***). This setup allows sub-pA measurements thanks to the combination of high-precision SMUs, the incorporation of triaxial cables and the Faraday shielding from the closed probe station. This system allows for a number of measurement modalities through direct control of the SMUs, including ramped scan, pulsed, and constant voltage application.

3.3.2. Photovoltaic and optical characterization of NiO/ZnO photodetectors (Chapter 5)

A setup composed of a second Agilent B1500 semiconductor analyzer, in this case paired with a Bentham PVE300 system, was used to characterize Photodetectors (***Chapter 5***). The Bentham PVE300 system includes a class B solar simulator that emits at 1 kW/m^2. It also allows UV-Vis spectral measurements of transmittance and reflectance thanks to an included integrating sphere and monochromated light from a Xenon and Quartz lamp combination.

3.3.3. Integrated device characterization of PeLEDs (Chapter 6)

All the device characterization of PeLEDs (***Chapter 6***) was performed in ambient conditions after encapsulation. A photocurable glue (Lumtec LT-U001) and a glass slide cover (Thermo scientific MENZBC080080A120) were applied to encapsulate the active area with 4 min exposure to UV light.
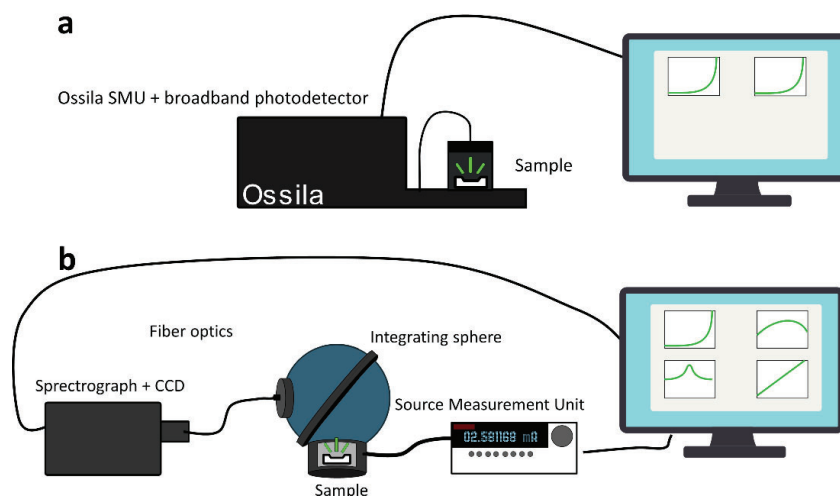
Fig. 3.9 LED characterization setups used in *Chapter 6*.

The characterization of LEDs in *Chapter 6* was accomplished by means of two setups. The first setup consists of an OSSILA automated measuring system (Fig. 3.9 a). This is a simple setup that can perform I(V) measurements of LEDs and output relative measurements of electroluminescence intensity. Despite its simplicity, this setup is useful for quick measurements to identify high and low performing samples.

Once the most promising architectures have been identified, a more advanced setup is used. The second setup consists of an integrated system formed by a *Hamamatsu C9920-12 external quantum efficiency measurement system,* a *GAMRY Reference 3000 potentiostat* coupled with an *Andor-iDUS DV420A-OE CCD detector* and a *Kymera 1931-B2 spectrograph* (Fig. 3.9 b) and is capable of measuring I(V) curves in addition to spectral and integrated electroluminescence parallelly.

An integrating sphere allows to collect most of the light emitted by a device, providing accurate estimation of radiometric and photometric quantities. The use of an integrating sphere (represented in Fig. 3.10) allows the measurement of two key parameters of LED characterization: luminance (usually expressed in cd/m^2) and EQE (usually expressed as a percent value). In an integrating sphere ideally, all light emitted by the LEDs can be measured (radiant flux, in units of watts), although it is generally underestimated as a fraction thereof is trapped in the LED substrate by total internal reflection.
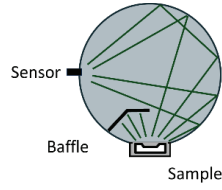
Fig. 3.10 Schematic of operation principle of an integrating sphere as the one used in **Chapter 6**.

Luminance is a measure of the apparent brightness of a surface, used as an industry-standard figure of merit for display technologies, measured as the luminous intensity (in candelas) per emissive unit area. For example, the European broadcasting union's *EBU Tech 3320* [12] specification sets standards for ordinary displays starting at a luminance range of 70 to $\geq$100 cd/m², and for high dynamic range displays starting at $\geq$500 cd/m².

Moreover, external quantum efficiency (EQE), which is a measure of device efficiency, can also be estimated from characterization in an integrating sphere. EQE is equal to the ratio of photons emitted vs. charge carriers injected into the LED (eq. 3.1). By considering the emission spectrum of the LED, the photon flux can be estimated from the measured radiant flux (eq. 3.2), while the charge carrier flux is directly calculated from the injected current (eq. 3.3).

$$EQE = \frac{Injected\ charge\ flux}{Emitted\ photon\ flux} = \frac{\Phi_q}{I_e} \tag{eq. 3.1}$$

$$\Phi_q = \int_{\lambda_1}^{\lambda_2} \frac{\lambda}{hc} \frac{d\Phi_e}{d\lambda} d\lambda \tag{eq. 3.2}$$

$$I_e = \frac{I}{q} \tag{eq. 3.3}$$

REFERENCES

1. Shah, M. A., Lee, D.-G., Lee, B.-Y. & Hur, S. Classifications and Applications of Inkjet Printing Technology: A Review. *IEEE Access* **9**, 140079–140102 (2021).

2. Zhang, M., Meng, L., Deng, H. & Liu, H. Controllable patterning of nanoparticles *via* solution transfer processes. *Mater Chem Front* **5**, 5247–5256 (2021).

3. EBU Tech 3320 specification .

Chapter 4

Inkjet-printed h-BN memristors for hardware security

T section explores an alternative branch of applications of resistive switching in the fields of digital security as physical unclonable functions (PUFs) and true random number generation (TRNG) with inkjet-printed LPE 2D hexagonal boron nitride (h-BN) memristors by exploiting the stochastic nature of these devices.

Memristor research has generally focused on exploiting the resistive I-V hysteresis cycle and pulse response of resistive switching devices (RSDs) to store bits of information, and their subsequent application as memory elements for standard computers. Later research moved the attention to their use not only as memory elements, but as computing units too, for example by employing an array of RSDs in a *crossbar* configuration that can perform a vector-matrix multiplication (commonplace in artificial neural networks) analogically. Beyond these, even more exotic applications of RSDs have been proposed in the form of neuromorphic computing, a field that attempts to process signals by replicating the function of biological neurons.

Such memristor architectures have traditionally consisted of metal-insulator-metal (MIM) structures with transition metal oxides such as HfO_2, Al_2O_3, TiO_2 and TaO_x.[1] Recently, however, the trend of incorporating 2D graphene-like materials like h-BN in diverse electronic applications is taking hold,[2] including RF components,[3] as a deep UV emitter,[4] as insulating layers for various devices,[5–7] as diffusion barriers for chemical species,[8] and as insulator in high performance memristors.[9–11] This breadth of applications originates thanks to the unique properties of layered materials,[12,13] representing a possible avenue to achieve electronic devices beyond traditional complementary metal oxide semiconductor (CMOS) technology.[14,15]

In particular, h-BN has high chemical robustness, high mechanical flexibility, and transparency,[12,16] enabling improved enhanced device stability and fabrication for wearable, transparent devices. Thanks to its ability to be deposited as an atomically flat surface free of dangling bonds, it has potential for ultra-dense integration.[17,18] Particularly, MIM memristors based on h-BN have shown remarkable features such as coexistence of

both volatile and nonvolatile switching,[1,12] high LRS/HRS ratio and low power consumption,[19] and even ultrathin monolayer devices have been demonstrated.[20]

However, most reported studies on 2D-based memristors rely on fabrication processes not compatible with wafer-scale electronics manufacture, such as mechanical exfoliation, a non-scalable process,[21] or chemical vapor deposition, which despite its scalability has high temperature requirements (>850 ºC) which complicate compatibility with CMOS fabrication, thus requiring a tedious transfer process that is time consuming and can easily produce cracks in the material.[22–25] In addition, monolayer deposition of h-BN has stringent requirements, needing to ensure an ultra-flat surface to avoid variability due to roughness.[26] In contrast, liquid phase exfoliation (LPE) is a cost-effective method that uses microfluidization or an ultrasonic bath to exfoliate bulk crystals, achieving a suspension of few nm-thick and few hundred nm-long nanoflakes, thanks to the relatively weak van der Waals forces of layered materials.[2] These liquid suspensions of 2D sheets can then be used to deposit h-BN at low cost and low processing temperatures through small scale solution processing routes such as drop-casting, spin coating, or scalable ones like inkjet printing,[21] and allowing the coating of non-planar surfaces, such as those of wires, electrodes and channels.[27] A multitude of microelectronic devices have been demonstrated through the LPE method, including capacitors,[28] transistors,[29] light emitting diodes,[30] photodetectors,[31] and solar cells.[32] Particularly, 2D material-based memristors obtained through LPE have shown interesting properties, such as the concurrence of both volatile and non-volatile switching, controllable potentiation and depression characteristics, ultralow power consumption, high thermal stability, flexibility, and transparency.[33]

Despite the compatibility of LPE with scalable inkjet printing deposition, inkjet-printed h-BN memristors are scarce in the literature, with an abundance of researchers opting for non-scalable, simpler methods such as spin coating. While inkjet printing has indeed been demonstrated with LPE 2D material-based memristors, examples in the literature demonstrate comparably lower-performance insulator materials such as graphene oxide, MoS_2 and black phosphorous. Such materials, in contrast to h-BN's high bandgap (~6 eV), dielectric constant (k = 4-6)[5] and high resistance to the diffusion of chemical species,[8,34] lead to memristors with lower endurance and shorter retention times

(see tables at the end of the chapter: Table 4.1 to Table 4.4).[19,35]

Due to the irregularity in size and thickness of flakes obtained through the LPE method, solution processing fabrication of 2D material based memristors produces layers with irregularities in thickness and flake boundaries, which lead to increased variability in performance.[26] Device variability is inconvenient for memory and computation applications, where predictable operation is desirable.[36] Nonetheless, this property is ideal for applications that require true random number generation.[37] Fig. 4.1 shows a conceptual sketch of two arrays of memristors, each with different switching thresholds, outputting their own unique identifiable outputs.
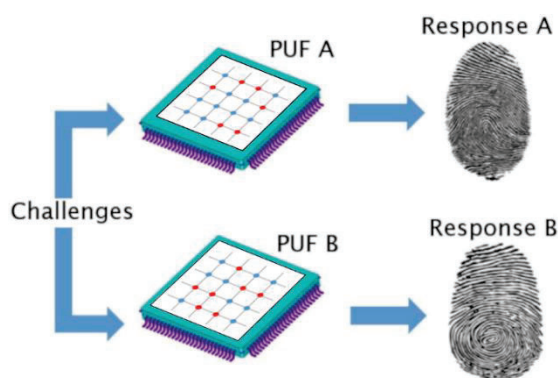
Fig. 4.1 Concept of memristor-based PUFs. Two PUFs, here based on memristors, respond with their respective unique identifiable outputs (configuration of red and blue dots in the matrix) when presented with a challenge. Adapted from Ref [38].

In the following sections, an inkjet-printable h-BN ink formulated through the LPE method is used to fabricate memristors in Ag/h-BN/Pt and Ag/h-BN/Ag structures by inkjet printing. These devices show device-to-device variability in initial resistance state and forming voltage, and cycle-to-cycle variability of resistance states within the same device. Thanks to their cost-effective, scalable fabrication method, the stochastic behavior of these devices is proposed for use as hardware security primitives, such as PUFs and TRNG circuits.

4.1. Fabrication of the h-BN memristors

The novelty introduced in the fabrication process of the memristors presented here lies in the inkjet-printed fabrication of h-BN, representing the first fully inkjet-printed h-BN memristors in the literature. Two inks were used: h-BN and Ag nanoparticle ink. The h-BN ink was formulated as described above, while the Ag nanoparticle ink was purchased from Advanced Nano Products. Two device structures are proposed, both pictured in Fig. 4.2.

Structure 1, consisting of Ag/h-BN/Pt, was fabricated on commercially available SiO$_2$/Si substrates, where the Pt back contact was deposited by electron beam evaporation on a SiO$_2$/Si wafer. The h-BN and Ag layers were inkjet-printed using a Fujifilm Dimatix DMP-2850 inkjet printer with a nominal drop volume of 10 pL, and then submitted to a thermal post-treatment of 1h at 150 ºC each, sequentially.

Structure 2, a fully inkjet-printed architecture consisting of Ag/h-BN/Ag, was fabricated in a similar manner on standard glass substrates. In this case, the thermal post-treatment was 1h at 100 ºC per layer.

In all cases, the device geometry is defined vertically by the top Ag contacts, which are circular with a diameter of 60 μm.
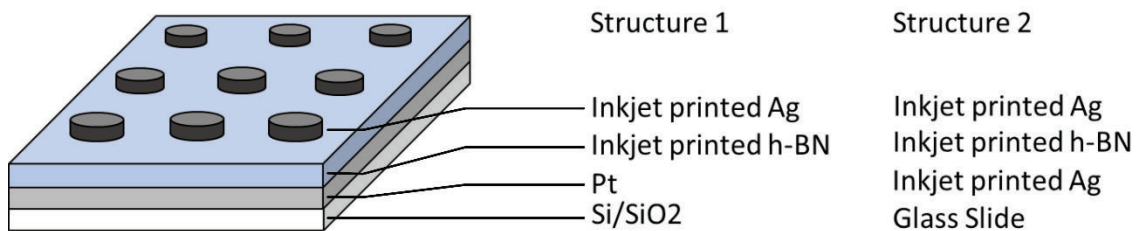
Fig. 4.2 Inkjet-printed h-BN Memristor structures presented.

4.2. Characterization of the h-BN inkjet-printed layers

The h-BN ink formulation used here is similar to that characterized and used in previous works by our research group.[39,40] Nonetheless, the ink is again characterized to confirm its properties. Fig. 4.3a shows a vial of the h-BN ink, with its characteristic white color. Fig. 4.3b shows a top-view SEM image of an individual Ag/h-BN/Pt memristor

fabricated on a 300 nm SiO$_2$/Si wafer. The continuous nature of the h-BN nanoflake film can be verified by AFM (Fig. 4.3c), showing a surface roughness of 5.6 nm, while a thickness of ~250 nm is confirmed through cross-sectional SEM (Fig. 4.3d). Cross-sectional TEM analysis of the Ag/h-BN/Pt devices suggests excellent crystallinity (Fig. 4.3e–h), later confirmed by Raman spectroscopy (Fig. 4.3i), and reveals a monolayer thickness of 0.33 nm, consistent with values reported in the literature.[41]
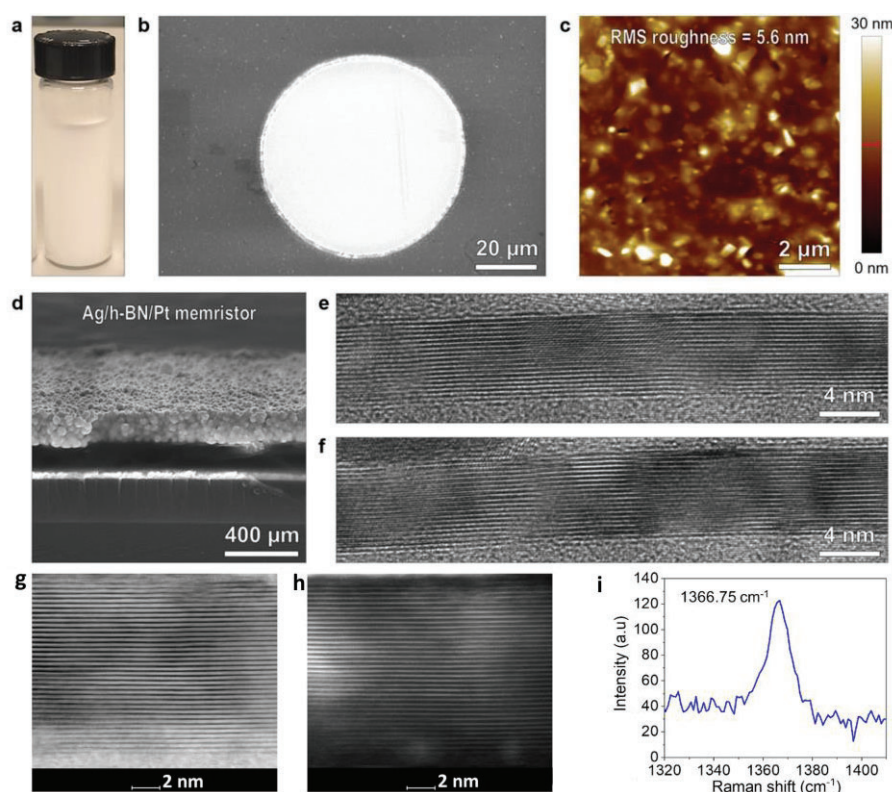
Fig. 4.3 (a) Picture of vial h-BN ink. (b) Top-view of individual inkjet-printed Ag/h-BN/Pt memristor by SEM. (c) Surface of inkjet-printed h-BN film through AFM (d) Cross-section of Ag/h-BN/Pt memristor by SEM. (e and f) Cross-section TEM imaging of h-BN nanoflakes with in the inkjet-printed thin film. (g and h) Cross-section scanning TEM (STEM) images of the same h-BN nanoflake in bright field (BF) mode and high-angle annular dark field (HAADF) mode. In the BF image (left), the black lines represent h-BN. In HAADF mode, the white lines represent h-BN. (i) Raman spectrum of the inkjet-printed h-BN thin film

The shape of the single nanoflakes is studied by AFM and top-view TEM on a microperforated copper grid (Fig. 4.4a and b, respectively), showing an average lateral length of 210 nm and a thickness between 5 and 15 nm (corresponding to 15-45 layers).
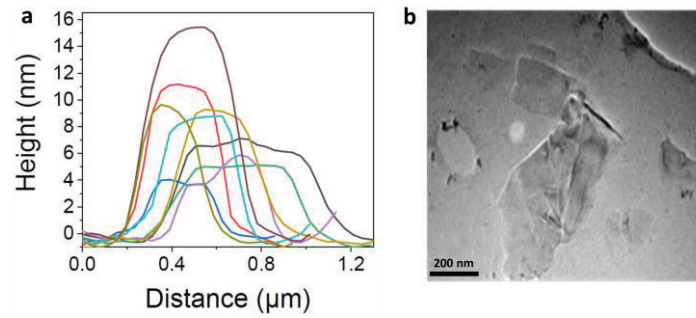
Fig. 4.4 (a) Flake height profiles obtained by AFM. (b) Top-view TEM of single h-BN nanoflakes.

4.3. Characterization of h-BN memristor switching characteristics

In the following subsections, different modes of operation for the inkjet-printed h-BN memristors are proposed and showcased. Since stressing an RSD in a particular way may modify its microscopic structure permanently and thus its electrical behavior, each of the modes of operation described here are tested on different subsets of devices, which have nonetheless been fabricated on the same substrate and in the same conditions.

Three different excitation modalities are showcased in this chapter: ramped voltage stress (RVS), pulsed voltage stress (PVS), and constant voltage stress (CVS). In RVS, the applied voltage is ramped once forwards and then once backwards in a voltage range were switching is expected to happen (Fig. 4.5a). In PVS, voltage pulses are applied to the device to elicit switching (Fig. 4.5b). Read pulses, of a lower voltage to avoid modification of the current state, are generally used to check the resistive state of the memristor before and after switching. Finally, in CSV the memristor is submitted to a constant voltage while the current is monitored.
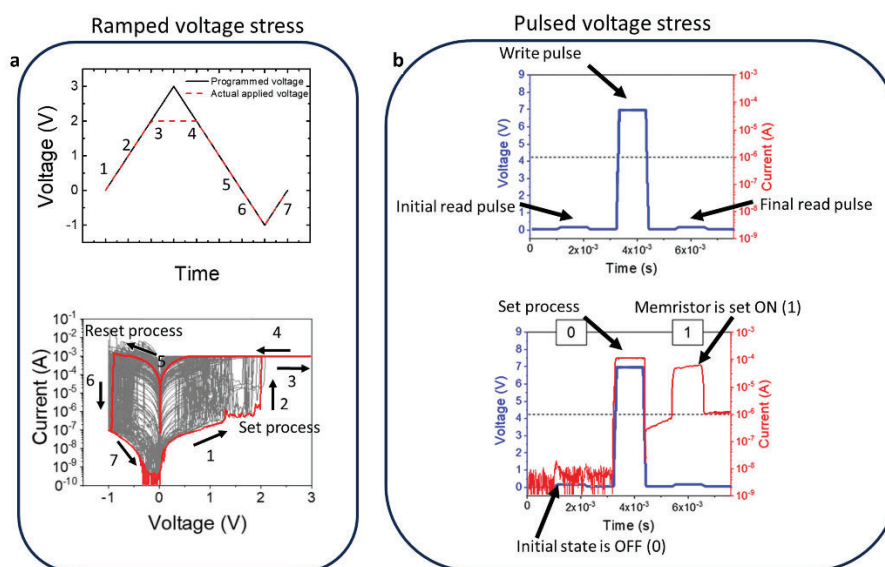
Fig. 4.5 Memristor excitation with (a) RVS and (b) PVS

4.3.1. Initial ramped voltage characterization

The h-BN devices were first submitted to sequences of ramped voltage stresses (RVS) to induce a device forming cycle and elicit resistive switching behavior. Upon study of the I-V curves obtained, the devices start at a high resistance state (HRS), transitioning to a low resistance state (LRS) as the voltage is increased (Fig. 4.6a). The abrupt, non-linear character of this transition suggests a filamentary switching mechanism. These devices showed a high device-to-device variability in dielectric breakdown voltage of 0.4 - 16 V and in pristine resistance of 10^7 - 10^{10} Ω (Fig. 4.6a and b). This variation can be attributed to micro- and nanoscopic variation of the devices, e.g., fluctuation in h-BN nanoflake thickness and stacking, as well as remaining impurities such as solvents within the device structure.
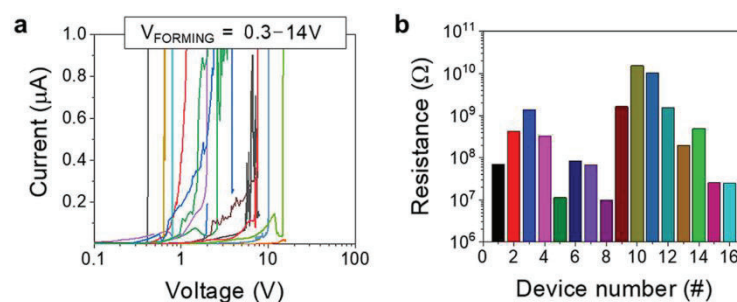
Fig. 4.6 a) I-V curves of the forming process of 16 devices show the variability in switching threshold of the Ag/h-BN/Pt memristors. b) variability in initial resistance level after forming.

While this variability in switching threshold might at first seem discouraging, as most applications of memristors require some level of uniformity of the resistive states, the variability shown by these h-BN memristors can be leveraged to build physical unclonable functions (PUFs).

4.3.2. Pulsed operation for PUF applications

PUFs are devices that return a specific, unique output (response) when a given input (challenge) is given to them. One of the main characteristics of PUFs is the inability to predict what the response of a particular PUF will be, ensuring robustness against malicious attacks, which can be achieved by exploiting the variability in switching threshold that the inkjet-printed h-BN devices display. A proof of concept is carried out where a new group of 16 h-BN memristors presented in Fig. 4.6 are submitted to a programming pulse train consisting of a read pulse of 0.1 V for 1 ms, a set pulse of 8 V for 1 ms, and a final read pulse (Fig. 4.7). Thus, the initial state of the device is first measured with a low-voltage pulse, then a higher voltage programming pulse is applied in an attempt to switch the device to an LRS, and later the final state of the device is confirmed.

Due to the fluctuations in device properties, the initial state of the devices may be at either HRS or LRS stochastically. In addition, due to variability in switching threshold, for devices starting at HRS only a subgroup may switch to an LRS. This variability is indeed observed in the 16 devices measured here, highlighted in Fig. 4.7a-c respectively: some devices start in HRS and don't switch, some start in HRS and switch to LRS, and other start in LRS and stay that way.
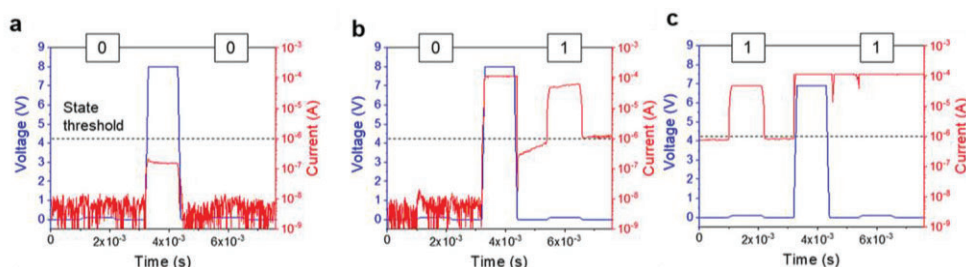
Fig. 4.7 Illustration of three possible scenarios when applying the programming pulse. a) device starts in state 0 and remains in state 0 b) device starts in state 0 and switches to state 1 and c) device starts in state 1 and remains in state 1.

Each of the h-BN memristors are determined to be OFF/ON (0/1) by setting an (arbitrary) cutoff for HRS/LRS of 10 MΩ. Initially, 3 out of 16 devices were in the ON state, and after the programming pulse, 7 out of 16 were found to be in the ON state. Fig. 4.8 shows the detailed currents of the 16 devices as they are exposed to the pulse train.
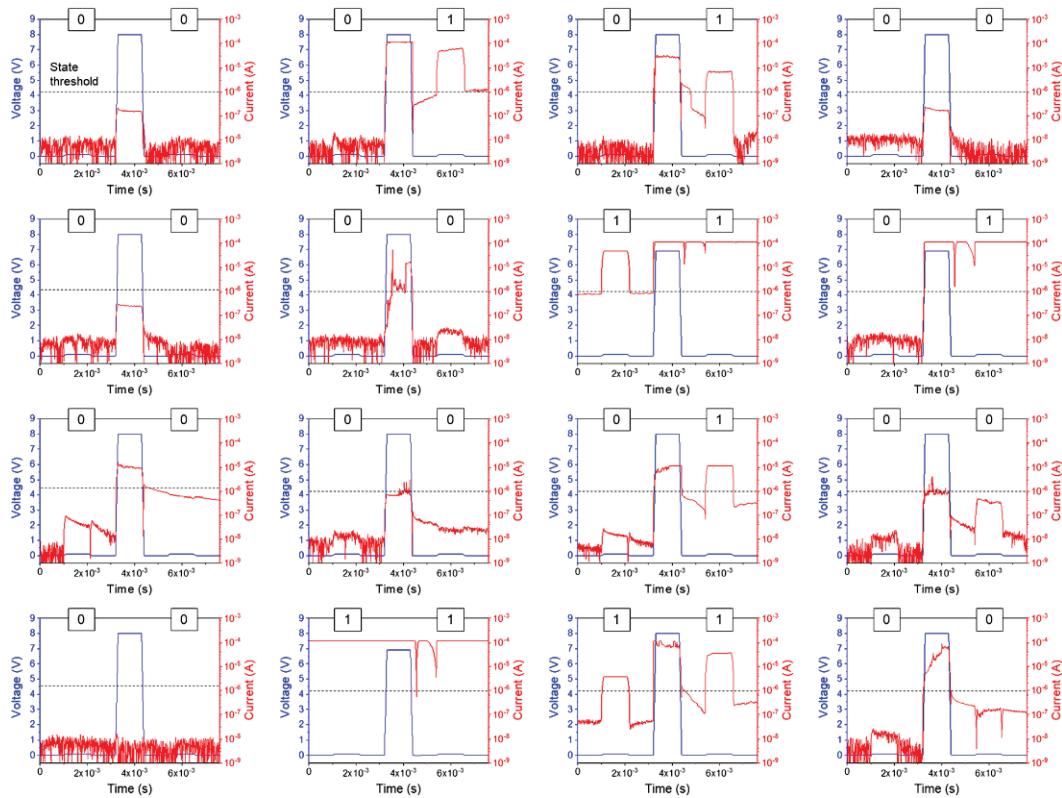
Fig. 4.8 Results after applying the voltage pulse train to a set of 16 devices.

This unpredictable behavior across the ensemble of devices creates a specific configuration of OFF/ON devices, i.e. the "fingerprint" in Fig. 4.9, which can be used as a unique identifier (PUF).
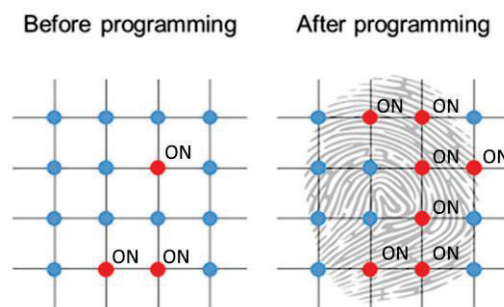
Fig. 4.9 Creation of an arbitrary pattern by applying the voltage pulse train to the group of 16 h-BN devices, corresponding to the initial and final states shown in Fig. 4.8.

In this pulsed voltage PUF configuration scheme, the set pulse is a critical parameter, as it needs to be tuned according to the stochastic properties of the memristor ensemble in order to achieve a final configuration of mixed ON/OFF devices. A set pulse that is too high voltage (or too long) would produce a configuration of mostly ON devices, while the opposite would lead to mostly OFF devices, thus creating a combination unusable as a unique identifier.

The method to prepare PUFs proposed here can generate truly random, unique keys in a facile way. Since the final ON/OFF device configuration ultimately stems from nano- and microscopic variations in device properties originating at the time of fabrication, this method of PUF configuration is unpredictable. Furthermore, the number of unique identifiers scales quickly with the number of devices, enabling many unique identifier tags. In this particular example using only 16 devices, the possible number of combinations ascends to $2^{16} = 65\ 536$, while at 30 devices, this number surpasses 1 billion ($2^{30} = 1\ 073\ 741\ 824$).

4.3.3. High endurance volatile threshold RVS switching property

A different switching typology, known as threshold switching, is characterized by a SET resulting an abrupt increase in current once a certain voltage is reached through a RVS but, as the voltage stress is removed, the device returns to the OFF state, a switching property that finds applications in hardware implementations of artificial neural networks.[42,43]

The Ag/h-BN/Pt memristors exhibit volatile unipolar threshold switching when submitted to RVS with a low current limitation (≤ 1 µA), in either polarity (Fig. 4.10 a-d). When the resistance levels of these two states are analyzed, they show a statistical distribution where the LRS and HRS are well defined with mostly separated states (approximately a factor $R_{HRS}/R_{LRS} \approx 10$) and limited overlap (Fig. 4.10 e and f). In these conditions, the h-BN devices show repeatable switching for up to 0.6 million cycles, the highest endurance reported to date for a memristor fabricated using the liquid phase exfoliation method (see tables: Table 4.1 to Table 4.4).
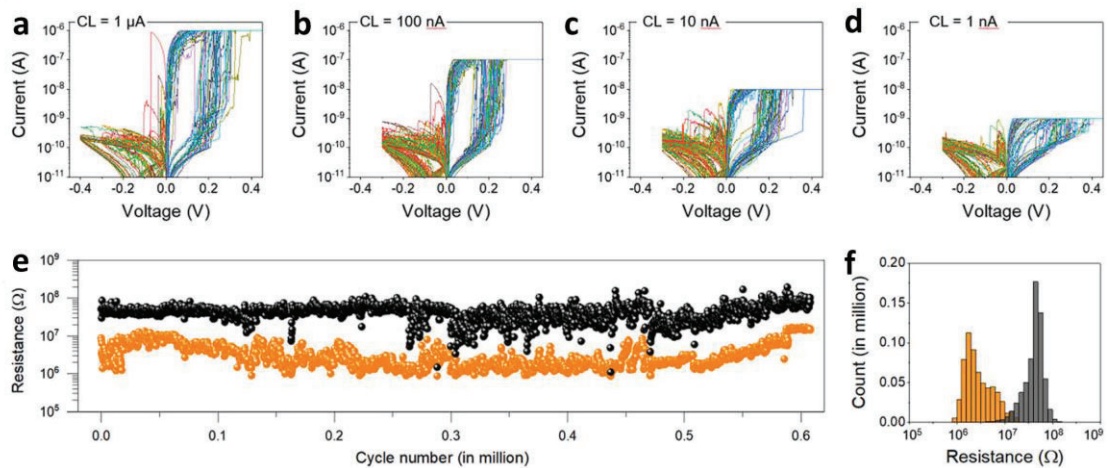
Fig. 4.10 a)-d) Ag/h-BN/Pt memristors operating in volatile threshold RVS mode at different current limitations from 1 uA to 1 nA. e) resistance levels in each cycle extracted from the experiment at a). f) statistical distribution of resistance levels from e), showing limited overlap between HRS and LRS.

In contrast, when the current limitation is raised to >10 µA, the memristors show non-volatile bipolar RS (Fig. 4.11a). Analysis of the LRS when measured in this way reveals relatively low dispersion in resistance (Fig. 4.11b), which could find applications as memory units.
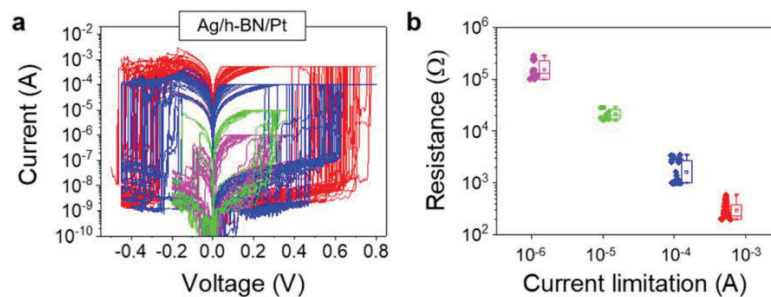
Fig. 4.11 (a) I-V plot of RVS measurement of Ag/h-BN/Pt memristors under current limitations ranging from ~1 µA to 1 mA, displaying non-volatile RS. (b) Plot of dependence of the resistance of the LRS on the current limitation, showing relatively tight dispersion within the same order of magnitude.

4.3.4. Self-recovery effect of LRS and fabrication of symmetrical Ag/h-BN/Ag devices

One of the most common modes of failure in resistive switching devices consists of failure to recover from the LRS.[44] The Ag/h-BN/Pt memristors studied in this chapter are robust to this failure mode thanks to a self-recovery effect. Even when operated in conditions that lead to non-volatile switching (i.e. higher current limitations up to 1 mA), the h-BN memristors spontaneously return from the ON state (LRS) back to the OFF state (HRS) after a time period allowing the h-BN memristors to not remain stuck in the LRS

indefinitely. Fig. 4.12 shows this effect, showing an inverse relationship between the retention time and the starting resistance of the LRS. This observation is consistent with a filamentary switching mechanism, stemming from the diffusion of highly mobile Ag^+ species originating in the Ag contact under electrical polarization.[45]
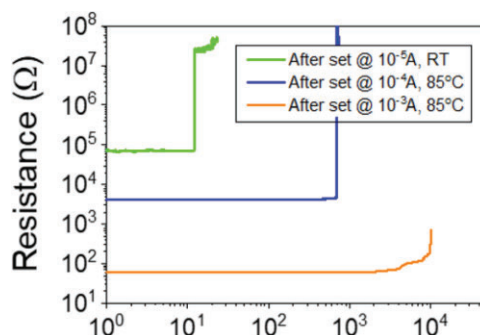
Fig. 4.12 Retention time of LRS at different conditions, showing the self-recovery effect.

In light of this proposed switching mechanism mediated by Ag^+ ions, and in order to exploit the stochastic property of the h-BN memristors, a symmetrical, fully-inkjet-printed Ag/h-BN/Ag device structure is proposed. This symmetrical structure should allow the injection of Ag^+ ions from both contacts according to the polarity of the applied voltage, leading to an increased injection of Ag^+ ions and thus an increased number of intermediate states with more overlap between HRS and LRS. Measurement with RVS of the Ag/h-BN/Ag devices shows non-volatile bipolar RS (Fig. 4.13).
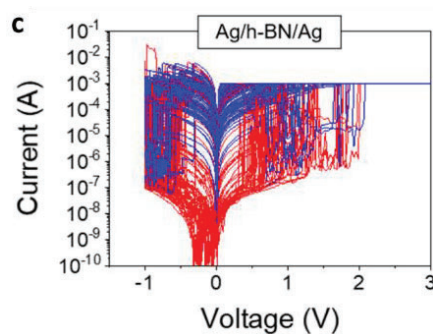
Fig. 4.13 I-V plot of RVS measurement of Ag/h-BN/Ag memristors under a current limitation of 1 mA, displaying non-volatile RS.

The Ag/h-BN/Ag structure also shows the self-recovery effect. Remarkably, measurement by PVS of the symmetrical device structure reveals that no devices remained stuck at the LRS permanently. Remarkably, in the worst case observed, the device persisted for <9% of operation time (Fig. 4.14).
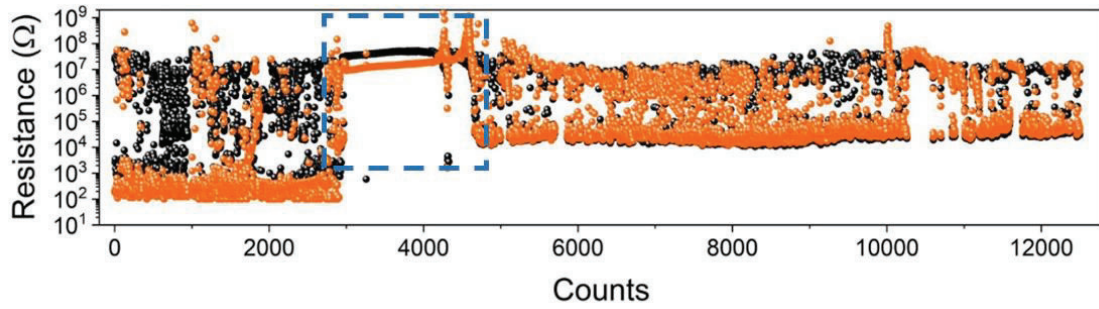
Fig. 4.14 Endurance test of Ag/h-BN/Ag memristors showing the self-recovery effect in action between cycles 3000-4500 and 10000-15000 (highlighted).

4.3.5. Entropy source property

When subjected to pulsed voltage stresses (PVS) with a current limitation of 1 mA, the Ag/h-BN/Pt memristors show non-volatile bipolar switching with an HRS that varies stochastically with each cycle in the range of $10^6 - 10^8$ Ω (Fig. 4.15 a-b). This mode of operation may be exploited as an entropy source, i.e. a random number generator, by comparing the resistance of the HRS with an (arbitrary) cut-off resistance level to generate a series of 1 and 0 values. For example, setting a threshold resistance of $R_{TH} = 50$ MΩ in Fig. 4.15a, 656 of the cycles would yield a 0 state, and 202 would yield a 1 state.
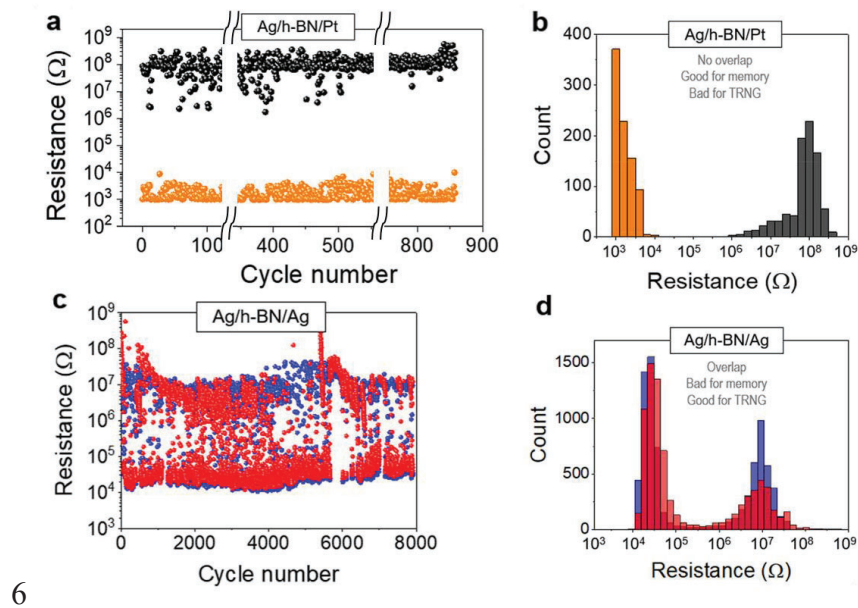
Fig. 4.15 Resistance states under pulsed operation for every cycle and statistical distribution of states for a)-b) Ag/h-BN/Pt memristors and c)-d) Ag/h-BN/Ag memristors.

Additionally, when subjected to a constant voltage stress (CVS), the Ag/h-BN/Pt devices show a current that alternates between high and low levels, a behavior known as random telegraph noise (RTN). Fig. 4.16a and c show the monitored current over time of Ag/h-BN/Pt devices subjected to CVS, displaying 2-state and 3-state RTN.

It has been observed that RTN is caused by charge trapping and detrapping by individual defects, while multilevel RTN is caused by the interaction of multiple defects.[46] During these CVS measurements, as the constant voltage was applied, the devices alternated between the 2-state and 3-state RTN modes spontaneously. This coexistence of both effects can be attributed to the stochastic formation of defects within the device structure during fabrication.

The transitions between low and high current can be exploited as an entropy source by translating each transition into an output of 1 and 0, for example, by using an AC coupled amplifier.[47–50] Incidentally, the low-current baseline of either the 2-state and 3-state modes observed in our devices coincide, at approximately 10 nA (Fig. 4.16a and c), meaning that this method can be used irrespective of the current RTN mode of the device.
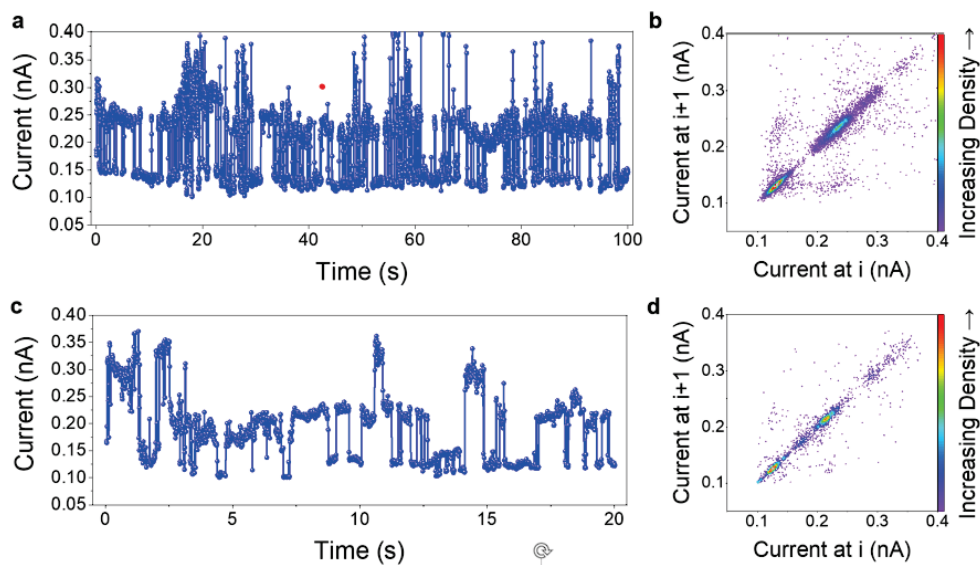
Fig. 4.16 CVS operation of Ag/h-BN/Ag memristors showing RTN between 2 states (a) and 3 states (c). The time-lag plots at b) and d) show the dispersion of the measurement of current at the current state vs that at the last measurement point.

Compared to pulsed operation, working in RTN mode consumes very low power, with currents below 1 nA, a consequence of the fact that no filament is formed and disrupted in every transition. Consequently, however, the separation between the two current levels is considerably low at approximately a factor of 2, which may add complexity to the required complementary electronics to translate the transitions into an output string of 1 and 0 values.

4.4. Supplementary tables

Table 4.1 LPE BP based memristors found in the literature.

Ref	TE/RS medium/BE	Print method	Endurance	Data points presented
Ref[51]	Al/BP/ITO	Drop-casting	-	-
Ref[52]	Al/PMMA/BPQDs/PMMA/Al	Sonication exfoliation	100	21
Ref[53]	Al/BP:PS/Al	Centrifuge	-	-

Table 4.2 LPE GO based memristors found in the literature.

Ref	TE/RS medium/BE	Print method	Endurance	Data points presented
Ref[54]	Cu/GO/Pt	Vacuum filtration	100	100
Ref[55]	Al/GO-PVK/ITO	Toluene-cast	10	9
Ref[56]	Al/G-O film/Al	Spin-casting	100	21
Ref[57]	Al/GO/ITO	Spin coating	100	50
Ref[58]	Al/TPAPAM-GO/ITO	Spin or blade coating	5	-
Ref[59]	Al/GO/ITO	Spin coating	100	50
Ref[60]	Al/RGO/ITO	Drop casting	hundreds	8
Ref[61]	Cu/GO/Pt	Vacuum filtration	-	-
Ref[62]	Pt/rGO-th/Pt	Vacuum filtration	350	350
Ref[63]	Al/FPA-rGO/ITO	Spin coating	1000	-
Ref[64]	Ag/GO/Ag	Spin coating	-	-
Ref[65]	Al/GO/ITO	Spin coating	100	100
Ref[66]	Al/GO/p-Si	Spin coating	100	50
	Al/GO/p-Ge		100	50
Ref[67]	Pt/GO/ITO	Spin coating	100	21
Ref[68]	Al/rGO/Al	Spin coating	~100	50
Ref[69]	Ag/HfO$_x$/LSG	Laser-scribing	100	-
Ref[70]	Ag/GO/ITO	Spin coating	-	-
Ref[71]	Al/CuO/GO/CuO/Al	Spray-coating	-	-
Ref[72]	Au/GO/ITO	Spin coating	100	9
Ref[73]	ITO/RGO/ITO	Dip coating	10^5	-
Ref[74]	Al/GO/Al	Spin coating	-	-
Ref[75]	Al/Au NPs-RGO-PVA/ITO	Spin casting	50	-
Ref[76]	Ag/GO/ITO	Inkjet printing	-	-
Ref[77]	ITO/GO/ITO/PES	Spin coating	-	-
Ref[78]	Al/Au NP inserted GO/ITO	Spin coating	10^4	-
Ref[79]	Ag/GO/rGO/SiO$_2$/p-Si	Spin coating	100	-

Ref		Print method	Endurance	Data points
Ref[80]	Au/GO/Au	Drip	-	-
Ref[81]	Au/GO/Al	Spin coating	200	-
Ref[79]	Ag/GO/rGO/Ag	Spin coating	100	-
Ref[82]	Ag/ZnO-rGO/FTO	Dip coating	-	-
Ref[83]	Metal/GO/Metal	Spin coating	250	15
Ref[84]	Pt/Ti/GO/Pt/Ti	Spin coating	10^4	-
Ref[85]	PEDOT:PSS/GO/PEDOT:PSS	Spin coating	10^3	-
Ref[86]	Pt/GO/ZnONR/ZnO/ITO	Drop-casting	10^3	-
Ref[80]	Au/GO/Au	Dripping	-	-
Ref[87]	Pt/brGO/Pt	Spin coating	-	-
Ref[88]	Yarns/RGO/Yarns	Spin coating	100	-
Ref[89]	Ag/N-GO QDs/Pt	Drop-casting	50	-
Ref[90]	Ag/RGO/ITO	Drop-casting	-	-
Ref[91]	Al/HGO/ITO	Spin coating	100	-
Ref[92]	Al/GO-TiO$_2$/ITO	Spin coating	60	-
Ref[93]	Pt/ZnO-G/Pt	Spin coating	-	-
Ref[94]	Ni/PMMA:GO/ITO	Spin coating	300	-
Ref[95]	Paint/GO/PET	Spin coating	100	15
Ref[96]	Al/GOAu/ITO	Spin coating	100	-
Ref[97]	LSMO-rGO	-	10^3	-
Ref[98]	Al/rGO-ZnO HC/PMMA/ITO	Spin coating	10^3	-
Ref[99]	Al/GO/Al/PES	Spin coating	100	-
Ref[78]	Al/GO/Au/GO/ITO	Spin coating	-	20

Table 4.3 LPE MoS2 based memristors found in the literature.

Ref	TE/RS medium/BE	Print method	Endurance	Data points presented
Ref[100]	Al/MoS$_2$-PVP/(rGO)	Spin coating	-	-
Ref[101]	rGO/MoS$_2$/ITO	Spin coating	-	-
Ref[102]	Ag/MoO$_x$/MoS$_2$/Ag	Inkjet, screen printing	10^4	14
Ref[103]	Al/MoS$_2$-MoO$_x$/Al	Spin coating	100	11
Ref[104]	Au/PMMA/MoS$_2$ QDs/PMMA/FTO	Spin coating	650	-
Ref[105]	Al/MoS$_2$-UCNPs/ITO	Spin coating	200	40
Ref[106]	Ag/Gr-MoS$_2$/Cu	Hydrothermal process	500	-
Ref[107]	Ag/MoS$_2$/Ag	aerosol-jet printing	120	25
Ref[108]	Gr/MoS$_2$ QDNS/Gr	Spin coating	50	-
Ref[109]	Pt/MoS$_2$/Ti	Spin coating	10^7	22

Table 4.4 LPE h-BN based memristors found in the literature.

Ref	TE/RS medium/BE	Print method	Endurance	Data points presented
Ref[110]	Ag/h-BN-PVOH/ITO	EHDA printing	1500	33
Ref[111]	Ag/ZnO/BNNSs/Pt	Spin coating	-	-
This work	Ag/h-BN/Pt	Inkjet printing	600,000	600,000
	Ag/h-BN/Ag	Inkjet printing	11,000	11,000

4.5. Overview of results regarding h-BN memristors

In *Chapter 4*, inkjet-printed h-BN memristors are presented as promising devices for random number generation and for use as physical unclonable function circuits, thanks to their inherent device-to-device variability and RTN property. The following findings are shown:

(1) The pulsed operation of h-BN memristors are shown, with the possibility to configure write pulses such that only a few devices switch from an *OFF* state to an *ON* state, which allows them to be used as PUFs.

(2) The ability of these devices to perform volatile threshold switching with exceptional endurance, reaching 0.6 million cycles when switched in pulsed, volatile unipolar mode. This is achieved by applying pulses using a current limitation of 1 µA or lower.

(3) The use of the h-BN memristors as entropy sources in one of two operation modes: pulsed operation and constant voltage operation. Strings of 1s and 0s can be generated by setting an arbitrary distinction in resistance or current level.

(4) The ability of the h-BN memristors to self-recover spontaneously from an LRS, the most common failure mode in other memristors.

REFERENCES

1. Pan, C. *et al.* Coexistence of Grain-Boundaries-Assisted Bipolar and Threshold Resistive Switching in Multilayer Hexagonal Boron Nitride. *Adv Funct Mater* **27**, (2017).

2. Ferrari, A. C. *et al.* Science and technology roadmap for graphene, related two-dimensional crystals, and hybrid systems. *Nanoscale* **7**, 4598–4810 (2015).

3. Dróżdż, P. A. *et al.* A graphene/h-BN MEMS varactor for sub-THz and THz applications. *Nanoscale* **15**, 12530–12539 (2023).

4. Schué, L. *et al.* Bright Luminescence from Indirect and Strongly Bound Excitons in h-BN. *Phys Rev Lett* **122**, 067401 (2019).

5. Dean, C. R. *et al.* Boron nitride substrates for high-quality graphene electronics. *Nat Nanotechnol* **5**, 722–726 (2010).

6. Nazir, G. *et al.* Comparison of Electrical and Photoelectrical Properties of ReS_2 Field-Effect Transistors on Different Dielectric Substrates. *ACS Appl Mater Interfaces* **10**, 32501–32509 (2018).

7. Jaiswal, H. N. *et al.* Diode-Like Selective Enhancement of Carrier Transport through Metal–Semiconductor Interface Decorated by Monolayer Boron Nitride. *Advanced Materials* **32**, (2020).

8. Lo, C.-L. *et al.* Studies of two-dimensional h-BN and MoS2 for potential diffusion barrier application in copper interconnect technology. *NPJ 2D Mater Appl* **1**, 42 (2017).

9. Wang, M. *et al.* Robust memristors based on layered two-dimensional materials. *Nat Electron* **1**, 130–136 (2018).

10. Migliato Marega, G. *et al.* Logic-in-memory based on an atomically thin semiconductor. *Nature* **587**, 72–77 (2020).

11. Bertolazzi, S. *et al.* Nonvolatile Memories Based on Graphene and Related 2D Materials. *Advanced Materials* **31**, (2019).

12. Akinwande, D. *et al.* Graphene and two-dimensional materials for silicon technology. *Nature* **573**, 507–518 (2019).

13. Mao, J. *et al.* A van der Waals Integrated Damage-Free Memristor Based on Layered 2D Hexagonal Boron Nitride. *Small* **18**, (2022).

14. Lanza, M. Hybrid 2D/CMOS microchips for memristive applications. in *2023 IEEE Nanotechnology Materials and Devices Conference (NMDC)* 192–192 (IEEE, 2023). doi:10.1109/NMDC57951.2023.10343541.

15. Zhu, K. *et al.* The development of integrated circuits based on two-dimensional materials. *Nat Electron* **4**, 775–785 (2021).

16. Hui, F. *et al.* On the use of two dimensional hexagonal boron nitride as dielectric.

Microelectron Eng **163**, 119–133 (2016).

17. Xie, J., Afshari, S. & Sanchez Esqueda, I. Hexagonal boron nitride (h-BN) memristor arrays for analog-based machine learning hardware. *NPJ 2D Mater Appl* **6**, 50 (2022).

18. Afshari, S. *et al.* Dot-product computation and logistic regression with 2D hexagonal-boron nitride (h-BN) memristor arrays. *2d Mater* **10**, 035031 (2023).

19. Yuan, B. *et al.* 150 nm × 200 nm Cross-Point Hexagonal Boron Nitride-Based Memristors. *Adv Electron Mater* **6**, (2020).

20. Wu, X. *et al.* Thinnest Nonvolatile Memory Based on Monolayer h-BN. *Advanced Materials* **31**, (2019).

21. Backes, C. *et al.* Production and processing of graphene and related materials. *2d Mater* **7**, 022001 (2020).

22. Chen, T.-A. *et al.* Wafer-scale single-crystal hexagonal boron nitride monolayers on Cu (111). *Nature* **579**, 219–223 (2020).

23. Wood, J. D. *et al.* Annealing free, clean graphene transfer using alternative polymer scaffolds. *Nanotechnology* **26**, 055302 (2015).

24. Lupina, G. *et al.* Residual Metallic Contamination of Transferred Chemical Vapor Deposited Graphene. *ACS Nano* **9**, 4776–4785 (2015).

25. Shen, Y. *et al.* Variability and Yield in h-BN-Based Memristive Circuits: The Role of Each Type of Defect. *Advanced Materials* **33**, (2021).

26. Hui, F. *et al.* Graphene and Related Materials for Resistive Random Access Memories. *Adv Electron Mater* **3**, (2017).

27. Li, J., Lemme, M. C. & Östling, M. Inkjet Printing of 2D Layered Materials. *ChemPhysChem* **15**, 3427–3434 (2014).

28. Worsley, R. *et al.* All-2D Material Inkjet-Printed Capacitors: Toward Fully Printed Integrated Circuits. *ACS Nano* **13**, 54–60 (2019).

29. Carey, T. *et al.* Fully inkjet-printed two-dimensional material field-effect heterojunctions for wearable and textile electronics. *Nature Communications* vol. 8 Preprint at https://doi.org/10.1038/s41467-017-01210-2 (2017).

30. Vescio, G. *et al.* 2D PEA 2 SnI 4 Inkjet-Printed Halide Perovskite LEDs on Rigid and Flexible Substrates. *ACS Energy Lett* **7**, 3653–3655 (2022).

31. Hossain, R. F., Deaguero, I. G., Boland, T. & Kaul, A. B. Biocompatible, large-format, inkjet printed heterostructure MoS2-graphene photodetectors on conformable substrates. *NPJ 2D Mater Appl* **1**, 28 (2017).

32. Wilk, B. *et al.* Inkjet Printing of Quasi-2D Perovskite Layers with Optimized Drying Protocol for Efficient Solar Cells. *Adv Mater Technol* **7**, (2022).

33. Lanza, M., Hui, F., Wen, C. & Ferrari, A. C. Resistive Switching Crossbar Arrays Based on Layered Materials. *Advanced Materials* **35**, (2023).

34. Chowdhury, C., Karmakar, S. & Datta, A. Capping Black Phosphorene by h-BN Enhances Performances in Anodes for Li and Na Ion Batteries. *ACS Energy Lett* **1**, 253–259 (2016).

35. Jang, S. K., Youn, J., Song, Y. J. & Lee, S. Synthesis and Characterization of Hexagonal Boron Nitride as a Gate Dielectric. *Sci Rep* **6**, 30449 (2016).

36. Zidan, M. A., Strachan, J. P. & Lu, W. D. The future of electronics based on memristive systems. *Nat Electron* **1**, 22–29 (2018).

37. Gao, B. *et al.* Concealable physically unclonable function chip with a memristor array. *Sci Adv* **8**, (2022).

38. Mispan, M. S. & Halak, B. Physical Unclonable Function: A Hardware Fingerprinting Solution. in *Authentication of Embedded Devices* 29–51 (Springer International Publishing, Cham, 2021). doi:10.1007/978-3-030-60769-2_2.

39. Vescio, G. *et al.* Inkjet-Printed Biocompatible h-BN Dielectric Ink for Flexible Electronics. in *MRS Fall Meeting, 29-4 Dec 2015* (Boston, Massachusetts, USA., 2015).

40. Vescio, G. Inkjet-Printed Flexible Electronic Devices: from High-k Capacitors to h-BN/Graphene Thin Film Transistors. (Universitat de Barcelona, 2017).

41. Zhang, C. *et al.* Controllable Co-segregation Synthesis of Wafer-Scale Hexagonal Boron Nitride Thin Films. *Advanced Materials* **26**, 1776–1781 (2014).

42. Duan, Q. *et al.* Spiking neurons with spatiotemporal dynamics and gain modulation for monolithically integrated memristive neural networks. *Nat Commun* **11**, 3399 (2020).

43. Roldan, J. B. *et al.* Spiking neural networks based on two-dimensional materials. *NPJ 2D Mater Appl* **6**, 63 (2022).

44. Lanza, M. *et al.* Standards for the Characterization of Endurance in Resistive Switching Devices. *ACS Nano* **15**, 17214–17231 (2021).

45. Wang, Z. *et al.* Memristors with diffusive dynamics as synaptic emulators for neuromorphic computing. *Nat Mater* **16**, 101–108 (2017).

46. *Noise in Nanoscale Semiconductor Devices*. (Springer International Publishing, Cham, 2020). doi:10.1007/978-3-030-37500-3.

47. Wen, C. *et al.* Data Encryption: Advanced Data Encryption using 2D Materials (Adv. Mater. 27/2021). *Advanced Materials* **33**, (2021).

48. Pazos, S. *et al.* High-Temporal-Resolution Characterization Reveals Outstanding Random Telegraph Noise and the Origin of Dielectric Breakdown in h-BN Memristors. *Adv Funct Mater* (2023) doi:10.1002/adfm.202213816.

49.   Pazos, S. *et al.* Hardware implementation of a true random number generator integrating a hexagonal boron nitride memristor with a commercial microcontroller. *Nanoscale* **15**, 2171–2180 (2023).

50.   Li, X. *et al.* Random Telegraph Noise in Metal-Oxide Memristors for True Random Number Generators: A Materials Study. *Adv Funct Mater* **31**, (2021).

51.   Hao, C. *et al.* Liquid-Exfoliated Black Phosphorous Nanosheet Thin Films for Flexible Resistive Random Access Memory Applications. *Adv Funct Mater* **26**, 2016–2024 (2016).

52.   Han, S. *et al.* Black Phosphorus Quantum Dots with Tunable Memory Properties and Multilevel Resistive Switching Characteristics. *Advanced Science* **4**, (2017).

53.   Hsieh, Y.-L., Su, W.-H., Huang, C.-C. & Su, C.-Y. Solution-processed black phosphorus nanoflakes for integrating nonvolatile resistive random access memory and the mechanism unveiled. *Nanotechnology* **30**, 445702 (2019).

54.   He, C. L. *et al.* Nonvolatile resistive switching in graphene oxide thin films. *Appl Phys Lett* **95**, (2009).

55.   Liu, G. *et al.* Bistable electrical switching and electronic memory effect in a solution-processable graphene oxide-donor polymer complex. *Appl Phys Lett* **95**, (2009).

56.   Jeong, H. Y. *et al.* Graphene Oxide Thin Films for Flexible Nonvolatile Memory Applications. *Nano Lett* **10**, 4381–4386 (2010).

57.   Seul Ki Hong, Ji Eun Kim, Sang Ouk Kim, Sung-Yool Choi & Byung Jin Cho. Flexible Resistive Switching Memory Device Based on Graphene Oxide. *IEEE Electron Device Letters* **31**, 1005–1007 (2010).

58.   Lai, Y.-C. *et al.* Low operation voltage macromolecular composite memory assisted by graphene nanoflakes. *J. Mater. Chem. C* **1**, 552–559 (2013).

59.   Ki Hong, S., Eun Kim, J., Kim, S. O. & Jin Cho, B. Analysis on switching mechanism of graphene oxide resistive memory device. *J Appl Phys* **110**, (2011).

60.   Vasu, K. S., Sampath, S. & Sood, A. K. Nonvolatile unipolar resistive switching in ultrathin films of graphene and carbon nanotubes. *Solid State Commun* **151**, 1084–1087 (2011).

61.   Zhuge, F. *et al.* Mechanism of nonvolatile resistive switching in graphene oxide thin films. *Carbon N Y* **49**, 3796–3802 (2011).

62.   Hu, B. *et al.* Electrically controlled electron transfer and resistance switching in reduced graphene oxide noncovalently functionalized with thionine. *J Mater Chem* **22**, 16422 (2012).

63.   Jin, C., Lee, J., Lee, E., Hwang, E. & Lee, H. Nonvolatile resistive memory of ferrocene covalently bonded to reduced graphene oxide. *Chemical Communications* **48**, 4235 (2012).

64. Venugopal, G. & Kim, S.-J. Observation of Nonvolatile Resistive Memory Switching Characteristics in Ag/Graphene-Oxide/Ag Devices. *J Nanosci Nanotechnol* **12**, 8522–8525 (2012).

65. Wang, L.-H. *et al.* The mechanism of the asymmetric SET and RESET speed of graphene oxide based flexible resistive switching memories. *Appl Phys Lett* **100**, (2012).

66. Jilani, S. M., Gamot, T. D., Banerji, P. & Chakraborty, S. Studies on resistive switching characteristics of aluminum/graphene oxide/semiconductor nonvolatile memory cells. *Carbon N Y* **64**, 187–196 (2013).

67. Khurana, G., Misra, P. & Katiyar, R. S. Forming free resistive switching in graphene oxide thin film for thermally stable nonvolatile memory applications. *J Appl Phys* **114**, (2013).

68. Ho, N. T., Senthilkumar, V. & Kim, Y. S. Impedance spectroscopy analysis of the switching mechanism of reduced graphene oxide resistive switching memory. *Solid State Electron* **94**, 61–65 (2014).

69. Tian, H. *et al.* Cost-Effective, Transfer-Free, Flexible Resistive Random Access Memory Using Laser-Scribed Reduced Graphene Oxide Patterning Technology. *Nano Lett* **14**, 3214–3219 (2014).

70. Yi, M. *et al.* Temperature dependence of resistive switching behaviors in resistive random access memory based on graphene oxide film. *Nanotechnology* **25**, 185202 (2014).

71. Yoo, D.-H., Cuong, T. V. & Hahn, S. H. Effect of copper oxide on the resistive switching responses of graphene oxide film. *Current Applied Physics* **14**, 1301–1303 (2014).

72. Banerjee, I., Harris, P., Salimian, A. & Ray, A. K. Graphene oxide thin films for resistive memory switches. *IET Circuits, Devices & Systems* **9**, 428–433 (2015).

73. Kim, H.-D., Yun, M. J., Lee, J. H., Kim, K. H. & Kim, T. G. Transparent Multi-level Resistive Switching Phenomena Observed in ITO/RGO/ITO Memory Cells by the Sol-Gel Dip-Coating Method. *Sci Rep* **4**, 4614 (2014).

74. Kim, S. K., Kim, J. Y., Choi, S., Lee, J. Y. & Jeong, H. Y. Direct Observation of Conducting Nanofilaments in Graphene-Oxide-Resistive Switching Memory. *Adv Funct Mater* **25**, 6710–6715 (2015).

75. Midya, A., Gogurla, N. & Ray, S. K. Flexible and transparent resistive switching devices using Au nanoparticles decorated reduced graphene oxide in polyvinyl alcohol matrix. *Current Applied Physics* **15**, 706–710 (2015).

76. Porro, S. & Ricciardi, C. Memristive behaviour in inkjet printed graphene oxide thin layers. *RSC Adv* **5**, 68565–68570 (2015).

77. Wu, H.-Y., Lin, C.-C. & Lin, C.-H. Characteristics of graphene-oxide-based flexible and transparent resistive switching memory. *Ceram Int* **41**, S823–S828 (2015).

78. Yun, D. Y. & Kim, T. W. Nonvolatile memory devices based on Au/graphene oxide nanocomposites with bilateral multilevel characteristics. *Carbon N Y* **88**, 26–32 (2015).

79. Hazra, P., Resmi, A. N. & Jinesh, K. B. Gate controllable resistive random access memory devices using reduced graphene oxide. *Appl Phys Lett* **108**, (2016).

80. Wang, L. *et al.* Neuromorphic Computing: Controllable Multiple Depression in a Graphene Oxide Artificial Synapse (Adv. Electron. Mater. 1/2017). *Adv Electron Mater* **3**, (2017).

81. Kim, S. K. *et al.* Conductive Graphitic Channel in Graphene Oxide-Based Memristive Devices. *Adv Funct Mater* **26**, 7406–7414 (2016).

82. Khanal, G. M. *et al.* A ZnO-rGO composite thin film discrete memristor. in *2016 IEEE International Conference on Semiconductor Electronics (ICSE)* 129–132 (IEEE, 2016). doi:10.1109/SMELEC.2016.7573608.

83. Pradhan, S. K., Xiao, B., Mishra, S., Killam, A. & Pradhan, A. K. Resistive switching behavior of reduced graphene oxide memory cells for low power nonvolatile device application. *Sci Rep* **6**, 26763 (2016).

84. Nagareddy, V. K. *et al.* Multilevel Ultrafast Flexible Nanoscale Nonvolatile Hybrid Graphene Oxide–Titanium Oxide Memories. *ACS Nano* **11**, 3010–3021 (2017).

85. Shi, R. *et al.* Fully Solution-Processed Transparent Nonvolatile and Volatile Multifunctional Memory Devices from Conductive Polymer and Graphene Oxide. *Adv Electron Mater* **3**, (2017).

86. Anoop, G., Panwar, V., Kim, T. Y. & Jo, J. Y. Resistive Switching in ZnO Nanorods/Graphene Oxide Hybrid Multilayer Structures. *Adv Electron Mater* **3**, (2017).

87. Kim, S. *et al.* In Situ Observation of Resistive Switching in an Asymmetric Graphene Oxide Bilayer Structure. *ACS Nano* **12**, 7335–7342 (2018).

88. Park, Y., Park, M. & Lee, J. Reduced Graphene Oxide-Based Artificial Synapse Yarns for Wearable Textile Device Applications. *Adv Funct Mater* **28**, (2018).

89. Sokolov, A. S. *et al.* Silver-Adapted Diffusive Memristor Based on Organic Nitrogen-Doped Graphene Oxide Quantum Dots (N-GOQDs) for Artificial Biosynapse Applications. *Adv Funct Mater* **29**, (2019).

90. Vartak, R., Rag, A., De, S. & Bhat, S. Study of Ag/RGO/ITO sandwich structure for resistive switching behavior deposited on plastic substrate. *Appl Nanosci* **8**, 1343–1351 (2018).

91. Jesuraj, P. J., Parameshwari, R. & Jeganathan, K. Improved performance of graphene oxide based resistive memory devices through hydrogen plasma. *Mater Lett* **232**, 62–65 (2018).

92. Singh, R., Kumar, R., Kumar, A., Kumar, D. & Kumar, M. Enhanced resistive switching

in graphene oxide based composite thin film for nonvolatile memory applications. *Mater Res Express* **6**, 105621 (2019).

93.   Aziz, T. N. T. A., Rosli, A. B., Yusoff, M. M., Herman, S. H. & Zulkifli, Z. Transparent hybrid ZnO-graphene film for high stability switching behavior of memristor device. *Mater Sci Semicond Process* **89**, 68–76 (2019).

94.   Li, L. Tunable Memristic Characteristics Based on Graphene Oxide Charge-Trap Memory. *Micromachines (Basel)* **10**, 151 (2019).

95.   Romero *et al.* Laser-Fabricated Reduced Graphene Oxide Memristors. *Nanomaterials* **9**, 897 (2019).

96.   Khurana, G., Kumar, N., Chhowalla, M., Scott, J. F. & Katiyar, R. S. Non-Polar and Complementary Resistive Switching Characteristics in Graphene Oxide devices with Gold Nanoparticles: Diverse Approach for Device Fabrication. *Sci Rep* **9**, 15103 (2019).

97.   Kumari, K. *et al.* Structural and resistive switching behaviour in lanthanum strontium manganite - Reduced graphene oxide nanocomposite system. *J Alloys Compd* **815**, 152213 (2020).

98.   Gogoi, K. K. & Chowdhury, A. Performance Enhancement of Solution-Processed Organic Memories by Exploiting Synergistic Organic–Inorganic Hybrid Composites. *The Journal of Physical Chemistry C* **124**, 1108–1120 (2020).

99.   Tan, C., Liu, Z., Huang, W. & Zhang, H. Non-volatile resistive memory devices based on solution-processed ultrathin two-dimensional nanomaterials. *Chem Soc Rev* **44**, 2615–2628 (2015).

100. Liu, J. *et al.* Preparation of MoS 2 -Polyvinylpyrrolidone Nanocomposites for Flexible Nonvolatile Rewritable Memory Devices with Reduced Graphene Oxide Electrodes. *Small* **8**, 3517–3522 (2012).

101. Xu, X.-Y., Yin, Z.-Y., Xu, C.-X., Dai, J. & Hu, J.-G. Resistive switching memories in MoS2 nanosphere assemblies. *Appl Phys Lett* **104**, (2014).

102. Bessonov, A. A. *et al.* Layered memristive and memcapacitive switches for printable electronics. *Nat Mater* **14**, 199–204 (2015).

103. Son, D. *et al.* Colloidal Synthesis of Uniform-Sized Molybdenum Disulfide Nanosheets for Wafer-Scale Flexible Nonvolatile Memory. *Advanced Materials* **28**, 9326–9332 (2016).

104. Wang, D. *et al.* Quantum conductance in MoS2 quantum dots-based nonvolatile resistive memory device. *Appl Phys Lett* **110**, (2017).

105. Zhai, Y. *et al.* Photonic Memory: Infrared-Sensitive Memory Based on Direct-Grown MoS 2 –Upconversion-Nanoparticle Heterostructure (Adv. Mater. 49/2018). *Advanced Materials* **30**, (2018).

106. Yalagala, B., Sahatiya, P., Mattela, V. & Badhulika, S. Ultra-low Cost, Large Area Graphene/MoS 2 -Based Piezotronic Memristor on Paper: A Systematic Study for Both Direct Current and Alternating Current Inputs. *ACS Appl Electron Mater* **1**, 883–891 (2019).

107. Feng, X. *et al.* Neuromorphic Computing: A Fully Printed Flexible MoS 2 Memristive Artificial Synapse with Femtojoule Switching Energy (Adv. Electron. Mater. 12/2019). *Adv Electron Mater* **5**, (2019).

108. Fu, X. *et al.* Molybdenum Disulfide Nanosheet/Quantum Dot Dynamic Memristive Structure Driven by Photoinduced Phase Transition. *Small* **15**, (2019).

109. Tang, B. *et al.* Wafer-scale solution-processed 2D material analog resistive memory array for memory-based computing. *Nat Commun* **13**, 3037 (2022).

110. Siddiqui, G. U., Rehman, M. M., Yang, Y.-J. & Choi, K. H. A two-dimensional hexagonal boron nitride/polymer nanocomposite for flexible resistive switching devices. *J Mater Chem C Mater* **5**, 862–871 (2017).

111. Wang, G., Yan, X., Chen, J. & Ren, D. Memristors Based on the Hybrid Structure of Oxide and Boron Nitride Nanosheets Combining Memristive and Neuromorphic Functionalities. *physica status solidi (RRL) – Rapid Research Letters* **14**, (2020).

Chapter 5

Inkjet-Printed p-NiO/n-ZnO Heterojunction Diodes for Photodetection Applications

In this chapter, inkjet-printed NiO/ZnO photodetectors will be fabricated and studied. The main contribution of this section is the validation of low post processing temperature inkjet printable, metal oxide transport layer materials and the fabrication process to obtain thin films through the fabrication of inkjet-printed metal oxide photodetectors.

The varied requirements across different application fields of photodetection result in several device families are available for UV photodetection, such as charge coupled devices (CCD), photomultiplier tubes (PMT), and semiconductor photodetectors.[1] Although semiconductor photodetectors are a versatile choice for most UV photodetection applications, thanks to their compact form factor (compared to PMTs) and fast response (compared to CCD), commercial devices are generally based on narrow-bandgap semiconductors such as Si, requiring filters to suppress visible light[2] and suffering degradation due to exposure to photons of much higher energy than the bandgap, besides lacking mechanical flexibility.[3] More recent research has studied large-bandgap materials such as SiC or III-Nitride compounds such as GaN for photodetection, however they require complex manufacturing processes and are difficult to prepare in large area substrates.[4,5] Thus, metal oxides, in particular p-type NiO and n-type-ZnO, are proposed as an alternative material due to their solution processability, mechanical flexibility,[6] compatibility with large-are processing,[7,8] optical transparency, and abundance,[6,9,10] in the form of inkjet-printable nanoparticle inks. Although previous studies have demonstrated the compatibility of NiO with ZnO for optoelectronics, they have generally focused on non-solution processing technologies such as CVD and sputtering. [11–18]

This study reports on the IJP fabrication and characterization of a transparent, inorganic conductive NiO/ZnO heterojunction photodetector post-processed at a temperature of 200 °C, compatible with different flexible substrates. An initial characterization of morphology, chemical structure and optical properties of the p-type NiO and n-type ZnO inks by SEM, XRD, and optical spectroscopy is followed by the

fabrication of a heterojunction device with an Au/NiO/ZnO/C structure onto a Si/SiO2 wafer. The intensity-voltage characterization of the device is performed in dark and illuminated condition, showing its photoresponse.

The work showcased here is intended as a first step characterization towards the application of these inks in the fully-inkjet-printed perovskite LEDs (PeLEDs) that will be presented in **Chapter 6**. The low post-processing temperature is a crucial parameter for two main reasons. First, because during the post-processing of the top layers of the PeLED, the active (perovskite) layer will be exposed to the same process as well, low temperature post-processing is a requirement for fully inkjet fabrication of PeLEDs. We have found the mark of 200 ºC to be the upper allowable boundary for stress on $CsPbBr_3$ nanocrystalss, beyond which they suffer considerable degradation. Secondly, it allows for the printing and further processing on flexible substrates, which have stricter post-processing restrictions than solid substrates, an imperative when considering large scale, commercial R2R manufacturing of devices.

5.1. Inkjet-printed NiO and ZnO thin films

5.1.1. Morphological and crystalline analysis of the NiO and ZnO thin films

A preliminary characterization of the inkjet-printed NiO and ZnO inks is performed (inks acquired from *Avantama AG*). These inks are a suspension of metal oxide nanoparticles synthesized by flame spray pyrolysis by *Avantama AG*, with hydrodynamic particle sizes of 7 nm (NiO) and 12 nm (ZnO) reported as fabricated. Dispersed in hexanol as the main carrier, a non-disclosed proprietary additive blend ensures a stable ink solution. Details regarding ink formulation are presented in **Chapter 3**.

For SEM characterization, single layers of these materials are inkjet-printed on Si/SiO_2 substrates and then subjected to a thermal post-processing both in ambient condition and in vacuum, at a temperature of 200 °C for 1h. Vacuum curing is introduced to enhance the curing process, as it is expected to improve the removal solvents thanks to the reduced pressure. In addition, the layers are expected to have lowered contamination from atmospheric contaminants. [19,20]

Upon first inspection, the inkjet-printed NiO layer cured under atmospheric

conditions appears hazy in SEM imaging. This is a phenomenon sometimes observed in solution processed layers that have undergone incomplete drying of their solvents (Fig. 5.1a).[21] Conversely, once the NiO layers that underwent post-treatment in vacuum are analyzed, their morphology can be distinguished, showing a granular surface, which suggests enhanced solvent removal (Fig. 5.1b).

Similarly, the non-vacuum post-processed inkjet-printed ZnO thin films show an undesirable appearance. SEM images reveal dark patches throughout the layer (Fig. 5.1c), suggesting boiling of the ink solvents. These features may lead to shunt (parasitic) currents across the layer in a device structure. However, when the inkjet-printed layers are post-processed under a vacuum procedure, a layer without visible pinholes is obtained (Fig. 5.1d).
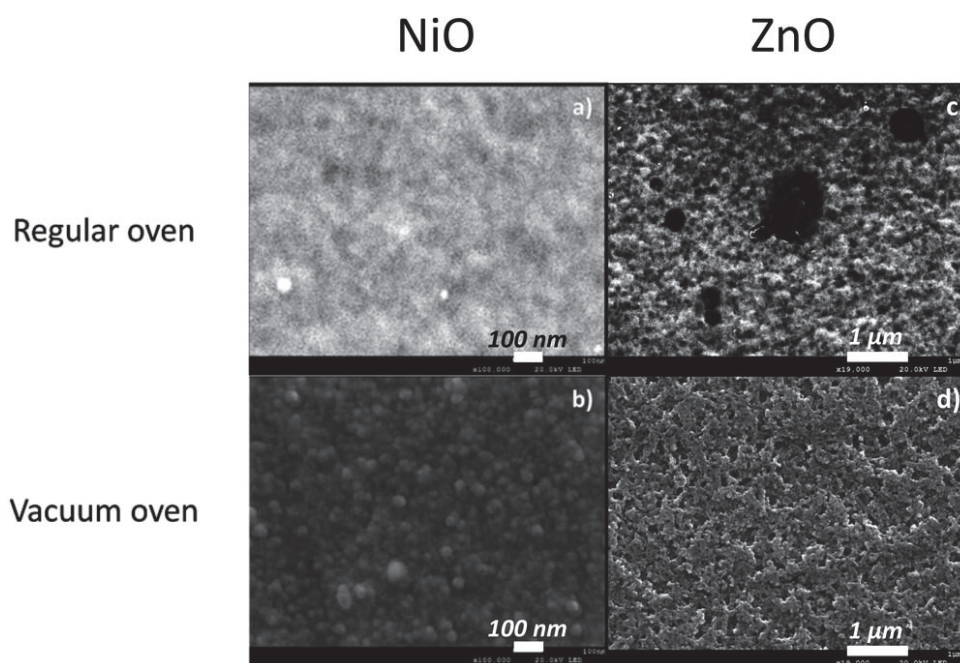
Fig. 5.1 Comparison of SEM images of regular convection oven and vacuum oven thermal post-treatment for NiO and ZnO layers, showing an improvement in layer quality for the vacuum oven treated layers.

A close view SEM of the vacuum post-processed NiO and ZnO layers is shown in Fig. 5.2. While some granularity can be perceived, expected from a nanoparticle-based thin film, these images reveal uniform and compact layers, a crucial aspect for thin film device fabrication. The approximate grain size of the thin films can be estimated at 30–

50 nm for ZnO and around 30 nm for NiO, greater than the original particles in solution, hinting at a successful sintering process.
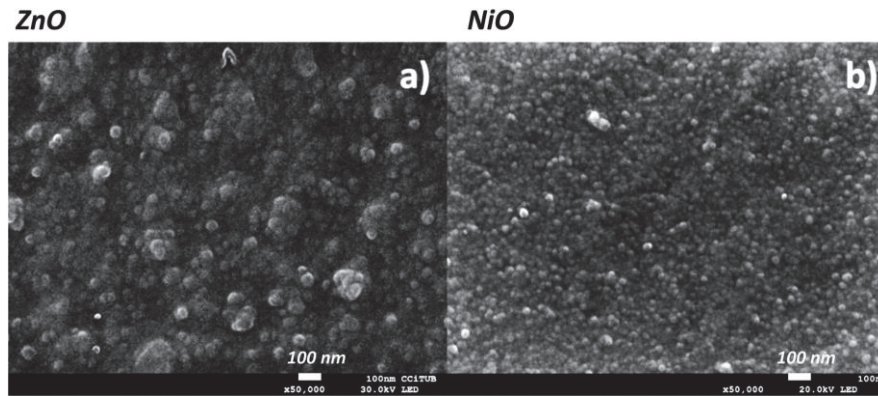
Fig. 5.2 Planar view SEM of inkjet-printed (a) ZnO and (b) NiO layers post-treated in vacuum.

Following the morphological SEM analysis, the metal oxide thin films are studied by XRD, shown in Fig. 5.3, which displays the observed peaks in the diffraction pattern. Zinc oxide (ZnO) can be found in three distinct structures: rock-salt, zinc-blende, and wurtzite, the latter being the only one stable under standard temperature and pressure. In contrast, rock-salt appears at high pressure, whereas obtaining zinc-blende ZnO requires epitaxy on a cubic substrate.[22] As expected, the diffraction pattern of ZnO (Fig. 5.3a) corresponds to its wurtzite crystal structure in the hexagonal system.[23,24] For NiO, the peaks detected (Fig. 5.3b) reveal its cubic phase, in agreement with the literature.[25]
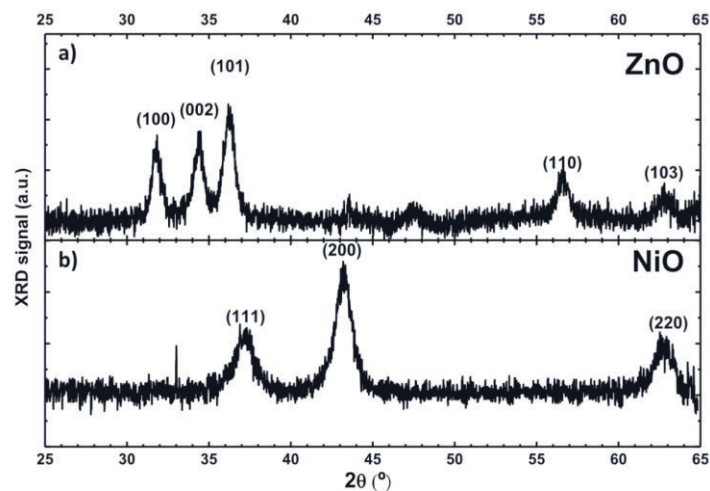
Fig. 5.3 XRD pattern of inkjet-printed (a) ZnO and (b) NiO thin films, showing peaks expected for wurtzite structure (ZnO) and cubic phase (NiO).

By measuring the full width half maximum of the XRD peaks of NiO and ZnO, the

respective crystallite sizes of each can be estimated through the Debye-Scherrer equation (eq. 5.1).

$$\tau = \frac{K\lambda}{\beta \cos(\theta)}$$ (eq. 5.1)

where the wavelength of the X-ray radiation is $\lambda = 0.15406$ nm is, β is the FWHM and θ is the measured diffraction angle. Following this equation, the estimated crystallite size is 13 nm for the ZnO layer and 9 nm for the NiO layer, in agreement with the values of nanoparticle size in suspension reported by *Avantama AG* for these inks, 12 nm and 7 nm, respectively. The findings from FESEM analysis and XRD data suggest that the nanoparticles underwent sintering but not recrystallization into a distinct phase, unlike what may be observed in other established deposition methods such atomic layer deposition or CVD.[26,27]

5.1.2. Optical Properties

After morphological and structural analysis of the inkjet-printed metal oxide layers, optical characterization was performed. Films of NiO and ZnO were printed onto fused silica, as it provides more accurate UV-VIS spectroscopy characterization thanks to its superior UV transparency compared to standard glass (Fig. 5.4a and b). In addition, layers of NiO and ZnO were inkjet-printed on PET, validating their excellent flexible substrate processability. The pictures in Fig. 5.4c–e are a close-up of 1×1 cm^2 films of inkjet-printed NiO and ZnO on PET, presenting a uniform appearance despite the moderately sized area of the layers. Fig. 5.4d-e shows pictures of the NiO and ZnO printed layers shone with light and photographed at a low exposure level to reveal the surface in detail through reflected light. The color observed in the printed areas is a result of light that has undergone reflection and thin film interference, providing qualitative insight into the thickness of the inkjet-printed thin films. A thickening effect can be seen along the periphery of the inkjet-printed ZnO (Fig. 5.4d), a widely reported occurrence in inkjet-printed layers referred commonly to as the coffee-ring effect.[28] Despite the undesirable nature of this effect, it can be seen that this phenomenon is limited to the edge zone, while the rest of the deposited surface maintains a uniform thickness. The NiO layer (Fig. 5.4e)

shows a similar effect, although less markedly.
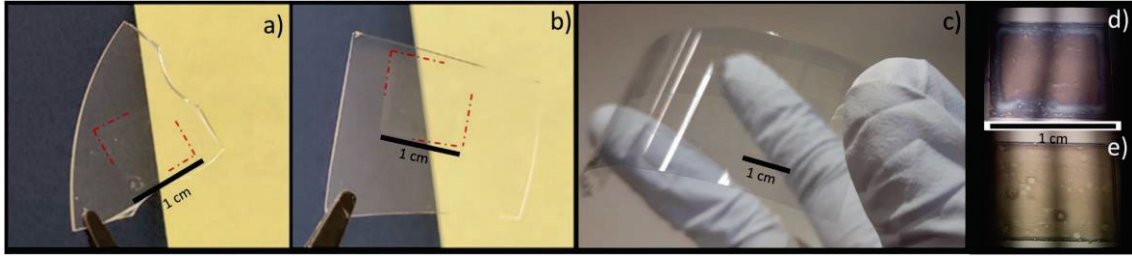
Fig. 5.4 Detail photographs of (a) ZnO and (b) NiO inkjet-printed on fused silica. (c) Both materials printed on PET, and close-up in (d) ZnO and (e) NiO.

In order to be incorporated in an optoelectronic device structure, the transparency of NiO and ZnO is paramount. However, light absorption in the layer along with the reflection caused by the significant difference in refractive indices between air and the metal oxide material, set a constraint on the maximum optical transparency (T_{max}) of the thin film. The contrast in refractive indices (n) cause a reflectivity that can be calculated as (eq. 5.2):

$$R_{n2-n1} = \frac{n_2 - n_1}{n_2 + n_1}^2$$ (eq. 5.2)

T_{max} is easily obtained by assuming no absorption (eq. 5.3):

$$T_{max} = 1 - R_{n2-n1}$$ (eq. 5.3)

Using the values $n_{ZnO} = 2.018$,[29] and $n_{NiO} = 2.180$,[30] at a wavelength of 500 nm, the values of $T_{max\ ZnO} = 88.6\%$ and $T_{max\ NiO} = 86.2\%$ are obtained. Fig. 5.5 shows the optical spectrum of the inkjet-printed NiO and ZnO layers. Excellent transmittances, with NiO reaching above 90% (Fig. 5.5a) and ZnO 70% (Fig. 5.5b) in the visible range, are obtained within the expected range of T_{max}. The spectrum observed for ZnO shows a sudden dip in transmittance due to its band gap of ~3.3 eV (corresponding to a photon wavelength of 375 nm).

Furthermore, the band-gap energy of direct band-gap materials can be estimated using a Tauc plot representation. This involves using the following relation (eq. 5.4).

$$(\alpha \cdot h \cdot v) \propto (h \cdot v - E_g)$$ (eq. 5.4)

where hv represents the photon energy and α is the absorption coefficient. The graph in Fig. 5.5c displays a plot of these relations, where the linear regression on this curve yielding an approximate value for the optical bandgap of the inkjet-printed ZnO layer at around 3.28 eV (corresponding to a photon wavelength of 378 nm). This is consistent with the published literature, indicating that the optical characteristics of the ZnO thin films are not altered by the inkjet printing process. In contrast, the bandgap of NiO, known to be around 3.7 eV (335 nm), lies is beyond the measurement range of the spectroscopy setup used (λ > 350 nm), and thus could not be estimated using this method.[31]
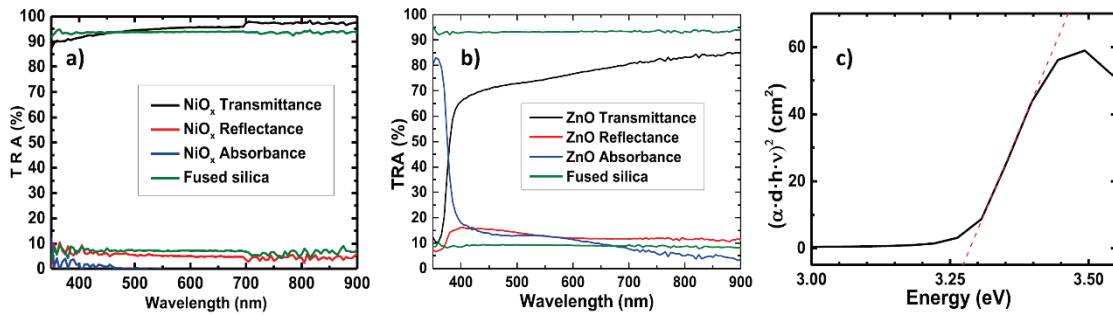
Fig. 5.5. Optical spectrosccopy of (a) NiO and (b) ZnO. (c) Estimation of the bandgap energy of ZnO by Tauc plot regression method.

In order to compare these results with the published literature irrespective of layer thickness, the coefficient of absorbance of the layers is estimated. While the absorbance of the inkjet-printed layers presented here can be easily calculated from the values of reflectance and transmittance (A = 1 - R - T), most articles only cite transmittance values, thus accurately determining the coefficient of absorptance for thin films is challenging. Due to this limitation, the exponential law of absorption (eq. 5.5) was used, to determine the coefficient of absorption assuming no reflectance (eq. 5.6).

$$T = e^{-\alpha t} \tag{eq. 5.5}$$

$$\alpha = -\frac{1}{t} \ln{(T)} \tag{eq. 5.6}$$

Table 5.1 compares the optical properties of the inkjet-printed thin films obtained here with the existing literature, which were fabricated using more established deposition technologies. It can be seen that the absorption coefficients obtained for the inkjet-printed

NiO and ZnO layers are similar to those reported in the literature.

Table 5.1 Optical properties of similar NiO and ZnO layers published in the literature.

Ref.	Material	Method	Thickness [nm]	Transmittance range [%] [400–600 nm]	Coeff. Abs Range [1/µm] [400–600 nm]
This work	NiO	Inkjet	200	90 - 95	0.53 - 0.26
Ref[16]	NiO	Spin coating	40	87 - 95	1.94 - 0.40
Ref[12]	NiO	Epitaxy	50	97 - 98	0.61 - 0.40
Ref[32]	NiO	Chemical bath deposition	120	88 - 88	1.07 - 1.07
Ref[33]	NiO	Spin coating	150	88 - 92	0.85 - 0.56
This work	ZnO	Inkjet	200	65 - 80	2.15 - 1.12
Ref[34]	ZnO	Spin coating	100	67 - 90	4.00 - 1.05
Ref[35]	ZnO	Sol-gel	200	85 - 90	0.81 - 0.53
Ref[36]	ZnO	Ultrasonic spray pyrolysis	200	80 - 92	1.12 - 0.42
Ref[37]	ZnO	Spin coating	150	88 - 92	0.85 - 0.56

5.2. Inkjet-printed diode I-V characteristic and photodetection

After evaluating the ink printing and post-processing method, the NiO and ZnO inks were used to fabricate an Au/NiO/ZnO/C inkjet-printed heterojunction. Fig. 5.6a-c illustrates the fabricated device architecture, its equilibrium band structure as expected from literature, and a top view image of the finished devices, respectively. Gold is chosen as a back contact as its work function should create an ohmic contact with NiO, and ensure a proper interface as a noble metal.[38] Regarding the top contacts, inkjet-printed Ag nanoparticle contacts as those shown for h-BN devices were attempted, however these devices showed shunted behavior evidenced by low resistances and linear I-V characteristics. Suspecting undesirable Ag^+ electromigration, a commercial carbon paste was applied by a simple screen-printing process as an alternative. The active device area is delimited by the top carbon contacts, which have a radius of 100 micrometers.
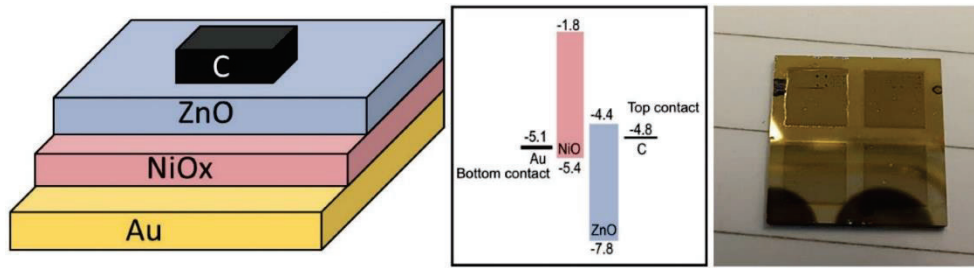
Fig. 5.6 (a) Sketch of structure of Au/NiO/ZnO/C device, and (b) its band diagram. c) Photograph of the finished heterojunctions on Au-covered Si/SiO$_2$ substrate.

To investigate the electrical behavior of the inkjet-printed NiO/ZnO heterojunction, the current-voltage (I-V) characteristics of a device was examined under dark conditions (Fig. 5.7a). The heterojunction exhibits remarkable current rectification behavior, demonstrating a significant forward/reverse polarization current ratio of two orders of magnitude at a voltage of ± 3 V, with a threshold voltage of around 2.2 V. The rectification behavior of the Au/NiO/ZnO/C heterojunction is compared with that of similar devices in the literature, deposited using more consolidated processes, as shown in Table 5.2.

Following, the inkjet-printed Au/NiO/ZnO/C device was analyzed to determine its photoresponse. This was done by measuring its I-V characteristics under exposure to light from an AM1.5 Global solar simulator. The current-voltage (I-V) behavior of the device in dark and under illumination is compared in Fig. 5.7b. The graph is plotted using a semi-log scale, with the current intensity represented in absolute value, revealing a remarkable quotient of $I_{light}/I_{dark} = 10^4$ at reverse polarization under the solar simulator.
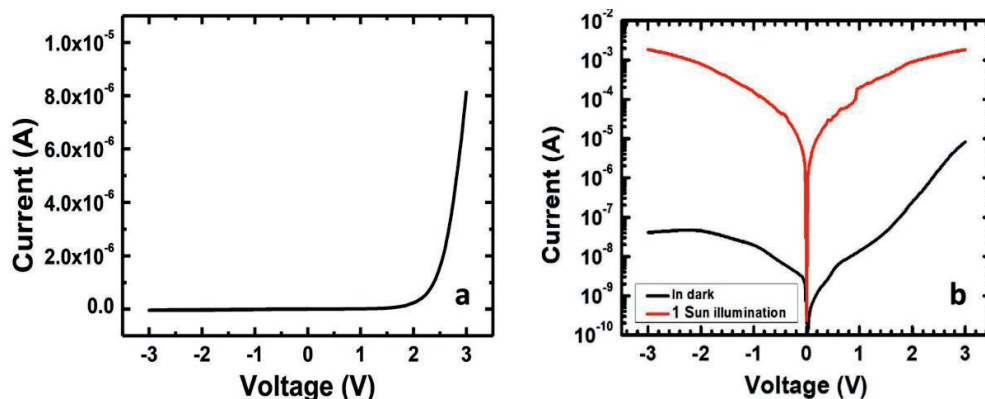
Fig. 5.7 (a) Rectification behavior of the device with no illumination. (b) I–V curves of the Au/ NiO / ZnO/ C heterojunction in dark and illuminated conditions.

Table 5.2 Summary of similar diodes published in the literature, showing their rectification behavior.

Ref.	Structure	Device	Deposition method	$\log_{10}[I_+/I_-]$	measured @voltage [V]
This work	Au/NiO/ZnO/C	UV photodetector	Inkjet printing	0.8	2
Ref[39]	ITO/NiOx/ZnO/Al	UV photodetector	Spin coating	2.46	1
Ref[40]	ITO/NiOx/ZnO/Al	UV photodetector	Spin coating	2.05	5
Ref	Au/NiOx/ZnO/Au	UV photodetector	RF magnetron sputtering	3.81	2
Ref[41]	ITO/ZnO/NiO/Ni	UV photodetector	Sputtering (ZnO) + ion beam (NiOx)	3.6	2
Ref[42]	ITO/NiO/ZnO/Au	UV photodetector	PLD (ZnO) + solid phase epitaxy (NiO)	2.36	2
Ref[43]	ITO/In$_2$O$_3$/NiO /PEDOT:PSS	Diode	Inkjet printing	1.04	2

5.3. Overview of results regarding inkjet-printed p-NiO/n-ZnO photodetectors

In *Chapter 5*, inkjet-printed p-NiO and n-ZnO layers are presented, and photodetectors based them studied. The following contributions were shown:

(1) The inkjet printing manufacturing of transparent thin films of n-type ZnO and p-type NiO showcased on rigid and flexible substrates, demonstrating optimal printability on a variety of surfaces.

(2) Thorough investigation of these layers through XRD shows their material properties are maintained. SEM imaging proves the thin layer surface is homogeneous and free of imperfections such as wrinkles, cracks, and pinholes, which would limit their applicability to optoelectronic devices.

(3) The observation of rectification behavior in a device structure, further demonstrating the semiconducting properties of the layers. This is a key point, as these layers are being studied for their future use in PeLED structures. A rectification ratio of 10^2 is observed between -/+ 3 V.

(4) The demonstration of photodetection properties of these layers, pointing to an appropriate interface between the layers, a crucial aspect towards the manufacturing of PeLEDs.

REFERENCES

1. Jandow, N. N., Abu, H., Yam, F. K. & Ibrahim, K. ZnO Metal-Semiconductor-Metal UV Photodetectors on PPC Plastic with Various Metal Contacts. in *Photodetectors* (InTech, 2012). doi:10.5772/37963.

2. Liu, K., Sakurai, M. & Aono, M. ZnO-Based Ultraviolet Photodetectors. *Sensors* **10**, 8604–8634 (2010).

3. Liu, S. *et al.* Tunable Hybrid Photodetectors with Superhigh Responsivity. *Small* **5**, 2371–2376 (2009).

4. Hu, J. *et al.* Research advances in ZnO nanomaterials-based UV photode tectors: a review. *Nanotechnology* **34**, 232002 (2023).

5. Ye, Q. *et al.* Research and Progress of Transparent, Flexible Tin Oxide Ultraviolet Photodetector. *Crystals (Basel)* **11**, 1479 (2021).

6. Yu, X., Marks, T. J. & Facchetti, A. Metal oxides for optoelectronic applications. *Nat Mater* **15**, 383–396 (2016).

7. Look, D. C. Recent advances in ZnO materials and devices. *Materials Science and Engineering: B* **80**, 383–387 (2001).

8. Tsukazaki, A. *et al.* Repeated temperature modulation epitaxy for p-type doping and light-emitting diode based on ZnO. *Nat Mater* **4**, 42–46 (2005).

9. Kim, Y.-H. *et al.* Flexible metal-oxide devices made by room-temperature photochemical activation of sol–gel films. *Nature* **489**, 128–132 (2012).

10. Chavali, M. S. & Nikolova, M. P. Metal oxide nanoparticles and their applications in nanotechnology. *SN Appl Sci* **1**, 607 (2019).

11. Zhao, Y. *et al.* Study on the electroluminescence properties of diodes based on n-ZnO/p-NiO/p-Si heterojunction. *Opt Commun* **336**, 1–4 (2015).

12. Zhai, P. *et al.* Transparent p-type epitaxial thin films of nickel oxide. *Chemical Communications* **50**, 1854–1856 (2014).

13. Ahmed, A. A., Devarajan, M. & Afzal, N. Fabrication and characterization of high performance MSM UV photodetector based on NiO film. *Sens Actuators A Phys* **262**, 78–86 (2017).

14. Chen, R. & Lan, L. Solution-processed metal-oxide thin-film transistors: a review of recent developments. *Nanotechnology* **30**, 312001 (2019).

15. You, J. *et al.* Improved air stability of perovskite solar cells via solution-processed metal oxide transport layers. *Nat Nanotechnol* **11**, 75–81 (2016).

16. Liu, S. *et al.* Nickel Oxide Hole Injection/Transport Layers for Efficient Solution-Processed Organic Light-Emitting Diodes. *Chemistry of Materials* **26**, 4528–4534 (2014).

17. Chen, T. F. *et al.* Property modulation of NiO films grown by radio frequency magnetron sputtering. *J Alloys Compd* **643**, 167–173 (2015).

18. Zhang, T., Li, L. & Ao, J. P. Temperature-dependent electrical transport characteristics of a NiO/GaN heterojunction diode. *Surfaces and Interfaces* **5**, 15–18 (2016).

19. Hwan Hwang, Y. *et al.* An 'aqueous route' for the fabrication of low-temperature-processable oxide flexible transparent thin-film transistors on plastic substrates. *NPG Asia Mater* **5**, e45–e45 (2013).

20. Socratous, J. *et al.* Electronic Structure of Low-Temperature Solution-Processed Amorphous Metal Oxide Semiconductors for Thin-Film Transistor Applications. *Adv Funct Mater* **25**, 1873–1885 (2015).

21. Calvert, P. Inkjet printing for materials and devices. *Chemistry of Materials* **13**, 3299–3305 (2001).

22. Udom, I., Ram, M. K., Stefanakos, E. K., Hepp, A. F. & Goswami, D. Y. One dimensional-ZnO nanostructures: Synthesis, properties and environmental applications. *Mater Sci Semicond Process* **16**, 2070–2083 (2013).

23. Belver, C., Bedia, J., Gómez-Avilés, A., Peñas-Garzón, M. & Rodriguez, J. J. Semiconductor Photocatalysis for Water Purification. in *Nanoscale Materials in Water Purification* 581–651 (Elsevier, 2019). doi:10.1016/B978-0-12-813926-4.00028-8.

24. *Fundamentals of Nanoparticles*. (Elsevier, 2018). doi:10.1016/C2016-0-01899-5.

25. Cairns, R. W. & Ott, E. X-Ray Studies of the System Nickel—Oxygen—Water. I. Nickelous Oxide and Hydroxide 1. *J Am Chem Soc* **55**, 527–533 (1933).

26. Swanson, H. & Tatge, E. Standard X-ray Diffraction Powder Patterns. *National bureau of standards US circular 539* Preprint at https://doi.org/https://doi.org/10.6028/nbs.circ.539v1 (1966).

27. Hanawalt, J. D., Rinn, H. W. & Frevel, L. K. Chemical Analysis by X-Ray Diffraction. *Industrial & Engineering Chemistry Analytical Edition* **10**, 457–512 (1938).

28. Soltman, D. & Subramanian, V. Inkjet-Printed Line Morphologies and Temperature Control of the Coffee Ring Effect. *Langmuir* **24**, 2224–2231 (2008).

29. Haynes, W. M. *CRC Handbook of Chemistry and Physics*. (CRC Press, 2011).

30. Mahmoud, S. A., Shereen, A. & Tarawnh, M. A. Structural and Optical Dispersion Characterisation of Sprayed Nickel Oxide Thin Films. *Journal of Modern Physics* **02**, 1178–1186 (2011).

31. Tsai, S. Y., Hon, M. H. & Lu, Y. M. Fabrication of transparent p-NiO/n-ZnO heterojunction devices for ultraviolet photodetectors. *Solid State Electron* **63**, 37–41 (2011).

32. Nama Manjunatha, K. & Paul, S. Investigation of optical properties of nickel oxide thin

films deposited on different substrates. *Appl Surf Sci* **352**, 10–15 (2015).

33.   Xu, W. *et al.* p-Type transparent amorphous oxide thin-film transistors using low-temperature solution-processed nickel oxide. *J Alloys Compd* **806**, 40–51 (2019).

34.   Dasi, G. *et al.* Enhanced UV emission of solution processed highly transparent Alq3/ZnO hybrid thin films. *Thin Solid Films* **710**, 138265 (2020).

35.   Jin-Hong, L., Kyung-Hee, K. & Byung-Ok, P. Electrical and optical properties of ZnO transparent conducting films by the sol–gel method. *J Cryst Growth* **247**, 119–125 (2003).

36.   Bose, S. *et al.* Elaboration of high-transparency ZnO thin films by ultrasonic spray pyrolysis with fast growth rate. *Superlattices Microstruct* **156**, 106945 (2021).

37.   Tsay, C. Y., Fan, K. S., Chen, S. H. & Tsai, C. H. *Preparation and Characterization of ZnO Transparent Semiconductor Thin Films by Sol-Gel Method*. *Journal of Alloys and Compounds* vol. 495 126–130 (Elsevier, 2010).

38.   Alzahrani, A. O. M., Abdel-wahab, M. Sh., Alayash, M. & Aida, M. S. Metals and ITO Contact Nature on ZnO and NiO Thin Films. *Brazilian Journal of Physics* **51**, 1159–1165 (2021).

39.   Young Kim, D., Ryu, J., Manders, J., Lee, J. & So, F. Air-Stable, Solution-Processed Oxide p–n Heterojunction Ultraviolet Photodetector. *ACS Applied Materials & Interfaces* **6**, 1370–1374 (2014).

40.   Park, N., Sun, K., Sun, Z., Jing, Y. & Wang, D. High efficiency NiO/ZnO heterojunction UV photodiodeby sol–gel processing. *J. Mater. Chem. C* 7333–7338 (2013) doi:10.1039/c3tc31444h.

41.   Wang, K., Vygranenko, Y. & Nathan, A. Fabrication and characterization of NiO/ZnO/ITO p–i–n heterostructure. *Thin Solid Films* **516**, 1640–1643 (2008).

42.   Ohta, H. *et al.* Fabrication and photoresponse of a pn-heterojunction diode composed of transparent oxide semiconductors, p-NiO and n-ZnO. *Appl Phys Lett* **83**, 1029–1031 (2003).

43.   Leppaniemi, J., Eiroma, K., Majumdar, H. S. & Alastalo, A. In 2 O 3 Thin-Film Transistors via Inkjet Printing for Depletion-Load nMOS Inverters. *IEEE Electron Device Letters* **37**, 445–448 (2016).

Chapter 6

Fully Inkjet-Printed Green-Emitting PEDOT:PSS/NiO/Colloidal CsPbBr₃/SnO₂ Perovskite Light-Emitting Diode on Rigid and Flexible Substrates

In this chapter, results concerning the inkjet-printed fabrication characterization process of light emitting diodes (LEDs) based on CsPbBr₃ metal halide perovskite are presented. The demonstration of inkjet-printed large area devices starts by proving the processability in ambient atmosphere.

Perovskite LEDs (PeLEDs), first reported in the 90's,[1,2] have shown dramatic progress over the last few years, achieving an outstanding peak efficiency of 28%[3,4] and high luminances up to 470 000 cd/m² [3] in less than a decade, a point which took OLED research more than two decades to reach.[5] Inorganic metal halide perovskites in particular stand as a compelling active functional material choice due to their higher stability compared to their organic counterparts.[6–8]

The impressive progress in PeLED EQE has been enabled by solution processing routes, as vacuum evaporated perovskite LEDs suffer from reduced efficiencies.[9] However, these record-breaking results have been obtained through laboratory-scale solution-based deposition methods such as spin-coating and in the tightly controlled atmosphere of a glovebox In this regard, Table 6.1 shows a list inkjet-printed PeLED structures in the literature, with an extended version shown in Table 6.3 at the end of this chapter. While ideal for research and benchmark purposes, such lab-scale fabrication technologies are not conducive to scalable manufacture.

Most of the work in this thesis was dedicated to the demonstration and validation of an inkjet-printing-based fabrication protocol for PeLEDs, as a proof of concept of their potential scalability of mass fabrication through solution processing. For this reason, the final objective should be to fabricate a structure based on only inkjet-printed layers on a flexible substrate, and ideally substituting organic transport layers for inorganic ones, which are potentially more stable.[10,11] Here, the progress of this thesis in the fabrication of inkjet-printed PeLEDs is showcased by using CsPbBr₃ as a benchmark material due to

the proven higher stability of inorganic perovskites.[12] In addition, this section of the thesis takes special importance as it was part of the H2020 European project Drop-It, a research project aiming for the validation of scalable, ambient atmosphere manufacture of inkjet-printed PeLEDs. As a result of focused work in this project, the results presented in this chapter showcase the second published example of a fully inkjet-printed LED (Table 6.1).[13]

Table 6.1 Summary of similar PeLED structures published in the literature comparing peak emission wavelength, maximum luminance, efficiency, and lifetime. This is a condensed form of table Table 6.3, shown at the end of this chapter.

Year	Inkjet-printed layers	Peak emission (nm)	Max. Luminance (cd/m2)	Max. EQE (%)	Lifetime	Ref.
2020	1	520	1233	2.8	-50% in 7 min	Ref[14]
2020	1	530	4000	N.A.	N.A.	Ref[15]
2021	1	515	10992	3.03	N.A.	Ref[16]
2021	1	530	3640	9	-42% in 10 min	Ref[17]
2021	4 (All)	536	10227	0.8	-10% in 100h	Ref[18]
2022	1	517 688 488	43883	8.54 5.54 0.81	-50% in 64 min -50% in 34 min -50% in 2 min	Ref[19]
2022	1	≈ 520	2465	7.9	-50% in 5s	Ref[20]
2022	1	633	30	1	N.A.	Ref[21]
2022	3	510	5038	8.9	N.A.	Ref[22]
2022	1	512	12882	10.1	-50% in 35 min	Ref[23]
2023	1	530	3598	N.A.	N.A.	Ref[24]

The materials and fabrication processes used are systematically optimized towards a fully inkjet-printed, flexible device. To achieve this, the work progresses from simple devices with few inkjet-printed layers into more challenging structures, by substituting spin-coated and evaporated charge transport layers with inkjet-printed ones. The achieved milestones are divided into three steps listed below and summarized in Fig. 6.1.

- Step 1: Validation of inkjet-printed CsPbBr$_3$ and NiO

- Step 2: Inkjet-printed PEDOT:PSS and flexible substrates

- Step 3: Inkjet-printed SnO$_2$ as top hole blocking layer.
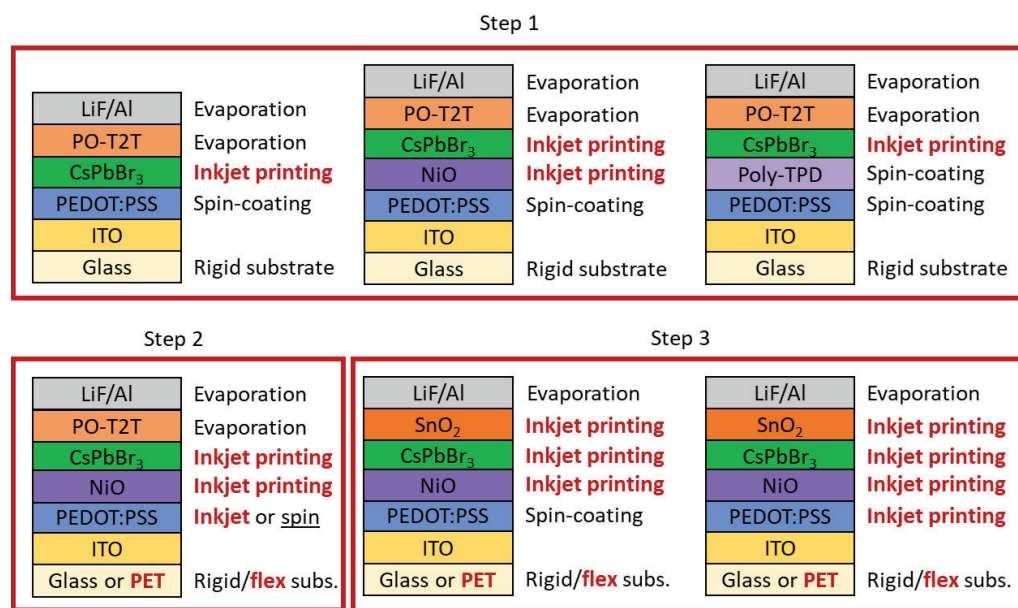
Fig. 6.1 Structures corresponding to each of the steps detailed in this chapter.

Due to the lack of published literature on inkjet-printed PeLEDs with metal oxide transport and blocking layers, this will constitute an exploratory work on the viability of inorganic inkjet-printed flexible PeLEDs.

6.1. Fabrication of inkjet-printed CsPbBr$_3$ LEDs

6.1.1. Characterization of inkjet-printed SnO$_2$

Similar to the formulation of the NiO and ZnO inks presented in **Chapter 5**, a hexanol-based SnO$_2$ nanoparticle inkjet-printable ink was acquired from Avantama AG. The characterization performed in the SnO$_2$ layers is shown in Fig. 6.2, including SEM, optical spectroscopy and XRD. The morphology analysis by SEM (Fig. 6.2a) reveals a granular layer free of pinholes, confirming a morphology similar to that of the NiO and ZnO layers analyzed in **Chapter 5**. Similarly, optical spectroscopy measurements (Fig. 6.2b) highlight the highly transparent nature of the inkjet-printed SnO$_2$ film, with a transparency close or above 90%. Although the successful device architectures presented further along this chapter include SnO$_2$ as the last layer in contact with Al (PIN structure), thus not necessarily benefitting from high transparency since light is outputted through the ITO contacts (Fig. 6.1), the optical characterization of SnO$_2$ suggests good performance in potential future NIP architectures. Finally, XRD analysis (Fig. 6.2c)

133

reveals peaks corresponding to the tetragonal phase of SnO_2, verifying the crystallinity of the NP. Applying the Debye-Scherrer formula to the diffraction pattern, a crystallite size of ≈ 7 nm is estimated.
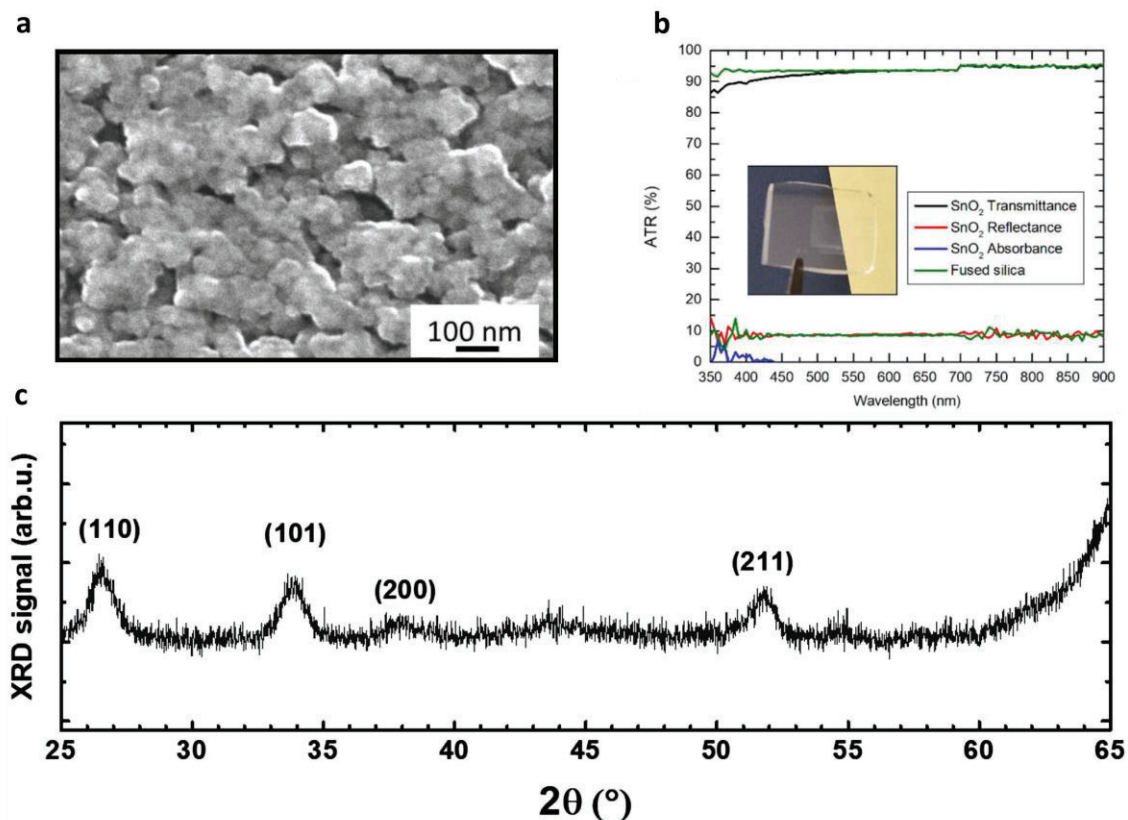
Fig. 6.2 Characterization of inkjet-printed SnO_2 layers by (a) SEM, (b) optical spectroscopy (inset showing an SnO_2 layer printed on fused silica) and (c) XRD.

6.1.2. Validation of transport layers with mixed fabrication processes in a P-N structure

As a preliminary study of the materials and fabrication methods, some of the proposed transport and blocking layers are incorporated into three P-N device structures with no active emissive layer (Fig. 6.3a). These structures replicate some of the layers and fabrication processes that will be employed for PeLEDs: the hole transport layers and electron blocking layers (HTLs and EBLs) are fabricated by spin coating, inkjet printing or a combination thereof, while the hole blocking layer (HBL) PO-T2T was evaporated.

The electrical characterization of these devices should present the expected behavior, i.e. an exponential I-V characteristic and absence of short-circuits, which may indicate imperfect film formation due to undesired pinholes, in order to validate the experimental

methodology prior to the introduction of the perovskite layer. A summary of this electrical characterization is presented in Fig. 6.3b, which shows the average current measured at up to 8 V over 12 identical pixels per tested structure, for a total of 36 pixels. The inset in Fig. 6.3b shows the maximum measured current for all tests, revealing that, none of the 36 devices shows a short-circuit. This observation, in addition to the observed nonlinear behavior, indicating the presence of low leakage currents. The detailed I-V characterization of each pixel is presented in Fig. 6.3c-e, showing relatively tight dispersion of the measured curved. These preliminary results suggest that the layers are of high quality and free of pinholes, and validate the compatibility of the mixed inkjet-printing, spin-coating and evaporation fabrication process.
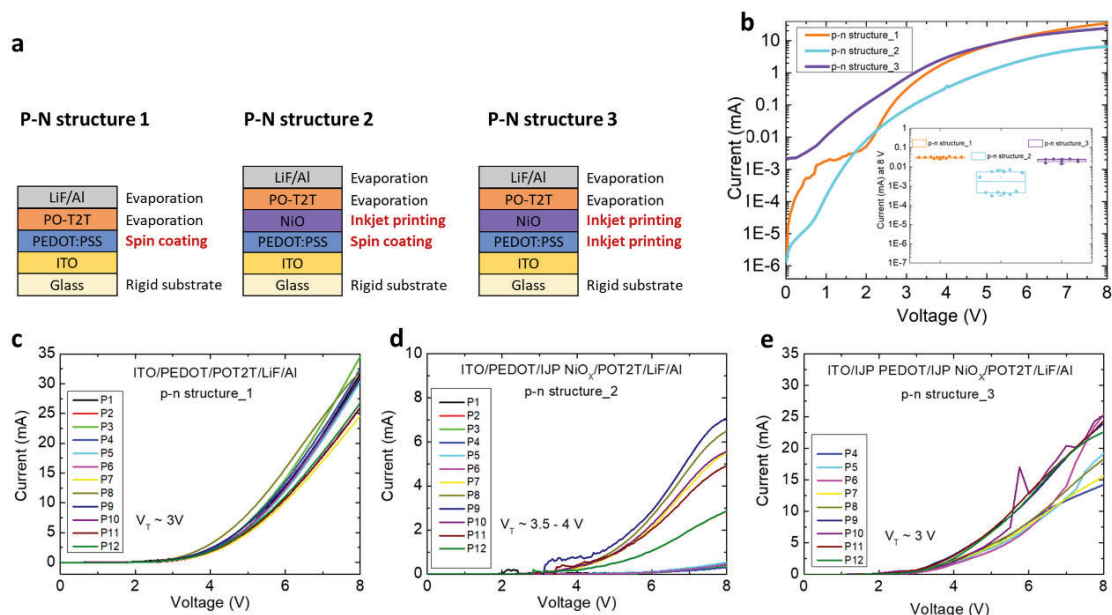
Fig. 6.3 Preliminary characterization of some of the proposed transport and blocking layer materials and fabrication methods, particularly inkjet printing. (a) Sketch of the three structures studied. (b) I-V characteristic, averaged over 12 identical pixels (2 devices x 6 pixels each), of the three structures. (c)-(e) Individual I-V plots of all pixels.

6.1.3. First step: The effect of NiO as electron-blocking layer on luminance

After validation of the inkjet-printed HTLs, inkjet-printed $CsPbBr_3$ was introduced to complete the PeLED structure. The first parameter that will be studied is the effect of NiO on the luminance of the PeLEDs. A standard architecture including the reference materials PEDOT:PSS and PO-T2T will be fabricated with and without an inkjet-printed

NiO interlayer to test its effect on device performance.

6.1.3.1 PEDOT:PSS vs PEDOT:PSS/NiO

The first PeLED structure comparison includes reference transport and blocking layers (p-type PEDOT:PSS, n-type PO-T2T) and contacts (ITO and Al) surrounding the active $CsPbBr_3$ layer, which is inkjet-printed. Besides the inkjet-printed perovskite, all layers are deposited by their respective reference deposition method. The perovskite formulation corresponds to *method 1*, as described in *Chapter 3*.

The inclusion of NiO is anticipated to increase the performance of the device structure, as the deep band of NiO is expected to confine charge carriers within the perovskite layer (Fig. 6.4a), increasing the probability of radiative recombination within it. Furthermore, the valence band maximum of NiO is favorable for the PeLED structure, as it lies at an intermediate level between those of PEDOT:PSS and $CsPbBr_3$.[25] A cross-section FIB image of the fabricated device can be seen at Fig. 6.4b, where flat layers with clearly defined thicknesses can be observed. Furthermore, the integrity of the layers is maintained as no cracks or pinholes are seen, resulting in favorable conditions for device performance.
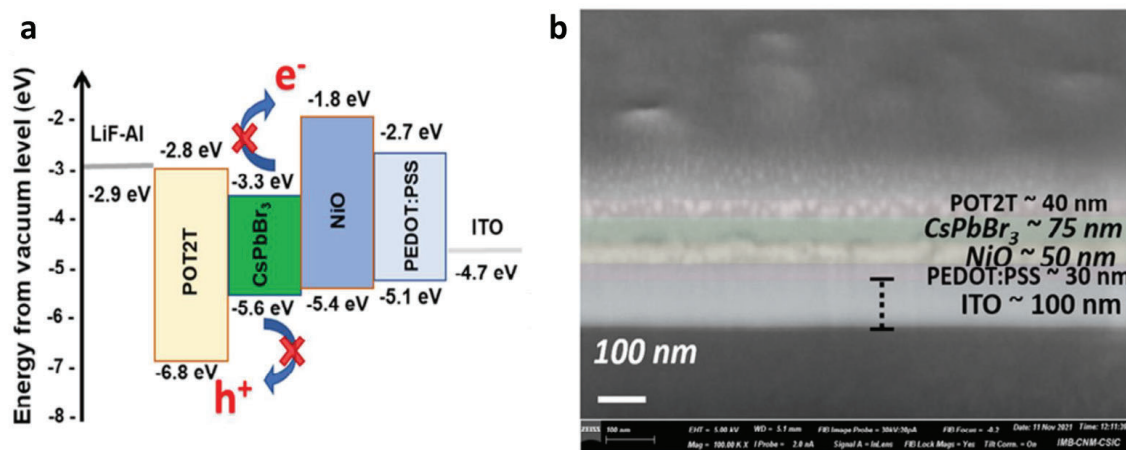
Fig. 6.4 (a) Band diagram of proposed the ITO/PEDOT:PSS/NiO/CsPBBr3/PO-T2T/LiF/Al structure. (b) Cross-section FIB of the fabricated device.

Fig. 6.5a-b shows the I-V behavior of the two devices, with one curve for each of the 6 pixels per device. It can be observed that all pixels show the expected nonlinear behavior with no shunted currents, confirming the high quality of the PeLED structure incorporating inkjet-printed $CsPbBr_3$ as seen previously in the cross-section FIB (Fig.

6.4b). A statistical analysis of the measured currents in both PeLED structures at 8V is shown in Fig. 6.5c, where notably, despite including an extra layer in the device architecture, the structure with NiO appears to show a similar yet slightly higher current distribution. This suggests that indeed, besides the expected reduction in nonradiative losses thanks to the confinement of electrons by the deep valence level of NiO[25] and the reported lower trap density at the NiO/perovskite interface compared to the PEDOT:PSS interface, the intermediate valence level energy of the NiO layer (-5.4 eV) improves the injection of holes between the PEDOT:PSS (-5.1 eV) and CsPbBr$_3$ (-5.6 eV) layers.[26,27]
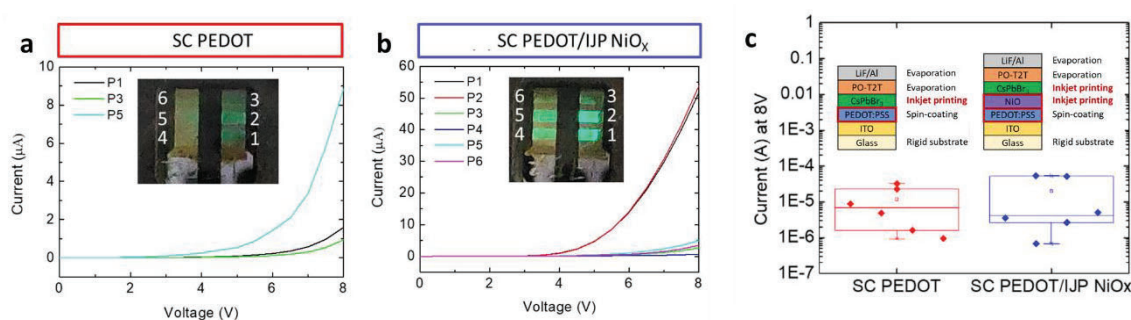
Fig. 6.5 Comparison of I-V characteristic of PeLEDs (a) without inkjet-printed NiO interlayer and (b) with NiO. (c) Analysis of the currents measured at 8 V for the 6 pixels of both devices. The insets show the PeLED pixels in operation.

Following, a comparison of the emission performance of both structures is presented in Fig. 6.6. A clear improvement in luminance can be confirmed in Fig. 6.6c-d after the inclusion of the NiO layer, both in the measured normalized EL intensity, and qualitatively in the inset photographs of the PeLED green emission. These results confirm the expected effect of NiO, and represent the first published validation of an inkjet-printed NiO electron blocking layer within a CsPbBr$_3$ PeLED (check Table 6.1, or its extended version in Table 6.3 at the end of the chapter).
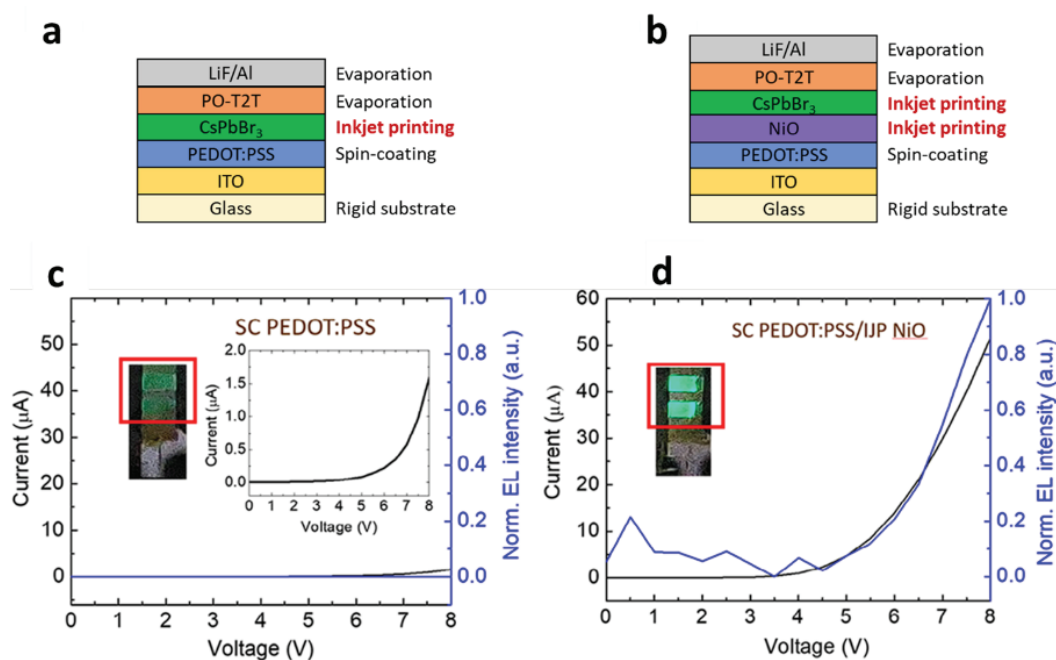
Fig. 6.6 First PeLEDs fabricated comparing the improvement of NiO on device luminance. A sketch of each device architecture is shown on top of the respective characterization. (a) and (c) device with only PEDOT:PSS and (b) and (d) device with PEDOT:PSS/NiO. The insets show the pixels in operation.

6.1.3.2 NiO vs Poly-TPD

After the beneficial effect of the NiO layer was confirmed, attention was directed towards the relatively low emission of the PeLEDs. Suspecting a negative effect from insulating ligands at the $CsPbBr_3$ NC, an improvement in the synthesis of the $CsPbBr_3$ NC colloidal suspension was proposed to reduce the presence of ligands at the NC surface corresponding to *method 2* described in *Chapter 3*.

With this improvement in the quality of $CsPbBr_3$, we challenged our inkjet-printed NiO layer against one of the best-performing reference electron blocking materials in both OLED and PeLED structures, Poly-TPD.[28–30] Having a favorable hole mobility (10^{-6} $cm^2/V \cdot s$),[31] its energy bands are close to those of NiO (-1.8 eV - -5.2 eV for NiO vs -2.4 eV - -5.3 eV for Poly-TPD), thus presenting itself as a fair reference comparison with a high-performance reference material.[32] The comparative performance of devices with inkjet-printed NiO and spin-coated Poly-TPD is shown in Fig. 6.7. A first analysis reveals that both the I-V behavior (Fig. 6.7a) and the emitted wavelength spectrum (Fig. 6.7b) of the NiO and Poly-TPD PeLEDs appear comparable, a preliminary positive indication of the performance of the inkjet-printed NiO.

Indeed, after incorporating the improved perovskite synthesis method, the performance of both devices in terms of luminance is rather high, at values comparable with the published literature (Table 6.3), validating the new perovskite formulation (***method 2***). Comparing the performance of the two structures in detail, the devices with NiO performed remarkably close to those with Poly-TPD, in terms of emission spectra (Fig. 6.7c), turn-on voltage (3V) and maximum luminance (17920 cd/m^2 vs 19230 cd/m^2 for Poly-TPD) (Fig. 6.7d), and EQE (2.6 %) (Fig. 6.7e). This result confirms, on the one hand, the performance of NiO as a material for PeLEDs compared to poly-TPD, and on the other hand, the high layer quality obtained here through inkjet printing compared to that of spin coating. Thus, these findings suggest that inkjet-printed NiO is a strong contender as an EBL alternative to established materials and fabrication processes such as Poly-TPD and spin coating.

Having confirmed the performance of the improved perovskite synthesis method, all devices are fabricated from this point using CsPbBr$_3$ as synthesized by ***method 2***.
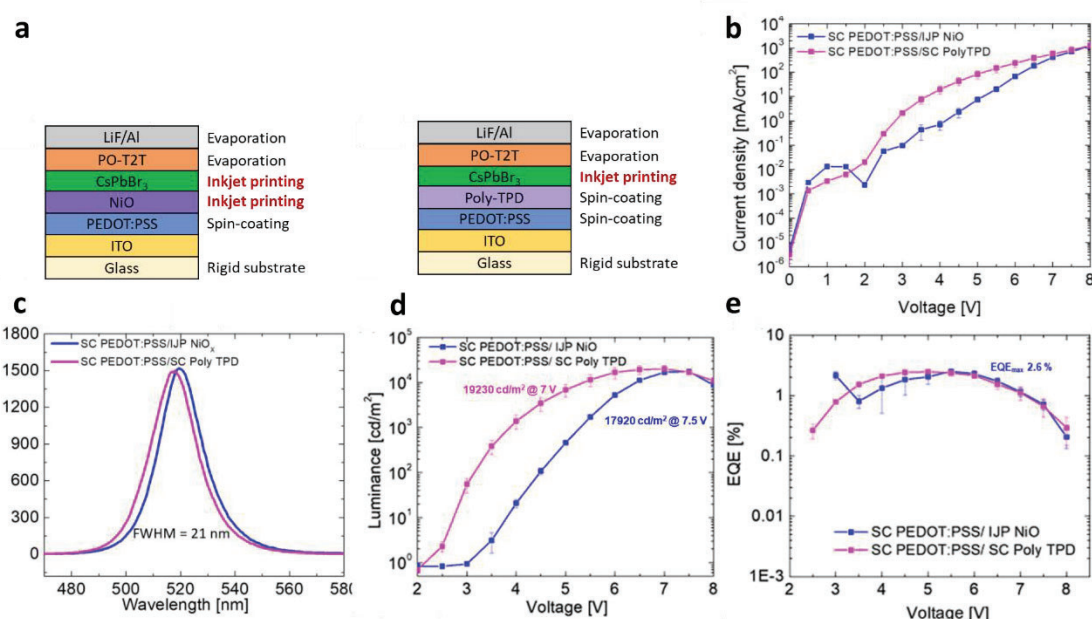

Fig. 6.7 Comparison of performance of PeLEDs fabricated with inkjet-printed NiO interlayer vs reference spin coated poly-TPD, showing their (a) sketches of device structure, (b) semilog J-V characteristic, (c) emission spectra, (d) Luminance vs applied voltage, and (b) EQE vs applied voltage.

6.1.4. Second step: Fabrication with IJP PEDOT:PSS layer on rigid & flexible substrates

Following the success with the inclusion of the NiO inkjet-printed layer, we set on the path to a fully inkjet-printed device on a flexible substrate by continuing to include an increasing number of inkjet-printed layers and experimenting with PET substrates.

In this second step, PeLEDs with an inkjet-printed PEDOT:PSS layer are fabricated. While not changing the material structure of the device, the addition of inkjet-printed layers adds fabrication complexity, as inkjet-printed layers generally have considerably higher roughness compared to their spin-coated counterparts, due to the more local nature of inkjet printing. Similarly, fabrication on flexible substrates is more challenging than on rigid ones, due to the increased surface roughness, and the more challenging handling of substrates during fabrication.

Fig. 6.8a shows the device structures compared in this section. Three structures have been chosen in order to evaluate, first, the effect of incorporating an inkjet-printed PEDOT:PSS layer (comparison I), and second, the effect of using a flexible substrate (comparison II). Despite the challenges added to device fabrication, an initial assessment of the results obtained reveals qualitatively comparable behavior in terms of J-V characteristic with the expected exponential trend (Fig. 6.8b), and turn-on voltage (3-3.5 V), luminance and EQE (Fig. 6.8c).

Analyzing comparison I, the inkjet-printed PEDOT:PSS devices (1639 cd/m^2) show a decrease in performance compared to their spin-coated counterpart (17920 cd/m^2). This is an expected result, as inkjet-printed layers usually require extensive optimization in order to obtain good morphology, compared to spin-coating, which inherently results in smoother film surfaces. The EQE measurements confirm the lower performance of the devices with inkjet-printed PEDOT:PSS, showing a value of 0.38% efficiency, compared to 2.6% for spin-coated PEDOT:PSS. These relatively low efficiencies, compared to the present maximum of 28%,[3,4] are expected for inkjet-printed fabrication. As can be confirmed in Table 6.1 and the extended Table 6.3 at the end of the chapter, PeLEDs with inkjet-printed layers have an EQE < 10% (save for one exception at 10.1%), with the only fully inkjet-printed device showing an efficiency of 0.8%.[18]

Switching to comparison II, however, reveals a surprising result, as the performance of the flexible (1681 cd/m^2) and rigid (1639 cd/m^2) devices is remarkably close. This result suggests that the limiting factor in these device architectures is not the inclusion of a flexible substrate but rather the inkjet-printed PEDOT:PSS layer, which might be further optimized to improve device performance.

Despite the lowered performance of these devices, the obtained luminances are comparable to those of recently published inkjet-printed PeLED literature (Table 6.1, or Table 6.3 for details). These findings reveal that, while further optimization of the inkjet-printed PEDOT:PSS might remain, fabrication of PeLEDs on flexible substrates seems to have a small effect on performance.
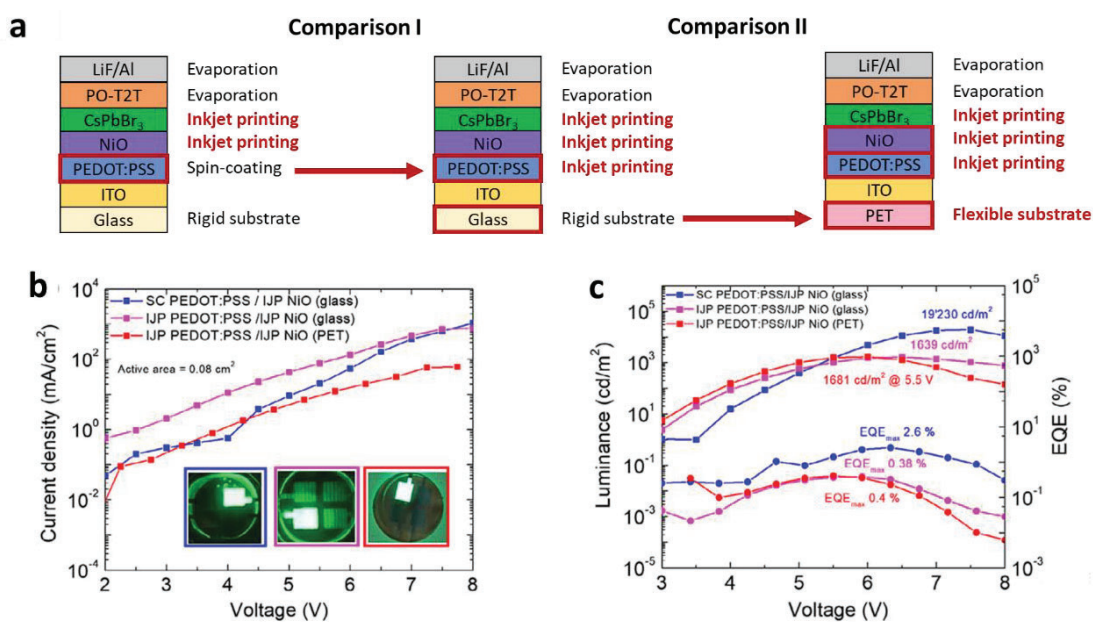
Fig. 6.8 Comparison of three structures (1) PeLEDs fabricated with spin coated PEDOT:PSS on glass substrate (ideal condition) with (2) PeLEDs fabricated with inkjet-printed PEDOT:PSS on glass substrate and (3) PeLEDs fabricated with inkjet-printed PEDOT:PSS on PET flexible substrate. a) J-V characteristic and b) luminance and EQE vs applied voltage. The insets show the PeLED pixels in operation.

In addition, the emission spectra of the devices is not significantly altered after the inclusion of inkjet-printed PEDOT:PSS, maintaining a distribution with a FWHM of 21 nm centered close to 520 nm, confirming the robustness of the inkjet-printed PEDOT:PSS fabrication step.

6.1.5. Third step: Fully inkjet-printed PEDOT:PSS/NiO/CsPbBr$_3$/SnO$_2$ stack on flexible substrate

At this point, the only non-inkjet-printed layer left in the above discussed structures, other than the contacts, was PO-T2T, thus the objective is set on substituting it by an inkjet-printed layer. This last step is perhaps the most critical: solution-processing materials on top of the perovskite layer is known to be challenging compared to vacuum deposition, especially when done in ambient condition and not in a glove-box, because the perovskite is exposed to solvents and to an additional thermal post-treatment step. Among available solution processable inorganic inks, SnO$_2$ is a promising candidate, as its band structure is relatively close to that of PO-T2T (Fig. 6.9a and b), also providing hole-blocking properties. While the lower conduction band of SnO$_2$ would suggest improved injection of electrons into the perovskite layer compared to the PO-T2T structure, thus making SnO$_2$ a better candidate in terms of band matching, the slight mismatch at the contact for the SnO$_2$ structure compared to PO-T2T may yield worse device performance.
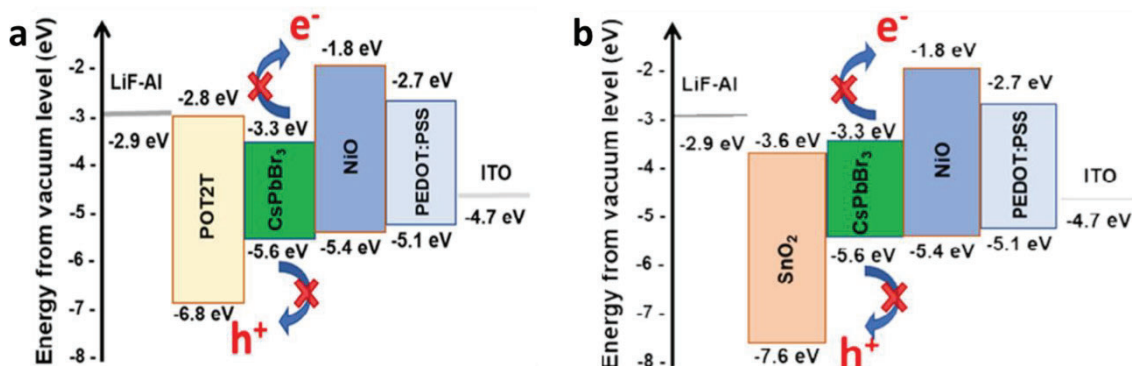
Fig. 6.9 Comparison of band structures of PeLED structures with (a) PO-T2T and (b)SnO2.

The results of this experiment are summarized in Fig. 6.10. A first look at the results obtained confirms that functional fully inkjet-printed PeLED structures have been obtained. First, the devices will be compared according to the fabrication method of PEDOT:PSS (inkjet vs spin coating), keeping the type of substrate constant (rigid vs flexible).

Looking at the **rigid** devices (Fig. 6.10a and c), remarkably similar J-V characteristics and turn-on voltages (3V) are obtained for both inkjet-printed and spin-coated PEDOT:PSS, showcasing the repeatability of the fabrication methodology. In addition, respectable values of luminance are obtained in both cases of 471 cd/m^2 and 324 cd/m^2 for the partially and fully inkjet-printed structures respectively.

Next, the **flexible** devices (Fig. 6.10b and d) will be analyzed. Working PeLEDs have been obtained albeit the highly challenging conditions of fully inkjet-printed fabrication combined with the use of flexible substrates. Despite the modest luminance values of 170 cd/m^2 and 22 cd/m^2 for the partially and fully-inkjet-printed structures respectively (Fig. 6.10), these results are proof of the viability of scalable, fully inkjet-printed manufacture of PeLEDs in ambient conditions. For reference, and notwithstanding the still limited stability and efficiency of the devices, out of all the structures presented only the latter one presents a luminance lower than 100 cd/m^2, the minimum luminance specification for standard definition displays by the European *EBU Tech 3320* specification [33] ($\geq$100 cd/m^2).

Notably, it was observed that the encapsulation process used is not favorable with the inkjet-printed SnO2 devices. While encapsulated devices that had a top PO-T2T layer appeared visually intact after encapsulation, the ones with an SnO2 layer displayed clear wrinkling and in some cases destruction of the device stack.
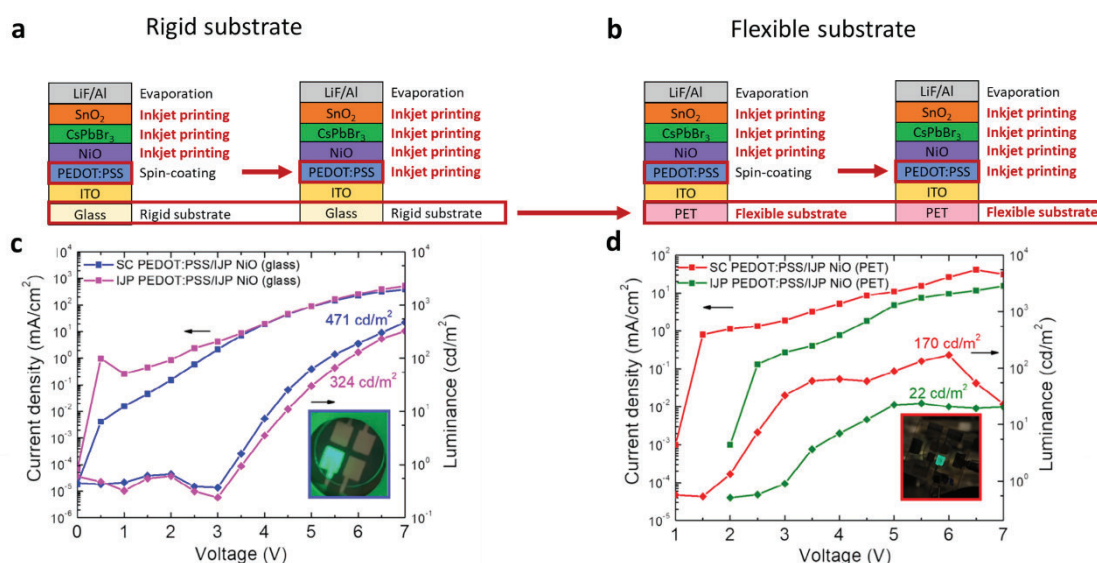
Fig. 6.10 Comparison of fully solution processed PEDOT:PSS/NiO/CsPbBr3/SnO2 PeLEDs on rigid and

flexible substrates. a) schematic structure of devices with spin coated PEDOT:PSS (ideal condition) vs b) devices with inkjet-printed PEDOT:PSS. c) and d) show J-V characteristic and luminance vs applied voltage of devices printed on glass and flexible PET respectively. The insets show the PeLED pixels in operation.

Furthermore, the EL emission spectra of the fully-inkjet-printed devices was measured (Fig. 6.11a), revealing an emission peak centered at 517 nm and a FWHM of 22 nm, consistent with previous measurements of devices finished with a PO-T2T evaporated layer, thus confirming the quality of the $CsPbBr_3/SnO_2$ interface.

The emission stability of the **rigid fully inkjet-printed** devices was studied in ambient atmosphere by measuring their t_{50}, the time after which their original emission (set to 100 cm/m^2 in this case) decays by 50% (Fig. 6.11b). The obtained results of 2-4 min reveal that, while encouraging results of luminance have been obtained, device stability is still one of the major challenges in inkjet PeLED fabrication. This follows the trend observed in the literature, with most published PeLEDs with inkjet-printed layers having a disclosed t_{50} <1h. Beyond inkjet-printed devices, long-term stability is one of the main obstacles in the PeLED research field in general. The major cause of this limited lifetime of PeLEDs is believed to stem from a contribution of Joule effect heating, ion migration and Auger recombination due to unbalanced charge injection.[34,35]
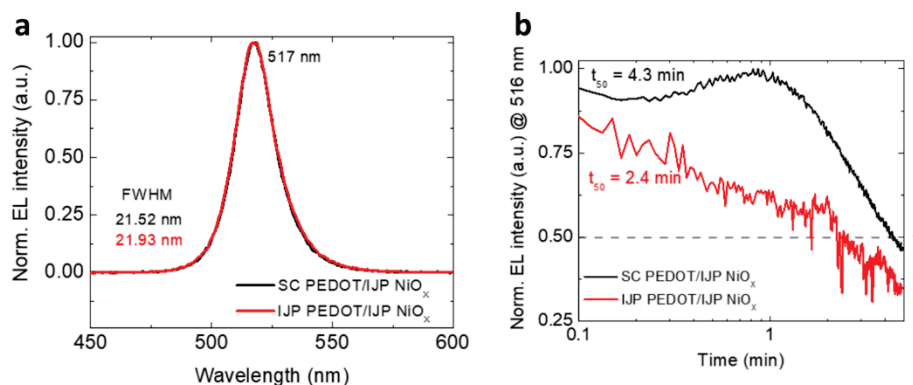
Fig. 6.11 (a) EL spectra of the devices shown in Fig. 6.10a. (b) Measurement of t_{50} for these devices (started luminance at 100 cd/m^2).

A summary comparing the performance of the different proposed devices is presented in Table 6.2, confirming the expected general trend of diminishing performance as more challenging fabrication conditions are introduced. The results of this chapter represent an exploration of the potential for scaling the fabrication of PeLEDs by fully-inkjet-printed deposition on flexible substrates, being the second published fully inkjet-

printed CsPbBr$_3$ PeLED structure, and the first one including the inorganic layers NiO and SnO$_2$, paving the way for future optimization of device structures, ink formulations and fabrication processes.

Table 6.2 Summarized details of the devices fabricated in this chapter. Challenging conditions (inkjet-printed layers and flexible substrates) are highlighted.

Substrate	HTL	Max L (cd/m^2)	Max EQE (%)	ETL
Glass	Spin PEDOT:PSS/**IJP** NiO	17920	2.6	PO-T2T
Glass	**IJP** PEDOT:PSS/**IJP** NiO	1639	0.38	PO-T2T
PET	**IJP** PEDOT:PSS/**IJP** NiO	1681	0.4	PO-T2T
Glass	Spin PEDOT:PSS/**IJP** NiO	471	0.035	**IJP SnO$_2$**
Glass	**IJP** PEDOT:PSS/**IJP** NiO	324	0.017	**IJP SnO$_2$**
PET	Spin PEDOT:PSS/**IJP** NiO	140		**IJP SnO$_2$**
PET	**IJP** PEDOT:PSS/**IJP** NiO	22		**IJP SnO$_2$**

Chapter 6: Fully Inkjet-Printed Green-Emitting PEDOT:PSS/NiO/Colloidal CsPbBr3/SnO2 Perovskite Light-Emitting Diode on Rigid and Flexible Substrates

Table 6.3 Summary of similar PeLED structures published in the literature comparing peak emission wavelength, maximum luminance, efficiency, and lifetime.

Year	Structure (inkjet-printed layers in bold)	Peak emission (nm)	Max. Luminance (cd/m2)	Max Current Efficiency (cd/A)	Max. EQE (%)	Lifetime	Ref.
2020	ITO/PEDOT:PSS/PVK/Poly-TPD/**FA0.3Cs0.7PbBr**/TPBi/LiF/Al	520	1233	10.3	2.8	90 cd/m2 -> 45 cd/m2 (-50% in 7 min)	Ref[14]
2020	ITO/PEDOT:PSS/**MAPbBr3**/BCP/LiF/Al	530	4000	≈ 0.9	N.A.	N.A.	Ref[15]
2021	ITO/PEDOT:PSS/TFB/**CsPbBr3**/TPBi/LiF/Al	515	10992	8.67	3.03	N.A.	Ref[16]
2021	ITO/TFB /PVK/**PEA2Csn-1PbnBr3n+1**/TPBi/LiF/Al	530	3640	31.5	9	120 cd/m2 -> 50 cd/m2 (-42% in 10 min)	Ref[17]
2021	**PEDOT:PSS/MAPbBr3/PEI/AgNWs**	536	10227	2.01	0.8	-10% in 100h	Ref[18]
2022	PEDOT:PSS/PTAA/**Perovskite**/TPBi/ LiF/Al (CsPbBr3, CsPbI3, CsPbBrxCl1−x)	517 / 655 / 488	43883	31.15	8.54 / 5.54 / 0.81	-50% in 64 min / -50% in 34 min / -50% in 2 min	Ref[19]
2022	PEDOT:PSS/MoO3/PVK/**FAPb0.7Sn0.3Br3**/TPBi/ LiF/Al	≈ 520	2465	32	7.9	45 s; 2000 cd/m2 -> 100 cd/m2 (-50% in 5s)	Ref[20]
2022	ITO/PEDOT:PSS/**PEA2SnI4**/PO-T2T/LiF/Al	655	30	0.5	1	N.A.	Ref[21]
2022	ITO/**PEDOT:PSS/MAPbCl3/mCP:Ir(mppy)3**/TPBi/Liq/Al	510	5038	30.8	8.9	N.A.	Ref[22]
2022	ITO/Poly-TPD/PFN-Br/**CsPbBr3+PEAPbBr3**/LiF/TPBi/LiF/Al	512	12882	29.4	10.1	-50% in 35 min	Ref[23]
2023	ITO/PEDOT:PSS/**MAPbBr3+PEG**/BCP or TPBi/LiF/Al	530	3598	2.6	N.A.	N.A.	Ref[24]

6.2. Overview of results regarding inkjet-printed CsPbBr$_3$ PeLEDs

Chapter 6 encompasses a multitude of results accomplished during this thesis, and most of the main objectives set at the start. Following is a summary of the main breakthroughs:

(1) The validation of the inkjet-printing-based fabrication process of CsPbBr$_3$ for PeLEDs.

(2) The functionality of inkjet-printed metal oxide layers in a PeLED, demonstrating homogeneous layers and adequate interfaces in a mixed deposition fabrication process (spin coating, inkjet printing and evaporation).

(3) The achievement of a fully inkjet-printed PeLED active and transport/blocking layer stack. These PeLEDs, while losing efficiency probably due to the added stress on the active layer (as a result of a: the solution processing with an alcohol-based ink on top of the perovskite and b: the thermal stress as a result of the extra thermal treatment for the top metal oxide layer), still display a respectable 324 cd/m^2 for devices fabricated on glass substrates, within the standard specifications for standard definition displays by the *EBU Tech 3320* [33] (≥100 cd/m^2).

(4) The fabrication of these structures on flexible substrates. As mentioned earlier, this is a crucial step for the proof of concept as a process that can be scaled to a commercial manufacturing level.

(5) The validation of a low post-processing temperature of 95 ºC, which places lower stress on all components of the PeLED structure and ensures compatibility with flexible substrates.

REFERENCES

1. Era, M., Morimoto, S., Tsutsui, T. & Saito, S. Organic-inorganic heterostructure electroluminescent device using a layered perovskite semiconductor (C6H5C2H4NH3)2PbI4. *Appl Phys Lett* **65**, 676–678 (1994).

2. Chondroudis, K. & Mitzi, D. B. Electroluminescence from an Organic−Inorganic Perovskite Incorporating a Quaterthiophene Dye within Lead Halide Perovskite Layers. *Chemistry of Materials* **11**, 3028–3030 (1999).

3. Kim, J. S. *et al.* Ultra-bright, efficient and stable perovskite light-emitting diodes. *Nature* **611**, 688–694 (2022).

4. Zhang, L. *et al.* Advances in the Application of Perovskite Materials. *Nanomicro Lett* **15**, 177 (2023).

5. Kar, S., Jamaludin, N. F., Yantara, N., Mhaisalkar, S. G. & Leong, W. L. Recent advancements and perspectives on light management and high performance in perovskite light-emitting diodes. *Nanophotonics* **10**, 2103–2143 (2021).

6. Luo, D. *et al.* Device Engineering for All-Inorganic Perovskite Light-Emitting Diodes. *Nanomaterials* **9**, 1007 (2019).

7. Liang, J. *et al.* Solution synthesis and phase control of inorganic perovskites for high-performance optoelectronic devices. *Nanoscale* **9**, 11841–11845 (2017).

8. Hu, Y. *et al.* Vacuum-evaporated all-inorganic cesium lead bromine perovskites for high-performance light-emitting diodes. *J Mater Chem C Mater* **5**, 8144–8149 (2017).

9. Du, P. *et al.* Efficient and large-area all vacuum-deposited perovskite light-emitting diodes via spatial confinement. *Nat Commun* **12**, 4751 (2021).

10. Kung, P. K. *et al.* A Review of Inorganic Hole Transport Materials for Perovskite Solar Cells. *Adv Mater Interfaces* **5**, 1–35 (2018).

11. Haque, M. A., Sheikh, A. D., Guan, X. & Wu, T. Metal Oxides as Efficient Charge Transporters in Perovskite Solar Cells. *Adv Energy Mater* **7**, 1–23 (2017).

12. Zhang, L. *et al.* Ultra-bright and highly efficient inorganic based perovskite light-emitting diodes. *Nat Commun* **8**, 15640 (2017).

13. Vescio, G. *et al.* Fully Inkjet-Printed Green-Emitting PEDOT:PSS/NiO/Colloidal CsPbBr 3 /SnO 2 Perovskite Light-Emitting Diode on Rigid and Flexible Substrates. *Adv Eng Mater* **25**, (2023).

14. Li, D. *et al.* Inkjet Printing Matrix Perovskite Quantum Dot Light-Emitting Devices. *Adv Mater Technol* **5**, 2000099 (2020).

15. Hermerschmidt, F. *et al.* Finally, inkjet-printed metal halide perovskite LEDs-utilizing seed crystal templating of salty PEDOT:PSS. *Mater Horiz* **7**, 1773–1781 (2020).

16. Zheng, C. *et al.* High-brightness perovskite quantum dot light-emitting devices using inkjet printing. *Org Electron* **93**, 106168 (2021).

17. Li, Y. *et al.* Coffee-Stain-Free Perovskite Film for Efficient Printed Light-Emitting Diode. *Adv Opt Mater* **9**, (2021).

18. Zhao, J. *et al.* High-Speed Fabrication of All-Inkjet-Printed Organometallic Halide Perovskite Light-Emitting Diodes on Elastic Substrates. *Advanced Materials* **33**, (2021).

19. Wei, C. *et al.* A Universal Ternary-Solvent-Ink Strategy toward Efficient Inkjet-Printed Perovskite Quantum Dot Light-Emitting Diodes. *Advanced Materials* **34**, (2022).

20. Ye, T. *et al.* Fabrication of Highly Efficient Perovskite Nanocrystal Light-Emitting Diodes via Inkjet Printing. *Micromachines (Basel)* **13**, 983 (2022).

21. Vescio, G. *et al.* 2D PEA 2 SnI 4 Inkjet-Printed Halide Perovskite LEDs on Rigid and Flexible Substrates. *ACS Energy Lett* **7**, 3653–3655 (2022).

22. Liu, L. *et al.* Inkjet printed organic light-emitting diodes employing organometal-halide perovskite as hole transport layer. *J Phys D Appl Phys* **55**, 105101 (2022).

23. Wang, J., Li, D., Luo, Y., Wang, J. & Peng, J. Inkjet Printing Efficient Defined-Pixel Matrix Perovskite Light-Emitting Diodes with a Polar Polymer Modification Layer. *Adv Mater Technol* **7**, (2022).

24. Schröder, V. R. F. *et al.* Large area inkjet-printed metal halide perovskite LEDs enabled by gas flow assisted drying and crystallization. *Nanoscale* **15**, 5649–5654 (2023).

25. Lee, J. H. *et al.* An Exciplex Forming Host for Highly Efficient Blue Organic Light Emitting Diodes with Low Driving Voltage. *Adv Funct Mater* **25**, 361–366 (2015).

26. Lee, S. Y. *et al.* Investigation of highly luminescent inorganic perovskite nanocrystals synthesized using optimized ultrasonication method. *Ultrason Sonochem* **89**, 106145 (2022).

27. Wang, Z. *et al.* Efficient and Stable Pure Green All-Inorganic Perovskite CsPbBr3 Light-Emitting Diodes with a Solution-Processed NiOx Interlayer. *Journal of Physical Chemistry C* **121**, 28132–28138 (2017).

28. Tremblay, M. H. *et al.* A photo-crosslinkable bis-triarylamine side-chain polymer as a hole-transport material for stable perovskite solar cells. *Sustain Energy Fuels* **4**, 190–198 (2019).

29. Höcker, J. *et al.* Efficient Solution Processed CH 3 NH 3 PbI 3 Perovskite Solar Cells with PolyTPD Hole Transport Layer. *Zeitschrift für Naturforschung A* **74**, 665–672 (2019).

30. Zhang, X. *et al.* Enhancing the Brightness of Cesium Lead Halide Perovskite Nanocrystal Based Green Light-Emitting Devices through the Interface Engineering with Perfluorinated Ionomer. *Nano Lett* **16**, 1415–1420 (2016).

31. Li, J. *et al.* 50-Fold EQE Improvement up to 6.27% of Solution-Processed All-Inorganic Perovskite CsPbBr3 QLEDs via Surface Ligand Density Control. *Advanced Materials* **29**, 1603885 (2017).

32. Chiba, T. *et al.* High-Efficiency Perovskite Quantum-Dot Light-Emitting Devices by Effective Washing Process and Interfacial Energy Level Alignment. *ACS Appl Mater Interfaces* **9**, 18054–18060 (2017).

33. EBU Tech 3320 specification .

34. Cheng, H. *et al.* Understanding and minimizing non-radiative recombination losses in perovskite light-emitting diodes. *J Mater Chem C Mater* **10**, 13590–13610 (2022).

35. Jiang, N. *et al.* Defects in lead halide perovskite light-emitting diodes under electric field: from behavior to passivation strategies. *Nanoscale* **16**, 3838–3880 (2024).

Chapter 7
Summary and conclusions

7.1. General conclusions

The main objective in this doctoral thesis was demonstrating inkjet printing as a tool to fabricate currently emerging devices with next-generation materials, allowing quick prototyping and facile solution processing routes. Unlike other solution processing deposition methods that are commonly used in the literature such as spin coating, which is a repeatable yet non-scalable technique thanks to its simplicity, inkjet printing is a technology that can be scaled to mass production after lab-scale validation of materials and devices. Whereas ink formulations validated in spin coating do not necessarily transfer to scalable printing methods (inkjet printing or otherwise, e.g., gravure), materials and methods validated at the lab scale inkjet printer constitute proof of their applicability to large scale inkjet printing.

In that regard, and with the aim of demonstrating the applicability of the materials and fabrication methods employed in this thesis to high-throughput inkjet-printed manufacture, achieving fully-inkjet-printed device fabrication processes became one of the main objectives of this thesis. In addition, all fabrication processes are performed in ambient conditions (instead of, e.g., inside a glovebox with a protective N_2 atmosphere). While this leads to potentially decreased device performance and stability due to contamination from atmospheric species, this is a crucial condition that further demonstrates the scalability of the materials and fabrication processes described in this thesis.

The objective of demonstrating scalable fabrication conditions has been met throughout this thesis as follows:

7.1.1. h-BN memristors

In the case of h-BN devices, the work demonstrated in this thesis is a continuation of previous work in our research group on h-BN capacitors. ***Chapter 4*** shows Ag/h-BN/Pt and Ag/h-BN/Ag fully inkjet-printed memristors, demonstrating their potential use in

security applications as unclonable physical functions and as true random number generators. These devices have been fabricated in full by inkjet printing, except for the platinum back contact of the Ag/h-BN/Pt structure.

7.1.2. Metal oxide photodetectors and perovskite LEDs

In the case of photodetectors in **Chapter 5** and perovskite LEDs in **Chapter 6**, the top contact was either fabricated from a screen-printed conductive carbon paste (photodetectors) or evaporated aluminum (PeLEDs). Except for the top contacts, fully inkjet-printed and inorganic photodetectors and PeLEDs were demonstrated. The active layers in these devices (metal oxide transport layers: NiO ZnO and SnO_2, perovskite: $CsPbBr_3$, organic buffer layers: PEDOT:PSS) were validated through inkjet printing, achieving functional fully printed stacks of NiO/ZnO for photodetectors and PEDOT:PSS/NiO/$CsPbBr_3$/SnO_2 for PeLEDs.

Another remarkable achievement is the demonstration of inkjet-printed transport layers processed on top of the perovskite layers in PeLEDs. Solution processing on top of perovskite layers is particularly challenging, as perovskites are sensitive to oxygen, moisture, and polar solvents, among others. Academic studies on perovskite LEDs, even those that remark about inkjet-printed devices, generally deposit the last transport layers through vacuum deposition processes, which guarantee better interfaces.

Fully inkjet-printed photodetectors and PeLEDs were attempted through the inkjet deposition of Ag NP inks, in a similar fashion to the h-BN memristors of **Chapter 4**, however working devices were not achieved. These Ag top contact photodetector and PeLED devices showed ohmic behavior response upon the application of voltage, and no photodetection or light emission was detected. This effect may be due to the infiltration of either Ag^+ ions, a highly mobile species, or remaining solvents across the device layers, disrupting normal device behavior. The difference between h-BN memristors and the rest of devices in this thesis may arise from the highly insulating and chemically nature of 2D h-BN nanoflakes, which allows the use of Ag NP contacts, whereas the nanoparticle thin films of the photodetectors and PeLEDs demonstrated in this thesis may be more prone to percolation.

Appendix

7.2. Specific conclusions

Following are the conclusions derived from the specific studies in this thesis.

7.2.1. Inkjet-printed h-BN memristors for security applications

- The feasibility of using arrays of fully inkjet-printed Ag/h-BN/Ag memristors as physical unclonable functions, taking advantage of the inherent unpredictability of switching conditions for these devices that arises from stochastic nano/microscopic processes related to the position of 2D h-BN platelets during device manufacturing. These devices show exceptional endurance of 0.6 million cycles in pulsed mode operation.

- The existence of random telegraph noise enhanced by the substitution of the Pt contact by a second Ag one, creating a symmetrical device structure.

7.2.2. Inkjet-printed NiO/ZnO photodetectors

- The successful inkjet printing manufacturing of transparent thin films of p-type ZnO and n-type NiO showcased on rigid and flexible substrates, demonstrating optimal printability on a variety of surfaces. Thorough investigation of these layers through XRD shows their material properties are as expected. After optimization of the post-treatment process through a vacuum oven, SEM imaging proves the thin layer surface is homogeneous and free of imperfections such as wrinkles, cracks, and pinholes, which would limit their applicability to optoelectronic devices.

- The observation of rectification behavior, demonstrating the semiconducting properties of the layers. This is a key point, as these layers are being studied for their future use in PeLED structures. A rectification ratio of 10^2 is observed between -/+ 3 V. The demonstration of photodetecting properties of these layers further points to an appropriate interface between the layers, a crucial aspect towards the manufacturing of PeLEDs.

7.2.3. Inkjet-printed CsPbBr₃ PeLEDs

- Demonstrated high-luminance PeLEDs with high-quality inkjet-printed perovskite layers, in a mixed device architecture with spin-coated hole

PEDOT:PSS injection layer, evaporated hole blocking PO-T2T layer and spin-coated Poly-TPD inkjet-printed peaking at 19230 cd/m^2 for the Poly-TPD structure, comparable with the literature record of a comparable structure fabricated in glovebox with spin-coated and evaporated transport layers, and inkjet-printed perovskite of 43883 cd/m^2 [1]

- Validated the functionality of inkjet-printed inorganic metal oxide layers in a PeLED, demonstrating homogeneous layers and adequate interfaces with organic and perovskite materials.

- Compared the performance of PeLEDs with an inkjet-printed NiO interlayer vs the reference organic material spin-coated Poly-TPD, demonstrating that our inkjet-printed NiO thin films perform equivalently reference spin coated materials. The PeLEDs with NiO electron blocking layers demonstrated a luminance of 17920 cd/m^2.

- The achievement of a fully inkjet-printed PeLED active and transport/blocking layer stack. These LEDs, while losing efficiency due to the added stress on the active layer (as a result of a: the solution processing with an alcohol-based ink on top of the perovskite and b: the thermal stress as a result of the extra thermal post treatment for the top metal oxide layer), still display a respectable 324 cd/m^2 for fully inkjet-printed PeLEDs on Glass (Glass/ITO/PEDOT:PSS/NiO/CsPbBr$_3$/SnO$_2$/LiF/Al), which is above the technical specifications for displays in *EBU Tech 3320* rated for standard definition content ($\geq$100 cd/m^2).

- The fabrication of fully inkjet-printed PeLED structures on flexible substrates. As mentioned earlier, this is a crucial step for the proof of concept as a process that can be scaled to a commercial manufacturing level.

7.3. Future prospects

Regarding inkjet-printed h-BN memristors for security applications, the results presented in ***Chapter 4*** are an exciting perspective of the possibility to exploit the inherent

---

[1] Wei, C. *et al.* A Universal Ternary-Solvent-Ink Strategy toward Efficient Inkjet-Printed Perovskite Quantum Dot Light-Emitting Diodes. *Advanced Materials* **34**, (2022).

stochasticity of inkjet-printed h-BN memristors for secure identification and random number generation. After the proposed proofs of concept presented here, a focused study on the true random nature of these devices is the logical next step, in order to ensure true random number generation valid for security applications. The results of such validation should inform adjustments in material, device architecture, or otherwise.

Future work on the inkjet-printed metal oxide photodetectors should attempt to discern the conduction mechanism, which may imply a study of I-V behavior at different temperatures. In addition, spectral response measurements should be performed. This additional characterization, plus a study on layer thickness effect on device behavior, should guide optimization of fabrication parameters for future devices.

Finally, concerning inkjet-printed perovskite LEDs, the results presented in this thesis reflect some of the first efforts in the perovskite LED literature towards validating a set of materials, ink formulations and processes for scalable manufacturing of fully inorganic, fully inkjet-printed perovskite LEDs on flexible substrates. After the initial task of demonstrating the feasibility of this device structure, the next logical step involves the optimization of the device structure in order to increase device lifetime, stability, and performance.

While devices with vacuum evaporated top transport layers show competitive luminances up to 19230 cd/m^2, their lifetime and stability is still limited, as shown by the lifetime measurements of t$_{50}$ (the time until a device drops to 50% of its original luminance) of 2.4-4.3 min at an initial luminance working point of 100 cd/m^2. This is a common concern in PeLED literature, as perovskites are known to suffer degradation in an LED structure due to ion migration and exposure to current, which at the present constitutes the biggest challenge towards commercialization of perovskite devices. While this is an intrinsic limitation of perovskite materials which must be addressed otherwise, endurance may also be stunted due to unbalanced injection of holes and electrons, which may place undue stress on the device. Exciting research directions in this regard involve studying the effect of layer thicknesses and material choice of transport layers on device lifetime, luminance and EQE.

An additional next step involves the validation of a structure that allows to deposit

top contacts through inkjet. This may involve printing a buffer layer to insulate the device structure from the top contact.

Appendix A
Scientific and academic contributions during this thesis
A.1. Published articles:

2023

- **Inkjet-Printed p-NiO/n-ZnO Heterojunction Diodes for Photodetection Applications**. González, S., Vescio, G., Frieiro, J. L., Hauser, A., Linardi, F., López-Vidrier, J., Oszajca, M., Hernández, S., Cirera, A., & Garrido, B. (2023). *Advanced Materials Interfaces*, *10*(15). https://doi.org/10.1002/admi.202300035

- **Fully Inkjet-Printed Green-Emitting PEDOT:PSS/NiO/Colloidal CsPbBr₃/SnO₂ Perovskite Light-Emitting Diode on Rigid and Flexible Substrates.** Vescio, G.,* Mathiazhagan, G., González-Torres, S., Sanchez-Diaz, J., Villaueva-Antolí, A., Sánchez, R. S., Gualdrón–Reyes, A. F., Oszajca, M., Linardi, F., Hauser, A., Vinocour-Pacheco, F. A., Żuraw, W., Öz, S., Hernández, S., Mora-Seró, I., Cirera, A., & Garrido, B. (2023) Advanced Engineering Materials, 25(21). https://doi.org/10.1002/adem.202300927

- **Inkjet-printed h-BN memristors for hardware security Nanoscale**, Kaichen Zhu, Giovanni Vescio, Sergio González-Torres, Julià López-Vidrier, Juan Luis Frieiro, Sebastian Pazos, Xu Jing, Xu Gao, Sui-Dong Wang, Joaquín Ascorbe-Muruzábal, Juan A. Ruiz-Fuentes, Albert Cirera, Blas Garrido, and Mario Lanza *Nanoscale*, 2023,**15**, 9985-9992 DOI: https://doi.org/10.1039/D3NR00030C

- **Digital and Analog Resistive Switching Behavior in Si-NCs Embedded in a Si/SiO₂ Multilayer Structure for Neuromorphic Systems.** Morales-Sánchez, A.; González-Flores, K.E.; Pérez-García, S.A.; González-Torres, S.; Garrido-Fernández, B.; Hernández-Martínez, L.; Moreno-Moreno, M. *Nanomaterials* **2023**, *13*, 986. https://doi.org/10.3390/nano13060986

2020

- **Toward RGB LEDs based on rare earth-doped ZnO.** J L Frieiro, C Guillaume, J López-Vidrier, O Blázquez, S González-Torres, C Labbé, S Hernández, X Portier and B Garrido. *Nanomaterials* **2023**, *13*, 986. https://doi.org/10.3390/nano13060986

Articles sent to journal (under review):

2023

- **Inkjet-printed red-emitting flexible LEDs based on sustainable inks of layered tin iodide perovskite.** Giovanni Vescio,* Dmitry N. Dirin, Sergio González-Torres, Jesús Sanchez-Diaz, Rosario Vidal, Iván P. Franco,, Samrat Das Adhikari, Vladimir S. Chirvony, Juan P. Martínez-Pastor, Felipe A. Vinocour Pacheco, Lukasz. Przypis, Senol Öz,, Albert Cirera, Iván Mora-Seró, Maksym V. Kovalenko, Blas Garrido. Sent to EcoMat.

A.2. Contributions to conferences:

2023

- **Demonstrating multiple Metal Oxide charge transport layers in fully Inkjet-Printed Halide Perovskite LEDs on Flexible Substrates** Sergio Gonzalez-Torres, Giovanni Vescio, Gayathri Mathiazhagan, Alina Hauser, Linardi Flavio, Oszajca Marek, Hernández Sergi, Cirera Albert, Garrido Blas. EMRS Spring 2023 Strasbourg, France (Oral)

- **Inkjet-Printed Halide Perovskite LEDs with metal oxide transport layers** S. Gonzalez-Torres, G. Vescio, G. Mathiazhagan, J.D. Forero, A. Hauser, F. Linardi, M. Oszajca, S. Hernández, A. Cirera, B. Garrido. 14th Spanish Conference on Electron Devices (CDE 2023) Barcelona, Spain (Poster)

- **Inkjet-printed lead-free red emitting LEDs based on 2D-perovskite TEA2SnI4** G. Vescio, S. González-Torres, D.Dirin, S. Hernández, A. Cirera, M. Kovalenko, B. Garrido CDE 2023 Spain

- **Hierarchical Approach to the Electrical and Optical Properties of Fully Inorganic Inkjet-Printed Nanocrystalline Perovskite CsPbBr$_3$ Green Emitting LED;** G. Vescio, G. Mathiazhagan, S. González-Torres, J. Sanchez-Diaz, A.Villanueva-Antoli, Rafael S. Sánchez, A. Gualdrón-Reyes, M. Oszajca, A. Hauser, S. Hernández, I. Mora-Seró, A. Cirera, B. Garrido*, ,* 2023, (*Oral*) MATSUS23 & Sustainable Technology Forum València (STECH23)

2022

- **Comparison of performance of inkjet-printed and spin-coated SnO2/NiO**: S. González-Torres, G. Mathiazhagan, J. L. Frieiro, G. Vescio, S. Giménez, J.D. Forero, M. Oszajca, N. Lüchinger, M. Rossier, A. Hauser, F. Linardi, S. Hernández, A. Cirera, B. Garrido E-MRS 2022 Spring Meet France (Poster)

Appendix

- **Study of Small molecule charge transport layers in solution-based ambient air processed perovskite light emitting diodes**: G. Mathiazhagan, S. González-Torres, S. Gimenez, J.D. Forero, G. Vescio, A. Cirera, B. Garrido. s: EMRS Spring Meeting 2022 France (Poster)

- **Investigating Ambient Air Processed Inkjet-Printed Electron Blocking Layer (EBL) and Nanocrystalline CsPbBr3 Emission Layer for Perovskite Based LEDs** G. Mathiazhagan, S. González-Torres, J. Sanchez-Diaz, G. Vescio, J. Cano, A. Gualdrón-Reyes, M. Oszjca, A. Hauser, S. Hernández, I. Mora-Seró, A. Cirera, B. Garrido s: Sustainable Metal-Halide Perovskites for Photovoltaics, Optoelectronics and Photonics (Sus-MHP) Spain (Oral)

- **Stoichiometry tunability of Cesium-Copper-Iodide synthesized by controlling the precursors concentration using a simple one-pot** J. D. Forero,* S. Hernández, J. L. Friero, S. González-Torres, G. Mathiazhagan, G. Vescio, B. Garrido, A. Cirera (Poster)

- **Progress in Inkjet Printing of Lead-Free Perovskites for Optoelectronics**; B. Garrido, **G. Vescio**, G. Mathiazhagan, S. Hernández, S. González, J. Diago, A. Cirera; s, Sustainable Metal-halide perovskites for photovoltaics, optoelectronics and photonics (Sus-MHP), València, Spain, **2022** December, (*Invited Speaker*)

2021

- **Optimization and performance of all inkjet-printed metal oxide heterojunctions for optoelectronic applications** S. González-Torres, J.L. Frieiro, G. Vescio, A. Fernández, M. Oszajca, N. Lüchinger, M. Rossier, A. Hauser, F. Linardi, S. Hernández, A. Cirera, B. Garrido CDE 2021 Spain (Poster)

- **Inkjet-printed ZnO and NiOx: layer and device characterization for optoelectronics** S. Gonzalez-Torres, G. Vescio, G. Mathiazhagan, J.D. Forero, A. Hauser, F. Linardi, M. Oszajca, S. Hernández, A. Cirera, B. Garrido. 14th Spanish Conference on Electron Devices (CDE 2023) Barcelona, Spain (Poster)

- **Full Characterization of Inkjet-printed CsPbBr3 Perovskite Quantum Dot Thin Films for LEDs application** G. Vescio, J.L. Frieiro, A.

F. Gualdrón-Reyes, I. Mora-Seró, S. González-Torres, A. Fernández-Guerra, J. López-Vidrier, S. Hernández, B. Garrido , A. Cirera . CDE 2021 Spain

- **Inkjet-printed Ag$_2$BiI$_5$ and Ag$_3$BiI$_6$ for eco-friendly flexible solar cells** G. Vescio, J.L. Frieiro, M. Oszajca, N. Lüchinger, S. González-Torres, A. Fernández-Guerra, J. López-Vidrier, S. Hernández, A. Cirera, B. Garrido.. EMRS Spring 2021 France (Poster)

- **Inkjet-printed metal halide perovskite devices** S. González-Torres,1 A. Fernández-Guerra, A. F. Gualdrón-Reyes, I. Mora-Seró, M. Oszajca, N. Lüchinger, M. Rossier, A. Hauser, F. Linardi, J. L. Frieiro, G. Vescio, A. Cirera, S. Hernández, B. Garrido EMRS Spring 2021 France (Poster)

- **Progress in inkjet-printed lead-free halide perovskites for LEDs** G. Vescio, S. González, G. Mathiazhagan, J. Diago, S. Hernández, A. Cirera. NanoGe 2021 (Oral)

- **Photovoltaic response dependence on the resistive switching state of silicon nanocrystal multilayers**; J. López-Vidrier, J. L. Frieiro, S. González-Torres, J. Bertomeu, S. Hernández, B. Garrido; Poster, 38th European Photovoltaic Solar Energy Conference and Exhibition, Lisbon (Portugal), 2021.

- **Silicon nanocrystal multilayers as active material for electro-optical resistive switching devices**; J. L. Frieiro, J. López-Vidrier, S. González-Torres, O. Blázquez, K. E. González-Flores, D. Yazıcıoğlu, S. Gutsch, M. Zacharias, S. Hernández, B. Garrido; Oral presentation, EMRS Spring Meeting, Strasbourg (France), 2020.

2019

- **Light effect on the resistive switching properties of ZnO based devices**; O. Blázquez, J. L. Frieiro, F. Bonet-Isidro, S. González-Torres, J. LópezVidrier, C. Guillaume, X. Portier, C. Labbé, P. Sanchís, S. Hernández, B. Garrido; Poster, Annual Meeting of the Institute of Nanoscience and Nanotechnology of the UB, Barcelona (Spain), 2019.

- **ITO/ZnO/p-Si resistive switching devices property improvement via Tb-doping**; F. Bonet-Isidro, J. L. Frieiro, O. Blázquez, J. López-Vidrier, S. González-Torres, C. Guillaume, C.; X. Portier, C. Labbé, P. Sanchís, S.

Hernández, B. Garrido; Poster, Annual Meeting of the Institute of Nanoscience and Nanotechnology of the UB, Barcelona (Spain), 2019

- **Effect of Tb-doping on ITO/ZnO/p-Si resistive switching devices**; F. Bonet-Isidro, J. L. Frieiro, O. Blázquez, J. López-Vidrier, S. González-Torres, C. Guillaume, C.; X. Portier, C. Labbé, P. Sanchís, S. Hernández, B. Garrido; Poster, EMRS Spring Meeting, Nice (France), 2019

- **Light effect on the resistive switching properties of ITO/ZnO/p-Si devices**; O. Blázquez, J. L. Frieiro, F. Bonet-Isidro, S. González-Torres, J. LópezVidrier, C. Guillaume, X. Portier, C. Labbé, P. Sanchís, S. Hernández, B. Garrido; Poster, EMRS Spring Meeting, Nice (France), 2019.

A.3. Participation in research projects:

- **Title:** DRop-on demand flexible Optoelectronics & Photovoltaics by means of Lead-Free halide perovskITes (DROP-IT)
  - o **Program**: H2020-EU.1.2.1.
  - o **Grant agreement ID**: 862656
  - o **Funding**: 3,461,345.00 €
  - o **Duration**: 01/11/2019 – 30/04/2023

- **Title:** Optoelectrónica impresa basada en óxidos metálicos y perovskitas (PRITES)
  - o **Call**: PPN2019D
  - o **Official Code**: PID2019-105658RB-I00
  - o **Funding**: 160,000.00 €
  - o **Duration**: 01/06/2020 – 31/05/2023

- **Title:** Computación en Memoria en soporte flexible: una tecnología disruptiva para el empoderamiento ciudadano (FLEXRAM)
  - o **Call**: PPN2021I
  - o **Program**: NTIC
  - o **Official Code**: TED2021-129643B-I00
  - o **Funding**: 248,300.00 €
  - o **Duration**: 01/12/2022 – presently ongoing

- **Title:** Desarrollo de óxidos de metales de transición con tecnología de silicio para conmutadores electrónicos (memristores) y células solares (METALONIC)

  - o **Official Code**: TEC2016-76849-C2-1-R
  - o **Funding**: 115,500 €
  - o **Duration**: 30/12/2016 – 29/12/2019

Appendix

A.4. Teaching

2022-2023
Força Docent gr@d: 90
Docència Assignada gr@d: 90
Aquests crèdits es divideixen en les assignatures de:

- 364289 Disseny digital bàsic, Grau d'enginyeria electrònica: 15
- 360572 Informàtica, Grau de física: 15
- 364290 Introducció als Ordinadors, Grau d'enginyeria electrònica: 30
- 360295 Electrotècnia, Grau d'Enginyeria Química: 30

2021-2022
Força Docent gr@d: 60 hores
Docència Assignada gr@d: 60 hores
Aquests crèdits es divideixen en les següents assignatures:

- 364290 Introducció als ordinadors, Grau d'Enginyeria Electrònica: 30 hores
- 360295 Electrotècnia, Grau d'Enginyeria Química: 30 hores

2020-2021
Força Docent gr@d: 60 hores
Docència Assignada gr@d: 60 hores
Aquests crèdits es divideixen en les assignatures de:

- 364290 Introducció als Ordinadors, Grau d'enginyeria electrònica: 30 hores
- 360295 Electrotècnia, Grau d'Enginyeria Química: 30 hores

2019-2020
Força Docent gr@d: 60
Docència Assignada gr@d: 60
Aquests crèdits es divideixen en les assignatures de:

- 364290 Introducció als Ordinadors, Grau d'enginyeria electrònica: 30
- 360295 Electrotècnia, Grau d'Enginyeria Química: 30

Appendix B
Dimatix DMP 2850 printer

FUJIFILM

Dimatix® Materials Printer
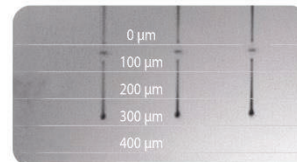## DMP-2850

Dimatix

System Description
- Flat substrate, xyz stage, inkjet deposition system
- Low cost, user-fillable piezo-based inkjet print cartridges
- Built-in drop jetting observation system
- Fiducial camera for substrate alignment and measurement
- Variable jetting resolution and pattern creation PC-controlled with Graphical User Interface (GUI) application software
- Capable of jetting a wide range of fluids
- Heated vacuum platen
- Cartridge cleaning station
- Includes software

Mechanical System
- Printable area
  - Substrate < 0.5 mm thickness: 210 mm x 315 mm (8.27 in x 12.4 in)
  - Substrate 0.5 - 25 mm thickness: 210 mm x 260 mm (8.27 in x 10.2 in)
- Repeatability: ± 25 μm (± 0.001 in)
- Substrate holder
  - Vacuum platen
  - Temperature adjustable; ambient to 60° C (140° F)
- System Footprint: 673 mm x 584 mm x 419 mm (26 in x 23 in x 16 in)
- Weight approximately 50.7 kg (111.8 lbs)
- Power 100-120/200-240 VAC 50/60 Hz 375 W maximum
- Operating range 15-40° C (59-104° F) at 5-80% RH non-condensing
- Altitude up to 2000 m
- Safety and EMC compliance
  - Safety: NRTL Certified to EN 61010-1, UL 61010-1, CSA 22.2 No. 61010-1
  - EMC: EN61326-1 Class A, FCC Part 15 Class A

Fiducial Camera
- Allows substrate alignment using reference marks
- Allows positioning a print origin or reference point to match substrate placement
- Provides measurement of features and locations
- Provides inspection and image capture of printed pattern or drops
- Provides cartridge alignment when using multiple cartridges
- Allows matching drop placement to previously patterned substrate
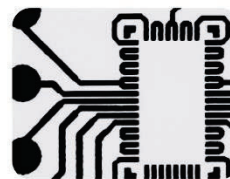
Cartridge
- Type: Piezo-driven jetting device with integrated reservoir and heater
- Usable Ink Capacity: Up to 1.5 ml (user-fillable)
- Materials Compatibility: Many water-based, solvent, acidic or basic fluids
- Samba® Cartridge
  - 12 nozzles, single row, 75 DPI
  - 2.4 pL drop volume, 30 μm dot size (results may vary)

Control PC and Application Software
- Pre-loaded patterned templates
- Pattern preview
- Editors: Pattern, piezo drive waveform, cleaning cycle, substrate setting
- Bitmap (1 bit) files accepted

Replaceable Items
- Print cartridge with one-time user-fillable reservoir
- Cleaning station nozzle blotting pad
- Drop watcher fluid absorbing pad

DMP-2850

| 0 μm |
| 100 μm |
| 200 μm |
| 300 μm |
| 400 μm |

Drop Watcher View

Fiducial Camera View

Dimatix

Cartridge

Dimatix

www.fujifilmdimatix.com

Appendix

FUJIFILM   Dimatix Materials Printer
DMP-2850   **Dimatix**

The Dimatix Materials Printer (DMP) is a benchtop materials deposition system designed for micro-precision jetting a variety of functional fluids onto virtually any surface, including plastic, glass, ceramics, and silicon, as well as flexible substrates from membranes, gels, and thin films to paper products. A complete turnkey system, the DMP facilitates developing and testing manufacturing processes and product prototypes. It also can be used for prototyping of products from flexible circuits, RFID tags and displays to DNA arrays, and wearable electronics. By employing inexpensive exchangeable cartridges that researchers can fill with their own fluid materials, the DMP system minimizes waste of expensive fluid materials, thereby eliminating the cost and complexity associated with traditional product development and prototyping.

The Dimatix Materials Cartridge is a cartridge-based inkjet printhead used with the DMP. Based on FUJIFILM Dimatix's proprietary Silicon MEMS technology, the Dimatix Materials Cartridge is designed for high-resolution, non-contact jetting of functional fluids in a broad range of applications. The cartridge can deposit features to fabricate products such as organic thin-film transistors (TFTs) and printed circuits. In biotechnology, the Dimatix Materials Cartridge allows researchers to closely pack large numbers of elements in DNA arrays, to permit more accurate and efficient analyses.

Appendix C
Resum en idioma oficial

Les noves pressions degudes a les tendències emergents en la fabricació de dispositius estan impulsant els esforços de recerca sobre nous materials i processos de fabricació per a aconseguir noves combinacions de propietats, incloses capacitats com a sensors físics i químics, conductivitat, flexibilitat i transparència. Aquestes aplicacions solen englobar-se al camp de l'Internet of Things (IoT), i es basen en l'ús de dispositius relativament simples i connectats que detecten l'entorn i hi interactuen. Per a abordar aquests reptes, l'electrònica impresa, un camp format per tecnologies d'impressió de gràfics i text adaptades a la fabricació de productes electrònics, és un candidat favorable per satisfer les noves necessitats en la fabricació de dispositius, permetent la deposició de materials de propera generació en forma de tinta, a baix cost i amb potencial per a fabricació escalable.

La impressió per injecció de tinta (inkjet), part del camp de l'electrònica impresa, és una tecnologia de deposició basada en tinta que permet la deposició de multitud de materials funcionals, incloent-hi aïllants, semiconductors i conductors. Gràcies a la seva capacitat de formar patrons digitalment, la geometria de dispositiu es pot definir sense necessitat de màscara ni processos fotolitogràfics. Això no només redueix els costos de fabricació, sinó que també permet la creació ràpida de prototips de dispositius a petita escala, cosa que proporciona una manera d'optimitzar les iteracions de prototipat a un cost inicial reduït, amb adaptabilitat per a una fabricació posterior a gran escala. Gràcies a la seva versatilitat en l'elecció de materials i a la fabricació sense màscares, és possible fabricar estructures completes de dispositius mitjançant impressió inkjet. Tot i això, la impressió inkjet també pot servir com a complement de tecnologies més establertes, com ara els processos complementaris de semiconductors d'òxid metàl·lic (CMOS), on pot complir la funció de tecnologia per al dipòsit de materials innovadors.

Aquesta tesi intenta mostrar la versatilitat de la impressió inkjet com a tecnologia de fabricació de dispositius per a abordar reptes futurs. Després de l'estudi i validació de materials nanoestructurats de diverses famílies impresos per inkjet, es fabriquen i caracteritzen tres tipus diferents de dispositius. Els dispositius demostrats cobreixen

diversos camps d'aplicació, que destaquen l'adaptabilitat de la impressió inkjet: memristors de nanoflakes 2D de h-BN, fotodetectors de nanopartícules d'òxid metàl·lic i díodes emissors de llum (LED) basats en punts quàntics (QD) de perovskita.

Els primers experiments d'aquesta tesi tracten de memristors de nanoflakes h-BN 2D impresos per inkjet per a aplicacions de seguretat de maquinari. Els memristors són una família de dispositius, de vegades coneguts com el quart element de circuit passiu junt amb el resistor, l'inductor i el condensador. La característica principal dels memristors és la possibilitat d'ajustar-ne la resistència elèctrica mitjançant estímuls elèctrics, una propietat que es pot explotar per a guardar informació digital. Tot i que resultats prometedors recents han demostrat el potencial de la integració d'alta densitat per a aplicacions d'emmagatzematge de dades, amb empreses com HP dedicant esforços de recerca en aquest camp, l'aplicabilitat d'aquests dispositius encara està subjecta a la repetibilitat limitada entre dispositius i entre cicles. En aquesta tesi, s'explota l'estocasticitat inherent dels memristors per utilitzar-los com a generadors de nombres aleatoris veritables (TRNG). En particular, es mostra la seva aplicació com a funcions físiques no clonables (PUF), que es poden fer servir com a claus digitals d'identificació úniques.

A continuació, es demostren fotodetectors de nanopartícules d'òxid metàl·lic impresos per inkjet. Els òxids metàl·lics són una família de materials que s'estan estudiant com a materials de bloqueig i transport de càrrega per a cèl·lules solars i LED, i en aquesta tesi es proposen per al seu ús en arquitectures LED com a materials inorgànics processables en solució. A més, com a materials de bandgap ample, els òxids metàl·lics poden complir un paper prometedor en fotodetectors ultraviolats selectius de baix cost, transparents i mecànicament flexibles. En aquest context, es fabriquen i es caracteritzen fotodíodes d'unió p-n de nanopartícules d'òxid metàl·lic p-NiO/n-ZnO impresos per inkjet.

A les seccions finals, s'estudia el camp en ràpid desenvolupament dels LEDs de perovskita (PeLED), centrant-se en la impressió per inkjet de LED de QD de perovskita inorgànics $CsPbBr_3$ per a aplicacions de visualització. En els darrers anys, les perovskites han mostrat avenços impressionants en l'emissió de llum i l'eficiència fotovoltaica i estan posicionades per convertir-se en el material actiu de futurs LED i cèl·lules solars. Les

eficiències més altes als LED de perovskita a la literatura generalment s'aconsegueixen mitjançant nanoestructuració en QD, que poden sintetitzar-se en dispersió col·loïdal mitjançant processos químics fàcils i escalables, com hot injetction, i dipositar-se mitjançant solution processing. Si bé els esforços en la literatura sobre PeLED s'han centrat a obtenir eficiències rècord mitjançant l'ús de tècniques a escala de laboratori, com ara el dipòsit per spin coating, pocs investigadors han demostrat tecnologies de fabricació escalables per a LED de perovskita processades mitjançant solució, com la impressió inkjet. En aquesta tesi, la viabilitat de la impressió per injecció de tinta es valida mostrant PeLEDs completament impresos en substrats flexibles i rígids, aconseguint una emissió verda pura amb un FWHM de fins a 22 nm centrat en 517 nm, que correspon aproximadament a 0.119, 0.790 a coordenades de color x,y de l'espai de color CIE 1931, consistent amb els resultats de la literatura de capes de perovskita obtingudes mitjançant tècniques més establertes, cosa que demostra que les propietats de la perovskita es mantenen mitjançant el procés de deposició per inkjet.

S'han obtingut arquitectures PeLED tant totalment impreses per inkjet com mixtes (amb perovskita impresa per inkjet i capes de transport evaporades/dipositades per spin coating), obtenint luminàncies de fins a 17920 cd/m^2 per a les mixtes, competitives amb les estructures de la literatura obtingudes mitjançant mètodes de deposició més establerts, i fins a 324 cd/m^2 per a aquells impresos totalment mitjançant impressió inkjet, dins de les especificacions de la indústria de les tecnologies de visualització i dins del rang de luminància de moltes pantalles comercials. A més, aquest resultat s'aconsegueix mitjançant el postprocessament a baixa temperatura de capes de transport d'òxids metàl·lics inorgànics, que substitueixen els materials orgànics coneguts per la seva estabilitat limitada a llarg termini. Finalment, es demostren PeLEDs quasi totalment impresos per inkjet en substrats flexibles.

Appendix D
Curriculum Vitae (next page)

Sergio González Torres

Physicist, PhD Candidate

Jan 2024

+34 687 451 679
sergio.gonzh@gmail.com
/in/sergiogtorres/

EXPERIENCE

Sept 2018 – Apr 2024 (Est.) **PhD Candidate**
Universitat de Barcelona, Spain

- Worked in a multidisciplinary international team centered on the optimization of materials and fabrication processes for inkjet-printed perovskite LEDs and solar cells.
- Participated in 4 publicly funded research projects, including a highly competitive European Horizon 2020 FET-OPEN project.
- Taught 200+ undergraduate students in Python, 8085 assembly and electrical technology labs over four years.

Sept 2022 – Sept 2023 **Associate profesor**
Universitat de Barcelona, Spain

Feb 2016 – Jul 2018 **Undergraduate research assistant**
Universitat de Barcelona, Spain

EDUCATION

Sept 2017 – Jul 2018 **Master's degree in Nanoscience and Nanotechnology**
Sept 2013 – Jul 2017 **Degree in Physics**
Universitat de Barcelona, Spain

Sept 2011 – July 2013 **Bsc. Physics (Discontinued)**
University of West Georgia, Carrollton, GA

SKILLS

Deposition technologies • Inkjet printing, spin coating, electron beam evaporation, thermal evaporation, sputtering, lithography, LIFT

Characterization experience (main) • High precision electrical measurements w/ microscopic probe station, confocal & interferometric microscopy, FE SEM (user)

Programing { Data manipulation • Python, Pandas, numpy, scikit-learn, OpenCV

Visualization • Matplotlib, seaborn

LANGUAGES

Fluent English (certified C2 Proficiency), Spanish, Catalan
Working fluency Japanese (certified JLPT N1 ≈ B2+)
Basic German

PUBLICATIONS

orcid.org/0000-0003-0218-3026

8 publications in peer-reviewed academic journals
27 contributions to international scientific conferences

SCHOLARSHIPS

Apr 2019 – Aug 2022 **APIF predoc scholarship**
Feb 2018 – Jul 2018 **Beques Col·laboració IN2UB (2017.17.IN2UB.1)**
Sept 2017 – Jan 2018 **Beca IN2UB Inici Recerca (2017.3.IN2UB.1)**